

I. THE MAGNETIC MOMENT OF THE PROTON IN H₂O
II. INELASTIC COLLISIONS IN EXCITED Na

by

WILLIAM DANIEL PHILLIPS
B.S., Juniata College
(1970)

SUBMITTED IN PARTIAL FULFILLMENT OF THE
REQUIREMENTS FOR THE DEGREE OF
DOCTOR OF PHILOSOPHY

at the

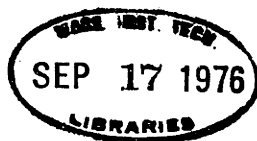
MASSACHUSETTS INSTITUTE OF TECHNOLOGY

1976

Signature of Author: *William D. Phillips*
Department of Physics, August 9, 1976

Certified by: *David M. Kleppner*
Thesis Supervisor

Accepted by: *Dr. Fred Kott*
Chairman, Departmental Committee on Graduate Students



I. THE MAGNETIC MOMENT OF THE PROTON IN H₂O

II. INELASTIC COLLISIONS IN EXCITED Na

by

WILLIAM D. PHILLIPS

Submitted to the Department of Physics on August 9, 1976, in partial fulfillment of the requirements for the degree of Doctor of Philosophy.

ABSTRACT

Part One presents a determination of the magnetic moment of the proton in water in units of the Bohr magneton. By comparing the electron spin flip frequency of atomic hydrogen in a hydrogen maser with the NMR frequency of protons in water we have obtained $g_j(\text{H})/g_p' = 658.216\ 0091(69)$, representing an accuracy of 10 parts per billion (ppb). From this we obtain $\mu_p'/\mu_B = 0.001\ 520\ 992\ 983(17)$ (11 ppb). Our result differs from the previously accepted value by 150 ppb.

Part Two presents measurements of the velocity dependence of the cross section for fine structure transfer collisions. Transfer between the fine structure components of the sodium 3P states induced by collisions with neon and argon has been studied. We find good agreement with theoretical predictions for the Na-Ar collisions and sharp disagreement for Na-Ne.

TABLE OF CONTENTS

	Page
ABSTRACT	2
LIST OF FIGURES AND TABLES	7

PART ONE

Magnetic Moment of the Proton in H₂O

I. INTRODUCTION	12
II. THEORY OF THE EXPERIMENT	17
II.1 Method of Measurement	17
II.2 High Field Hydrogen Maser	18
II.3 NMR Theory	23
II.4 Fourier Transform Analysis	24
III. APPARATUS AND EXPERIMENTAL PROCEDURE	30
III.1 Magnet	30
III.2 Sample Holder	30
III.3 Sample Translator	36
III.4 Microwave Cavity and NMR Coil	39
III.5 Electronics and Data Acquisition	42
III.6 Procedure	47
IV. RESULTS AND ANALYSIS	54
IV.1 Plan	54
IV.2 Analysis of the Electron Signal	55

TABLE OF CONTENTS (continued)

	page
IV.3 Analysis of the Proton Signal	59
IV.4 Corrections	63
IV.5 Final Results	74
V. DISCUSSION	78
V.1 Previous Work	78
V.2 Temperature Effects	79
V.3 Derived Results	80
APPENDIX A Verification of NMR Frequency Determination	83
APPENDIX B Details of Correction Calculations . . .	87
APPENDIX C Computer Programs	91
APPENDIX D Schematic Diagrams	122
REFERENCES	125

PART TWO

Inelastic Collisions in Excited Na

I. INTRODUCTION	128
II. THEORY	137
II.1 Simple Approaches	137
II.2 Molecular Potentials	143
II.3 Semi-classical Theory	145

TABLE OF CONTENTS (continued)

	page
II.4 Quantum Theory	149
II.5 Theory of the Experiment	156
III. APPARATUS AND EXPERIMENTAL PROCEDURES	162
III.1 Vacuum System	162
III.2 Source Flange	164
III.3 Rotating Beam Source	171
III.4 Laser and Input Optics	176
III.5 Fluorescence Collection Optics	185
III.6 Detection Electronics	193
III.7 Procedures - Rotation Mode	195
III.8 Procedures - Laser Velocity Selection Mode	201
IV. RESULTS AND ANALYSIS	205
IV.1 Methods of Analysis	205
IV.2 Na-Ne Collisions	210
IV.3 Na-Ar Collisions	219
IV.4 Na-He Collisions	223
V. DISCUSSION	226
V.1 Relation to Other Work	226
V.2 Comparison of Methods	227
V.3 Suggestions for Future Work	230

TABLE OF CONTENTS (continued)

	page
APPENDIX	233
REFERENCES	235
ACKNOWLEDGEMENTS	237
BIOGRAPHICAL NOTE	239

LIST OF FIGURES AND TABLES

FIGURES, Part One

figure number		page
1	Hydrogen Energy Levels	19
2	Schematic Representation of High Field Maser . .	21
3	Sample Bulb	32
4	Collimator Assembly	34
5	Bulb Assembly	35
6	Sample Translator	37
7	Exploded View of Cavity Assembly	40
8	Coil Coupling Circuit	43
9	Maser Electronics	44
10	NMR Electronics	46
11	Data Digitizer	48
12	Bulb Measurement Set-Up	52
13	Maser Signal	56
14	Transform of Maser Signal	57
15	NMR Signal	60
16	Transform of NMR Signal	61
17	NMR Bulb	66
A1	Centroid Extrapolation	85
D1	Maser Audio Amplifier	122
D2	NMR Audio Amplifier	123
D3	Pulse Buffer and Divider	124

LIST OF FIGURES AND TABLES (continued)

FIGURES, Part Two

figure number		page
1	Velocity Range of Various Methods	134
2	Avoided Crossing	139
3	Landau-Zener Transition Probability	142
4	Na-Ar Potentials	144
5	Coupling Regions	147
6	Na-Ne Cross Section	152
7	Na-Ar Cross Section	153
8	Na-He Partial Cross Sections	154
9	Sodium Level Diagram	158
10	Vacuum System	163
11	Na Source Assembly	165
12	Oven Assembly	166
13	Oven Rotation Mechanism	169
14	Rotating Beam	173
15	Gas Nozzle Assembly	175
16	Dye Laser Internal Optics	177
17	Auxiliary Laser Optics	179
18	Laser Beam Alignment Optics	182
19	Circular Polarizer Alignment	184
20	Collection Optics	186
21	Collection Lens Assembly	187

LIST OF FIGURES AND TABLES (continued)

figure number		page
22	Periscope	189
23	Beamsplitter	190
24	Detection Electronics	194
25	Na Velocity Distribution	208
26	Na-Ne Cross Section, Laser Selected	211
27	Na-Ne Cross Section, High Power	214
28	Na-Ne Cross Section, Rotation Selected	216
29	Na-Ne Cross Sections, Comparison	217
30	Na-Ar Cross Section, Laser Selected	220
31	Na-Ar Cross Section, Rotation Selected	221
32	Na-Ar Cross Section, Parallel Polarizations	222
33	Geometry for Polarization Axis Tests	224
A1	V/F Circuitry	233
A2	Scaler Gate	234

TABLES, Part One

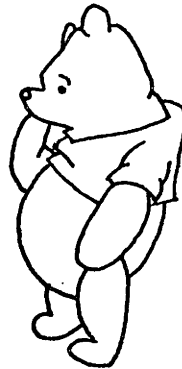
table		page
1	Results of All Runs	64
2	Corrections and Uncertainties in $g_j(H)/g_p'$	67
3	Corrected Values of $g_j(H)/g_p'$	76

On Monday, when the sun is hot
I wonder to myself a lot:
"Now is it true, or is it not,
"That what is which and which is what?"

On Tuesday, when it hails and snows
The feeling on me grows and grows
That hardly anybody knows
If those are these or these are those.

from "Lines Written by a Bear of Very Little Brain"

by A. A. Milne



PART ONE

THE MAGNETIC MOMENT OF
THE PROTON IN H₂O

I. INTRODUCTION

Nuclear magnetic resonance (NMR) is the most precise method for measuring most magnetic fields. The NMR frequency ν' is related to the field by

$$\nu' = \mu'H/h \quad (1)$$

where μ' is the effective nuclear magnetic moment. The effective moment differs from the free moment due to effects of molecular shielding and bulk diamagnetism. In order to determine the field in atomic units, μ' must be related to atomic constants. The most convenient link is through the ratio μ'/μ_B where $\mu_B = e\hbar/2m_e$ is the Bohr magneton. We present here a new determination of μ_p'/μ_B where μ_p' is the effective magnetic moment of the proton in a spherical sample of water. The reason for choosing water as the NMR standard will be discussed in Sec. III.2.

μ_p'/μ_B plays a role in nearly every measurement of a fundamental constant which involves a magnetic field. For example, the proton-electron mass ratio is currently determined by comparing the proton moment in nuclear magnetons with the proton moment in Bohr magnetons:

$$\frac{m_p}{m_e} = \frac{\mu_p'/\mu_N}{\mu_p'/\mu_B} \quad (2)$$

The quantity μ_p'/μ_N is measured by comparing the cyclotron frequency ν_c of a proton (or other ion) to the NMR frequency

of protons. μ_p'/μ_B appears as a natural conversion factor between the NMR frequency and atomic constants.

As another example, the fine structure constant may be obtained from a measurement of γ_p' , the gyromagnetic ratio of the proton in water according to:

$$\alpha^{-1} = \left(\frac{1}{4R_\infty} \frac{c}{\Omega_{lab}/\Omega_{abs}} \frac{\mu_p'}{\mu_B} \frac{1}{\gamma_p'} \frac{2e}{h} \right)^{1/2} \quad (3)$$

where R_∞ is the Rydberg for infinite mass. (The electrical measurements involved in γ_p' and $\frac{2e}{h}$ are in "practical" or "as maintained" units such as NBS amperes and NBS volts; the ratio $\Omega_{lab}/\Omega_{abs}$ connects these to absolute units.) γ_p' is determined by measuring the NMR frequency of protons in water in a magnetic field produced by a current distribution of known strength and geometry; μ_p'/μ_B effectively relates this frequency to atomic constants:

$$\gamma_p' \mu_B / \mu_p' = \frac{e}{2m_e} \quad (4)$$

The gyromagnetic ratio of the free proton, γ_p may be determined from γ_p' by using μ_p'/μ_B in a slightly different context. Since γ_p involves knowing a field in terms of currents and geometry, rather than in atomic units, μ_p'/μ_B is not used as a conversion factor to atomic units, but rather to eliminate effects of molecular and bulk diamagnetism on the protons in water:

$$\gamma_p = \gamma_p' \cdot \frac{\mu_p/\mu_B}{\mu_p'/\mu_B} \quad (5)$$

(It should be noted that in experiments such as this where the magnetic field must be measured in terms of currents and geometry, the achievable precision is generally lower than in experiments where the field can be measured in atomic units by NMR.)

Other quantities whose measurement explicitly uses μ_p'/μ_B include the anomalous electron moment and the magnetic moment of the neutron. Because of the interdependence of the fundamental constants, μ_p'/μ_B has an indirect effect on many other quantities; for further discussion the reader is referred to the most recent adjustments of the fundamental constants (TAY69, COH73).

The ratio μ_p'/μ_B also has important applications in the determination of molecular diamagnetic shielding constants. Although magnetic shielding constants can be measured by NMR with great precision relative to a given standard, their absolute determination requires the measurement of at least one shielding constant absolutely. The absolute, total diamagnetic shielding for protons in a spherical sample of water is

$$\sigma(\text{H}_2\text{O}) = 1 - \frac{\mu_p'}{\mu_p} = 1 - \frac{\mu_p'/\mu_B}{\mu_p/\mu_B} \quad (6)$$

Using $\sigma(\text{H}_2\text{O})$, the shielding of protons in any molecule can be determined by comparing its NMR frequency to that of water. The case of molecular hydrogen is of particular interest; $\sigma(\text{H}_2)$ can be calculated from first principles and provides a

testing ground for the theory of diamagnetic shielding.

The best value of μ_p'/μ_B prior to this work is due to Lambe and Dicke (LAM59) who compared the electron spin flip frequencies in atomic hydrogen with the NMR frequency of a water sample. The electron resonance was observed by microwave absorption in atomic hydrogen buffered by other gases. The quoted uncertainty, 66 ppb (parts per billion), was due to statistics and to unresolved questions about the effect of the buffer gas. As is discussed in Sec. V, there is an additional uncertainty due to the unknown temperature of the sample and other sources of systematic error which were not appreciated at the time of the measurement.

Recent developments have necessitated an improved measurement of μ_p'/μ_B . Measurements of γ_p' by Olsen and Williams at NBS (OLS76) at a level of parts in 10^7 require improved accuracy in μ_p'/μ_B in order to determine α by eq. 3. Measurements of the electron g-factor anomaly (RIC75) and the neutron moment (RAM75) at a level of precision requiring a better μ_p'/μ_B are currently in progress. Recent theoretical calculations of $\sigma(H_2)$ by Reid (REI75) are at a level where a more precise value for μ_p'/μ_B is needed to compare theory and experiment.

We present here the result of a new determination of μ_p'/μ_B based on comparison of the NMR frequency in a water sample and an electron transition frequency in a hydrogen maser. The chief source of statistical error in the Lambe-Dicke experiment was in the determination of the electron

signal line center. The present work provides an improvement in electron linewidth by a factor of 30, and in intrinsic signal to noise by a factor of 10. No buffer gas is used, eliminating a major source of the uncertainty in the previous work. Our final uncertainty, 10 ppb, is due mainly to estimates of uncertainties in systematic errors.

A brief account of our results has been published elsewhere (PHI75). We present here the details of the experiment and data analysis.

II. THEORY OF THE EXPERIMENT

II.1 Method of Measurement

μ_p'/μ_B is determined by measuring $g_j(H)/g_p'$ and using the relation

$$\mu_p'/\mu_B = \frac{g_p'}{g_j(H)} \cdot \frac{g_j(H)}{g_e} \cdot \frac{g_e}{2} \quad (7)$$

$g_j(H)/g_p'$ is measured by alternately observing in the same magnetic field free induction decay signal from protons in water and electrons in atomic hydrogen. The resonance frequencies are determined by fourier analyzing the free decay signals. The proton frequency is proportional to g_p' :

$$\nu_p' = g_p' \mu_B H/h \quad (8)$$

The observed electron frequency must be corrected for the effects of hyperfine coupling and nuclear spin to obtain the field-coupled contribution to the electron frequency, defined as

$$\nu_j \equiv -g_j \mu_B H/h \quad (9)$$

thus,
$$\frac{g_j(H)}{g_p'} = \frac{\nu_j}{\nu_p'} \quad (10)$$

Resonance line Q's for both proton and electron are 10^7 or greater, with signal-to-noise ratios of 30 to 100. Determination of the line centers is therefore not a major problem

in measuring $g_j(H)/g_p'$ to a part in 10^8 . The major theoretical and experimental difficulties arise from the problem of assuring that each sample "sees" the same field. Even after extreme care in design has been taken to accomplish this, there remain corrections whose magnitude must be carefully calculated. These arise in part because the water sample is liquid while the hydrogen is gaseous, which leads to unavoidable differences in the effective shapes of the two samples. There is also a problem arising from the different manner in which each substance samples the field during the measurement.

II.2 High Field Hydrogen Maser

The hydrogen maser used in this experiment is designed to operate in a high magnetic field, though in other respects it is similar to the low field hydrogen maser (KLE62) (RAM65). Fig. 1 shows the energy levels of hydrogen in a magnetic field. In the high field limit m_j and m_I are good quantum numbers. We observe the transition $m_j = 1/2, m_I = -1/2 \rightarrow m_j = -1/2, m_I = -1/2$, corresponding to the electron flipping its spin. The transition frequency ν_{23} is given by the Breit-Rabi formula (RAM56):

$$\nu_{23} = \nu_j - \frac{\nu_0}{2} \left\{ 1 + x \left(1 - \left(1 + \frac{1}{x^2} \right)^{1/2} \right) \right\} \quad (11a)$$

where $\nu_j = -g_j \mu_0 H/h$, (11b)

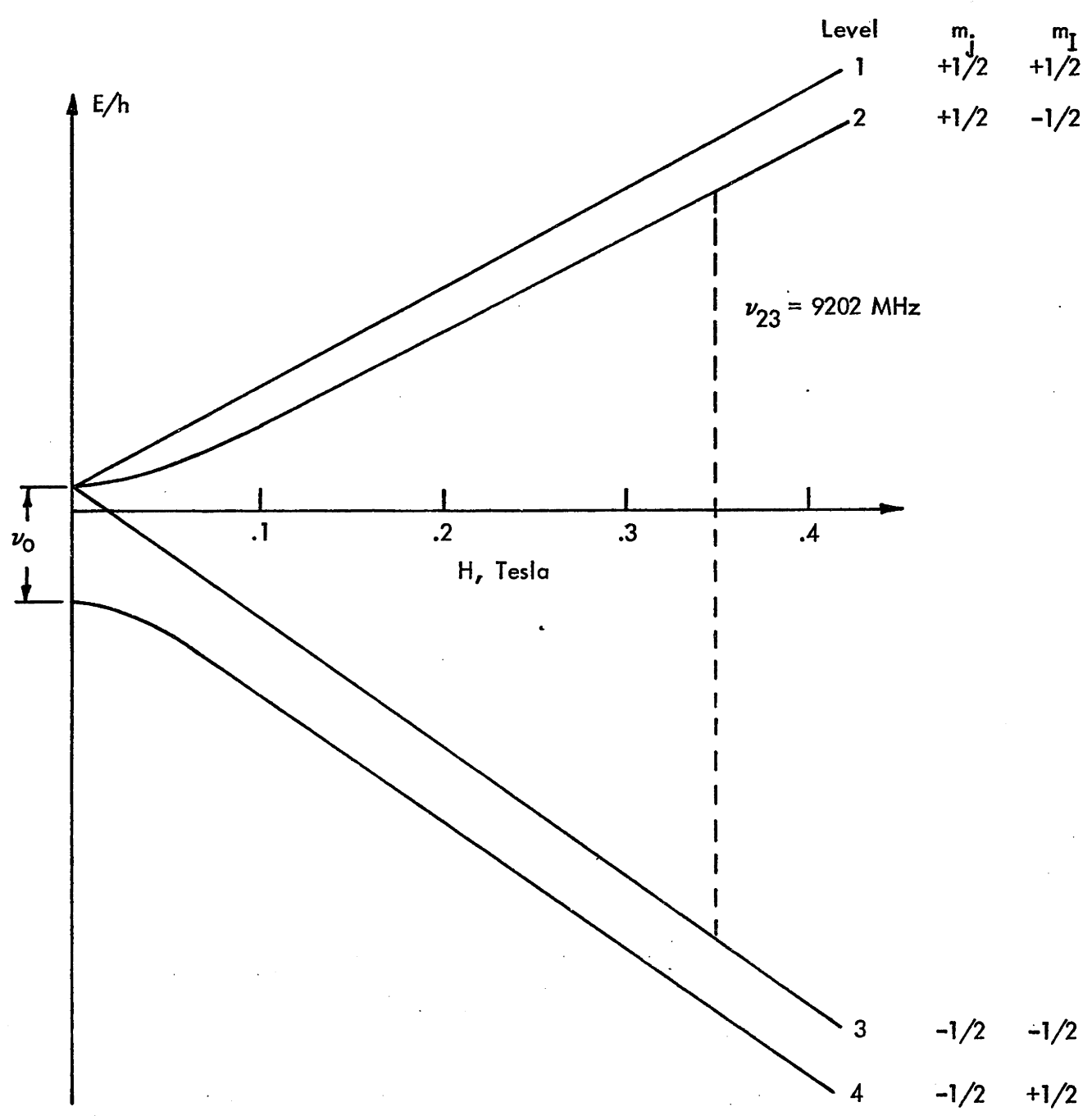


FIG. 1 HYDROGEN ENERGY LEVELS

$$\nu_I = g_I \mu_O H/h \quad , \quad (11c)$$

$$x = \frac{\nu_I + \nu_J}{\nu_O} \quad . \quad (11d)$$

At the field of about .35T used in the experiment $\nu_{23} \approx 9200$ MHz and $x \approx 7$. Once ν_{23} is measured, ν_j may be determined from Eq. 11a using known values of ν_O , the zero field hyperfine splitting, and $\frac{J_P(H)}{g_j(H)}$, the ratio of nuclear and electronic g factors.

Fig. 2 is a schematic diagram of the high field maser. Molecular hydrogen is dissociated in a discharge tube which provides the source for an atomic hydrogen beam. The beam passes through a hexapole state selecting magnet which focuses atoms with electron spin "up" into a spherical storage bulb. A collimator at the entrance of the storage bulb increases the storage time and confines the atoms to the spherical region of the bulb. The bulb is at the center of a microwave cavity tuned to ν_{23} , by means of which oscillatory fields are applied and detected. The cavity is situated between the poles of a magnet in the most homogenous region of the magnetic field.

Because of the state selection, most of the H atoms have their electron spins pointed along the field. This results in a much larger polarization of the sample than is present in thermal equilibrium (as in the Lambe-Dicke experiment) so that a large resonance signal may be obtained with relatively few atoms.

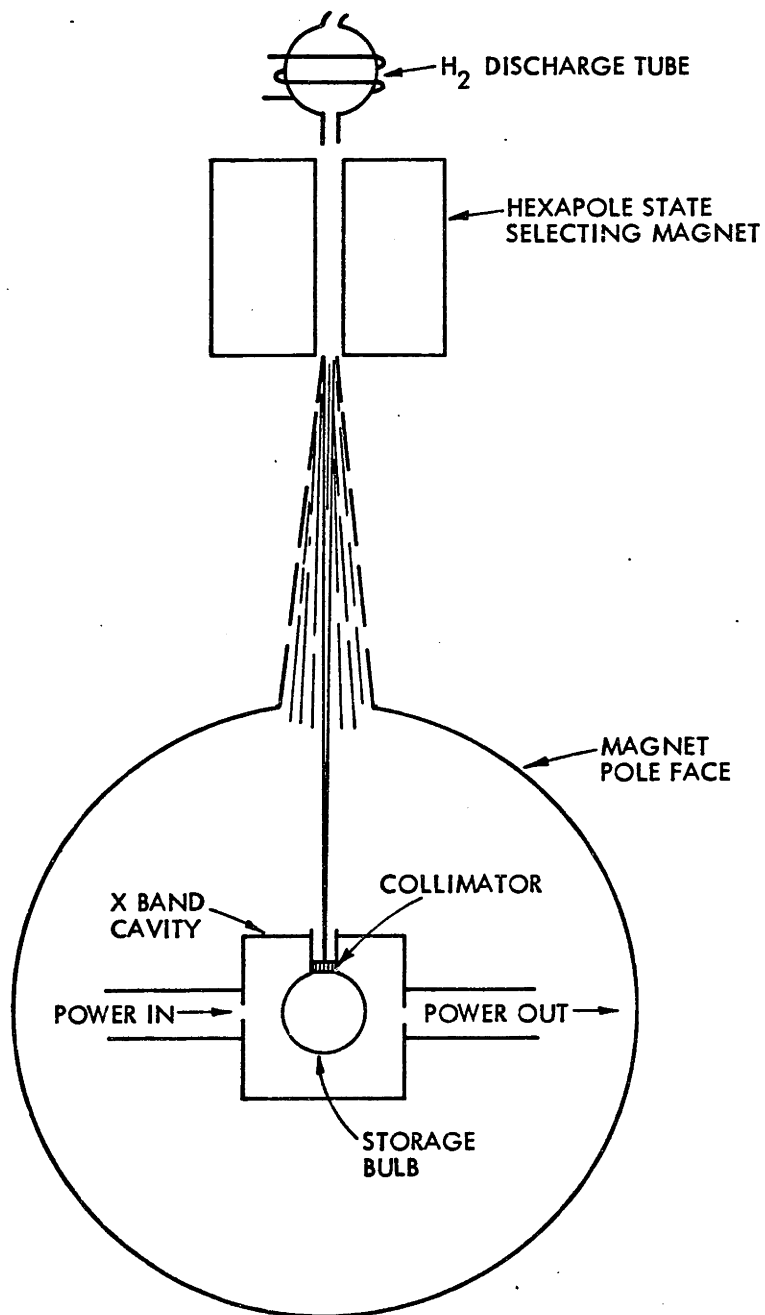


FIG. 2 SCHEMATIC REPRESENTATION OF HIGH FIELD MASER

A $\pi/2$ pulse of microwave radiation near frequency ν_{23} rotates the net moment perpendicular to the static field, whereupon it precesses and radiates at frequency ν_{23} , which is measured.

The relaxation rate of the radiation moment is dominated by three processes. The first is physical escape of atoms from the bulb. The second is relaxation of the radiating moment by collisions with the wall of the storage bulb. Both of these processes are simple rate processes which cause the radiating moment to decay exponentially. Finally, inhomogeneities in the magnetic field cause individual components of the ensemble magnetic moment to precess at different rates, thus relaxing the net moment. If the atoms cross the bulb sufficiently rapidly, motional narrowing occurs and the field inhomogeneities also produce an exponential decay, the rate given by (SLI63):

$$\gamma_{\text{field}} = \langle \Delta\omega^2 \rangle \tau_c \quad (12)$$

where $\langle \Delta\omega^2 \rangle$ is the mean square deviation of the precession frequency over the bulb and τ_c is the mean time for an atom to cross the bulb. Other processes such as spin exchange which also relax the radiating moment are not significant in our case, but would nevertheless lead to exponential decay. The spectral shape of the signal from the maser is therefore known to be lorentzian.

There are a number of well known systematic effects which

can shift the frequency observed with the maser. These include the effects of inhomogeneties, wall collisions, spin exchange collisions and cavity mistuning. These effects have been discussed in detail elsewhere (WAL72a) and in a typical maser experiment (WAL72b) were in the order of parts in 10^{11} . In no case can these errors have an effect as large as 1 ppb for our experiment.

For a more complete discussion of the theory of the high field maser, the reader is referred to earlier work on the subject (WAL72, WIN72, MYI66).

II.3 NMR Theory

The NMR signal is observed using standard techniques of pulsed NMR spectroscopy (ABR61, FAR71). Free induction decay is observed and the signal is fourier analyzed. The usual longitudinal and transverse relaxation processes for liquids operate to relax the free induction signal exponentially. In addition, the macroscopic field inhomogeneties cause relaxation which depends in detail on the nature of the field. This is in sharp contrast to the case of the maser where macroscopic motion of the H atoms results in motional narrowing and exponential decay.

One can regard the NMR signal which results from a sample in an inhomogeneous field as the sum of signals coming from various volume elements of the sample, each decaying exponentially according to the intrinsic relaxation mechanisms but oscillating at the frequency determined by the magnetic field at its location. The spectrum of this signal is a sum of lorentzians at each of the different

frequencies. More precisely, it is the convolution of a lorentzian of width determined by the simple rate processes with the distribution function of NMR frequencies over the sample volume. This is strictly true only if each volume element contributes proportionately to the signal, that is, if the r.f. field in the NMR coil is uniform over the sample. The NMR frequency which we wish to obtain from our measurement is the frequency corresponding to the volume average magnetic field. Under conditions of r.f. field uniformity this is the centroid of the absorptive spectrum. Methods for determining this centroid for an arbitrary line shape are discussed below.

One possible systematic effect in the determination of the NMR frequency is the presence of dissolved impurities in the water, especially paramagnetic impurities. In samples which have been heavily doped with paramagnetic salts to increase the longitudinal relaxation this effect can be very important, but in samples as pure as tap water, the effect is not significant at the 10^{-8} level (WAU74), so we can safely assume this error to be negligible for distilled water.

II.4 Fourier Transform Analysis

The frequency spectra of the maser and NMR free induction decay signals are obtained by fourier analysis. The signals are heterodyned to an audio frequency, the audio signal is

sampled periodically in time and the results are analyzed by taking a discrete fourier transform of the resulting set of points.

If the signal is sampled at rate $1/\tau$, a set of signal points $f(t_j)$ result, where

$$t_j = j\tau \quad , \quad (13)$$

the discrete fourier transform of $f(t_j)$ is

$$g(\omega_k) = \sum_{j=0}^{N-1} f(t_j) e^{-i\omega_k t_j} \quad , \quad (14)$$

While in principal this expression could be evaluated for any value of ω_k , all of the information is contained in a set of N values given by

$$\omega_k = \frac{2\pi}{N\tau} \cdot k \quad , \quad 1 \leq k \leq N \quad . \quad (15)$$

Note that the function $g(\omega_k)$ is periodic in k with period N . In practice the function $g(\omega_k)$ is evaluated by means of a fast fourier transform (FFT) algorithm which simplifies machine processing provided N is chosen to be a power of 2 (CO065, BEL72).

If we assume the signal $f(t)$ to be an exponentially damped oscillation (as is the case with the maser signal):

$$f(t) = \cos(\omega_0 t + \phi) e^{-\gamma t} \quad (16a)$$

we obtain:

$$\begin{aligned} \operatorname{Re} g(\omega_k) = & -\frac{1}{2} \left[(1+\delta) \frac{\gamma \cos \phi - (\omega_0 - \omega_k) \sin \phi}{(\omega_0 - \omega_k)^2 + \gamma^2} \right. \\ & \left. + (1+\delta') \frac{\gamma \cos \phi - (\omega_0 + \omega_k) \sin \phi}{(\omega_0 + \omega_k)^2 + \gamma^2} \right] \\ & + \text{periodic repetitions} \end{aligned} \quad (16b)$$

where δ and δ' , which arise from the finite integration time, do not depend on ω_k for ω_k given by Eq. 15. They are of the order of $e^{-\delta N\tau}$ and are small for sufficiently large N .

The term in Eq. 16b which is centered at $\omega = \omega_0$ is the resonance of interest. The feature at $\omega = -\omega_0$ is an image due to the negative frequency components of the signal. (This arises because the signal is real, oscillating as $\cos \omega_0 t$. If the signal were expressible as $e^{i\omega_0 t}$ the image would disappear.) Eq. 14 reveals that both the signal and the image are repeated with period $2\pi/\tau$. Wings of the image and of the repetition lines can contribute to the signal at $\omega \sim \omega_0$, and cause distortion.

For the maser signal the determination of ω_0 is a straightforward problem of fitting Eq. 16b to the transformed signal. The NMR signal however, does not have a well known functional form since its damping depends on the details of the magnetic field inhomogeneities. The general nature of the

transformed signal, however, is indicated by Eq. 16b. There is an absorption-dispersion feature centered at $\omega_k = \omega_0$ and a similar image feature at $\omega_k = -\omega_0$. The periodic repetitions produce features at $\omega_k = \omega_0 + 2\pi n/\tau$ and $\omega_k = -\omega_0 + 2\pi n/\tau$ where n is any integer. The true NMR frequency is defined as the average NMR frequency over the volume of the sample. If every volume element contributes equally to the signal, that is, if the r.f. field is uniform, this becomes

$$\omega_p' \text{ NMR} = \int g_a(\omega) \omega d\omega \quad (17)$$

where $g_a(\omega)$ is that portion of the transform signal which corresponds to the purely absorptive part of the first term in Eq. 16b. To obtain $g_a(\omega)$ from $g(\omega)$, real and imaginary parts of $g(\omega)$ are combined:

$$\begin{aligned} \cos \phi R_e g(\omega) + \sin \phi I_m g(\omega) = g_a(\omega) + \text{image} \\ + \text{repetitions} \end{aligned} \quad (18)$$

where the image term has in general both absorptive and dispersive components.

The difficulty presented by Eq. 18 is that the wings of the images and repetitions overlap $g_a(\omega)$ in the region where $g_a(\omega)$ is large. Repetitions of $g_a(\omega)$ are not bothersome, since they are absorptive and fall off rapidly. In addition they are symmetrically distributed about $g_a(\omega)$ so

their effects tend to cancel. The image and its repetitions on the other hand generally have dispersive components which fall off slowly and which tend to add rather than cancel.

Two steps may be taken to minimize the effects of the images. First the sampling frequency is chosen so that the images are symmetrically distributed about the signal spectrum, and therefore as far away as possible. Choosing $1/\tau \approx 2\omega_0/\pi$ places the image at $-\omega_0$ and its first repetition at $3\omega_0$, so that both are separated from the signal by $2\omega_0$. Second, the heterodyne beat frequency, ω_0 , is chosen to be as high as possible, thus spreading out the pattern of images. With these precautions the effects of the images can be made negligible.

The problem remains of determining the proper value of ϕ in Eq. 18 since in practice ϕ is not known a priori. The problem is complicated by the fact that the absorptive line shape is in general assymmetric. The most successful method we have found for doing this is an iterative procedure in which ϕ is varied so as to make the wings of $g_a(\omega)$ symmetric about an assumed value of ω_p' ; a new value of ω_p' is computed from $g_a(\omega)$ and this is used as the symmetrization point for a new computation of ϕ . Because even an inhomogeneously broadened line such as our NMR signal is lorentzian in its wings, this method is not sensitive to the details of the line shape. The integration region for the determination of

ω_p' is restricted to a small region symmetric about ω_p' to avoid the effects of images. (The images could be eliminated experimentally by performing the fourier transform on a complex $f_c(t)$ formed from the real signal plus a signal $f_i(t)$ delayed by 90° to provide the imaginary part. The problem here is to insure accurate quadrature of the signals. We have chosen to deal with the problem computationally rather than electronically.)

We have tested the procedures described above for determining the average NMR frequency by performing the analysis on computer generated NMR signals, formed from sums of exponentially decaying signals with various frequencies (WRI74). In cases corresponding to linewidths and asymmetries several times greater than those encountered in practice, errors in determination of the true average frequency or centroid of the NMR line corresponded to a few ppb.

III. APPARATUS AND EXPERIMENTAL PROCEDURE

Because much of the apparatus has been described previously (MYI66, WIN70, WAL72), we focus here only on features which are new or are essential to the experiment.

III.1 Magnet

A permanent magnet, described in connection with earlier experiments with the maser (WIN72, WIN70, MYI66), was used. The field is approximately 0.35 T, the pole diameter is 26.6 cm, the gap is 6.5 cm. A set of 16 electrical shims produces a field homogeneity of 1 part in 10^7 over a 2 cm diameter volume, as determined by the decay rate of the electron signal. Careful thermal isolation and temperature regulation results in a drift rate of typically 2 ppb/min. The short term field jitter is less than 10 ppb.

III.2 Sample Holders

A key problem in an experiment which requires interchanging samples is to insure that both samples "see" the same field. Because the sample holders appreciably alter the field by their intrinsic diamagnetism, meticulous care was needed in their design and construction.

Our approach was to construct sample holders which are as identical as possible, and then to eliminate residual errors by reversing their roles so that each holder was used both for the water and the hydrogen signal.

The sample holders were fabricated from fused quartz. This material was chosen because it can be shaped with high precision, can be coated to inhibit wall relaxation of H atoms and because it has a low loss factor at the 9 GHz electron frequency. (The low loss factor is needed to avoid undue loading of the microwave cavity.)

The sample holders are in the shape of spherical bulb with a cylindrical neck (Fig. 3). They were formed by vacuum shrinking a quartz tube around a graphite form. The forms were machined from high purity graphite in the shape of a bulb, 1.27 cm diameter, with a stem, either 0.254 or 0.457 cm diameter. The form was removed from the bulb by drilling the stem region and burning the remainder in a furnace at about 1200°C, while flowing pure oxygen into the stem. Sphericity of the bulbs was checked with an optical comparator using a method to be described later in this section. The dimension is generally within 25-50 micron of the graphite form, and successful bulbs differ in their largest and smallest diameters by less than 0.2%.

The outsides of the bulbs were lapped spherical with a diameter of 1.429 cm. Four suitable bulbs were produced, two with .457 stems, which we shall designate as Pair A, and two with .254 cm stems, which we shall designate as Pair B. The entire experiment was separately performed with each pair.

The sample bulbs were treated with a coating agent to inhibit relaxation of the atomic hydrogen. Teflon, most commonly used, could not be applied successfully because of slight

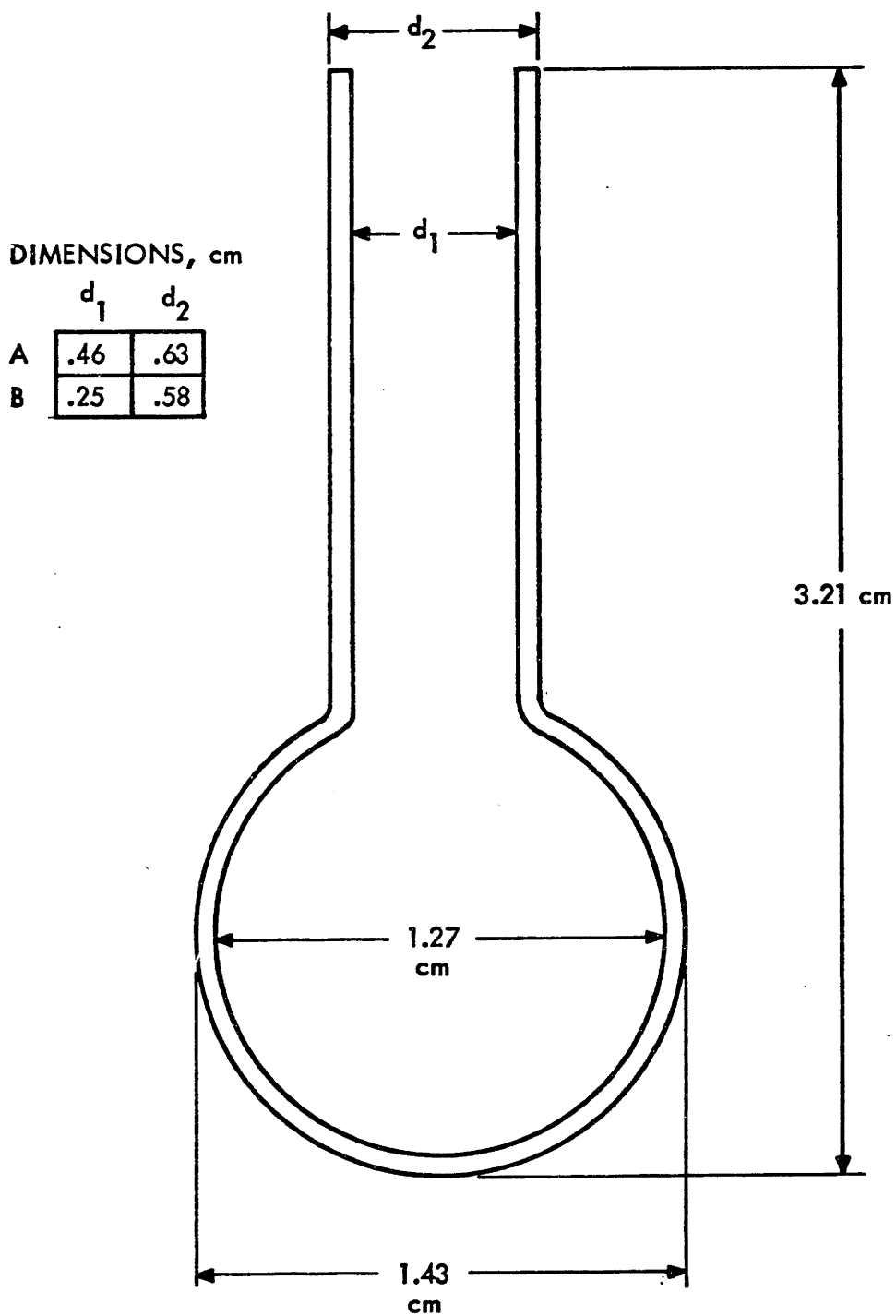


FIG. 3 SAMPLE BULB

surface irregularities. Instead, the surfaces were treated with $(CF_3CH_2CH_2)_2SiCl_2$ (CRA73), a flourinated variant of "Dri-Film", $(CH_3)_2SiCl_2$. The coating procedure, developed by Valberg (VAL69) is as follows: After thoroughly cleaning the bulb with acids and solvents and finally rinsing with water, several drops of the flourinated dri-film are put in the bulb and swirled around. Water is added to complete the reaction, and the bulb is rinsed with water. An acetone rinse is then used to remove oils formed by the reaction.

A collimator, needed to contain the hydrogen, was fabricated from a glass capillary array (Corning 0080) supplied by Galileo Electro-Optics (Sturbridge, Mass.). The capillary diameter is 25μ , the array thickness is .076 cm, and the transmission is 50%. Collimators were used on all sample holders to maintain symmetry. Each collimator was glued with Duco Household cement to the end of a tube which fit into the bulb stem, locating the collimator just above a tangent to the spherical cavity. The tubes were fabricated from quartz for pair A and acrylic plastic for pair B. Boron nitride alignment collars were glued to the tubes with Torr-Seal (Varian Associates). The entire collimator assembly is shown in Fig. 4.

Each pair of bulbs was fixed together into a rigid assembly, Fig. 5. Dummy stems were fixed to the bottom of each bulb with Torr-Seal. The lower stem of the NMR bulb was joined to a push rod by a boron nitride fitting. The joint was made smooth and flush to allow it to pass freely through an o-ring vacuum seal. The push rod is a quartz tube with a Delrin fit-

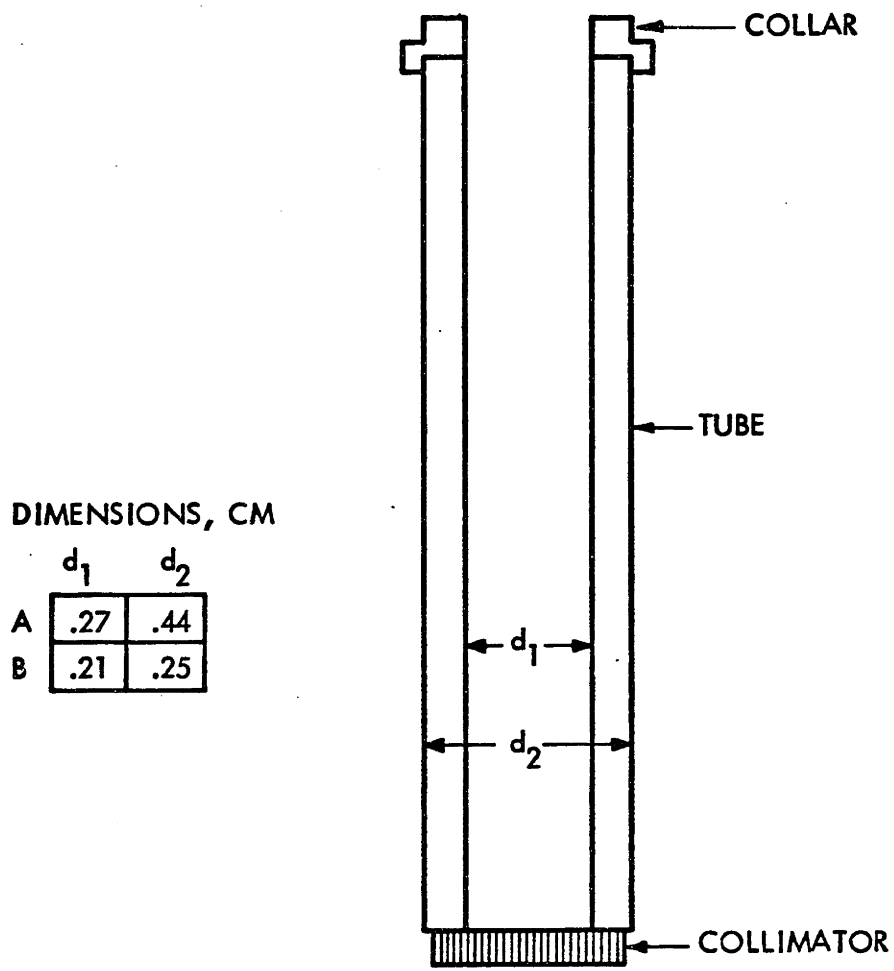


FIG. 4 COLLIMATOR ASSEMBLY

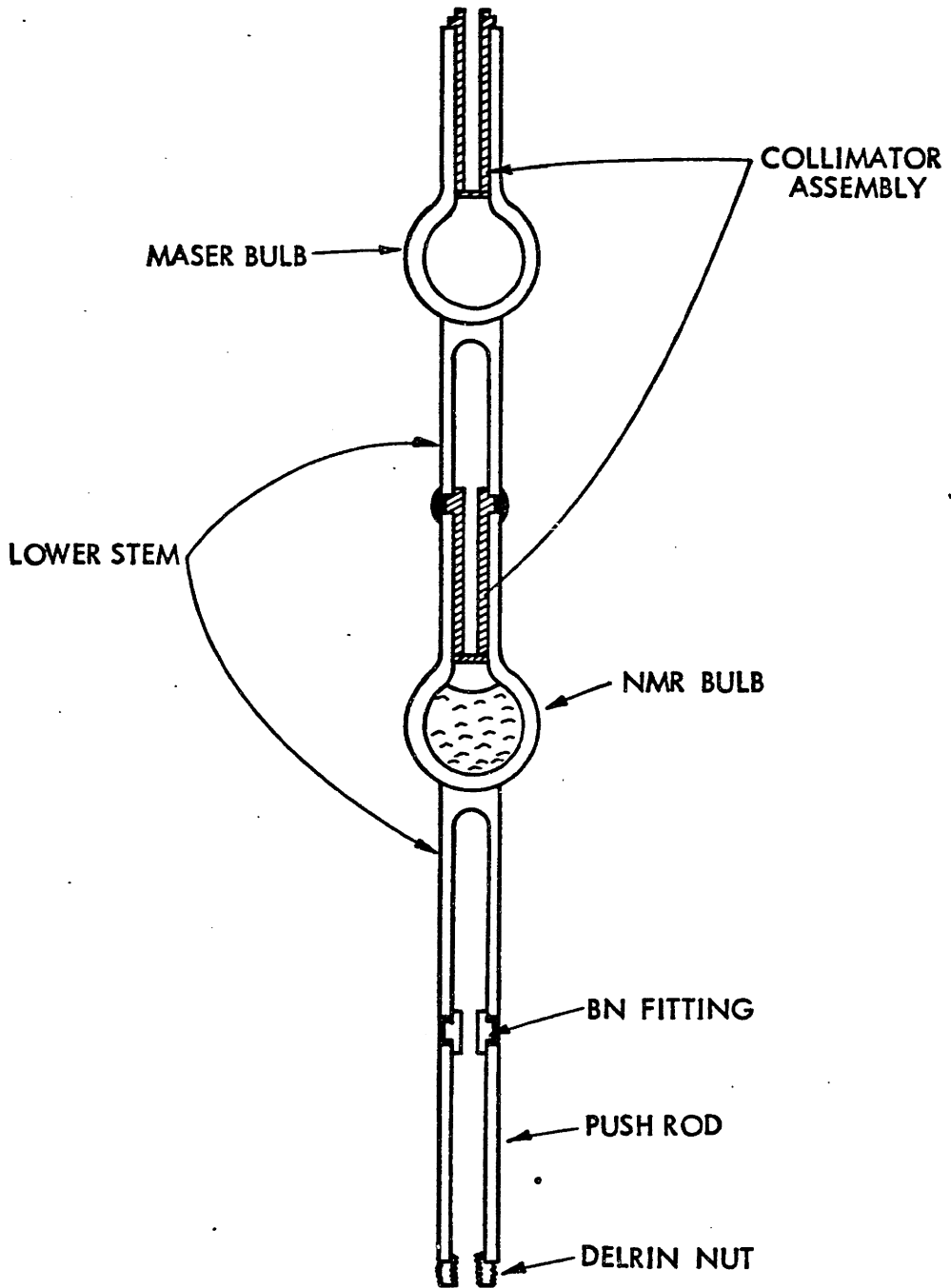


FIG. 5 BULB ASSEMBLY

ting threaded to accept a lead screw.

The NMR bulb was filled with distilled water until the water surface almost touched the collimator. (The meniscus surface is later measured by a procedure described below.) Water does not wet the coated bulb surface, so it is prevented from contacting the collimator and being drawn upward. It is impossible to avoid severe capillary effects with organic liquids which do wet the surface — an important factor in choosing water as the NMR standard.

The entire sample assembly was glued in a cylindrical jig, held by carefully machined collars and rods. The distance between bulb centers, nominally 5.05 cm, was determined from measurements of the stem lengths and glue fitting thicknesses. Optical measurements of the separation agree with these measurements to between 25 and 100 microns.

III.3 Sample Translator

Determining $g_p'/g_j(H)$, involves measuring the NMR and maser frequencies in rapid alternation. This requires that the bulbs be moved quickly and smoothly, and be located accurately. Because the field is significantly distorted by any material, only the bulb assembly can be allowed to move in the interchange procedure.

The mechanism for interchanging the samples is shown in Fig. 6. The bulb assembly moves with a sliding fit in a precision bore quartz tube which extends through the maser cavity. (The fit is so good, that a small flat had to be ground on the

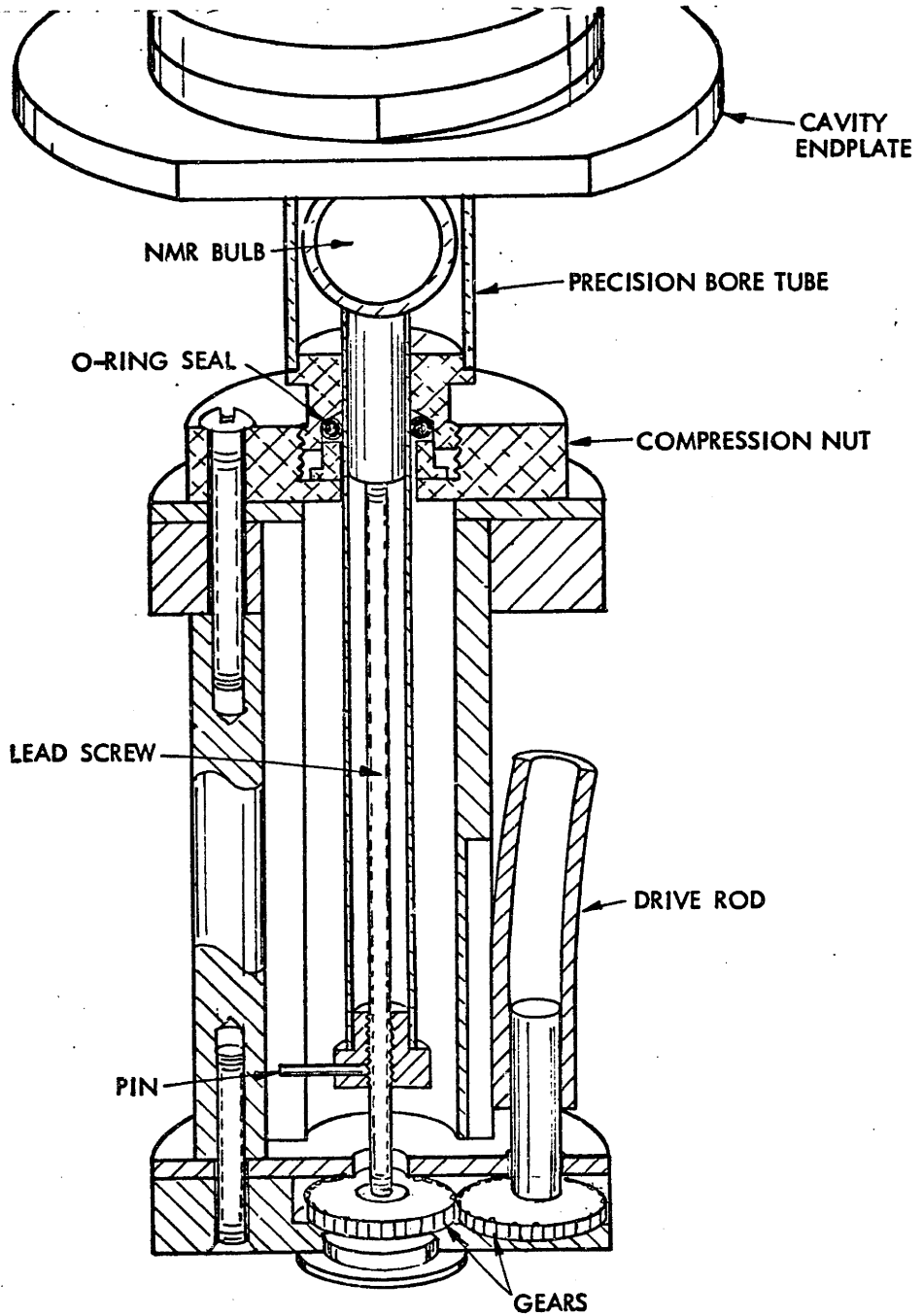


FIG. 6 SAMPLE TRANSLATOR

side of each bulb to allow air to pass during assembly.) In order to reduce loading of the microwave cavity, the O.D. of the tube was ground to 1.550 cm, reducing the wall thickness to .06 cm.

The quartz tube is evacuated. An aluminum O-ring compression fitting, glued to the lower end with Torr Seal, provides a vacuum seal between the tube and the bulb push rod. An acrylic plastic housing for the translator is bolted to the compression nut of the O-ring fitting. A 4-40 (American Standard thread size) aluminum lead screw threads into a Delrin nut at the bottom of the push rod (see Fig. 5). Rotation of the bulb assembly is prevented by a radial pin which rides in a groove cut into the acrylic translator housing.

The lead screw is driven by selected non-magnetic brass spur gears which are driven, via a flexible plastic tube, with a plexiglass drive rod which extends out of the magnet gap. The drive rod, operated manually, is connected to a turns counter which allows the lead screw to be located to 1/20 turn. The bulb positioning was repeatable to within 30 μ .

The only motion of the drive mechanism is rotation of essentially cylindrical parts, so that only the position of the bulb assembly changes with respect to the magnetic field. Therefore only the bulb assembly need be considered when evaluating the effects of material on the magnetic field "seen" by the samples.

As with all components placed in the magnetic field, only selected non-magnetic parts were used in the construction of

the translator. Materials were tested by placing them close to an operating maser bulb. Materials which caused frequency shifts greater than 1×10^{-8} at distances of 4.5 cm were rejected.

III.4 Microwave Cavity and NMR Coil

The requirement that only the bulbs move during the sample interchange puts stringent limitation on the design of the microwave cavity and NMR coil. The coil and cavity must enclose the same volume without interfering with each other excessively; this means that neither a coil nor a cavity of conventional design, one of which would have to be placed inside the other, could be used. Furthermore, the NMR coil must produce a uniform field over the sample volume. We arrived at a design in which the coil itself formed the cylindrical part of the microwave cavity. As shown in Fig. 7 the coil is made from 10 1/2 turns of copper ribbon .07 cm thick and .51 cm wide which were close wound on a 3.9 cm diameter form. Turns were insulated from each other with mylar tape. Coupling holes .48 cm in diameter were made on opposite sides of the coil-cavity.

The endplates shown in Fig. 7 were made of foil segments, about .01 cm thick, fixed to acrylic forms. The endplate is an annular disc about 3.85 cm in diameter with a 1.7 cm hole in the center. The disc is slit along a radius to open the r.f. circuit. Small copper flanges provide capacitance to allow the microwave currents to flow across the gap. The

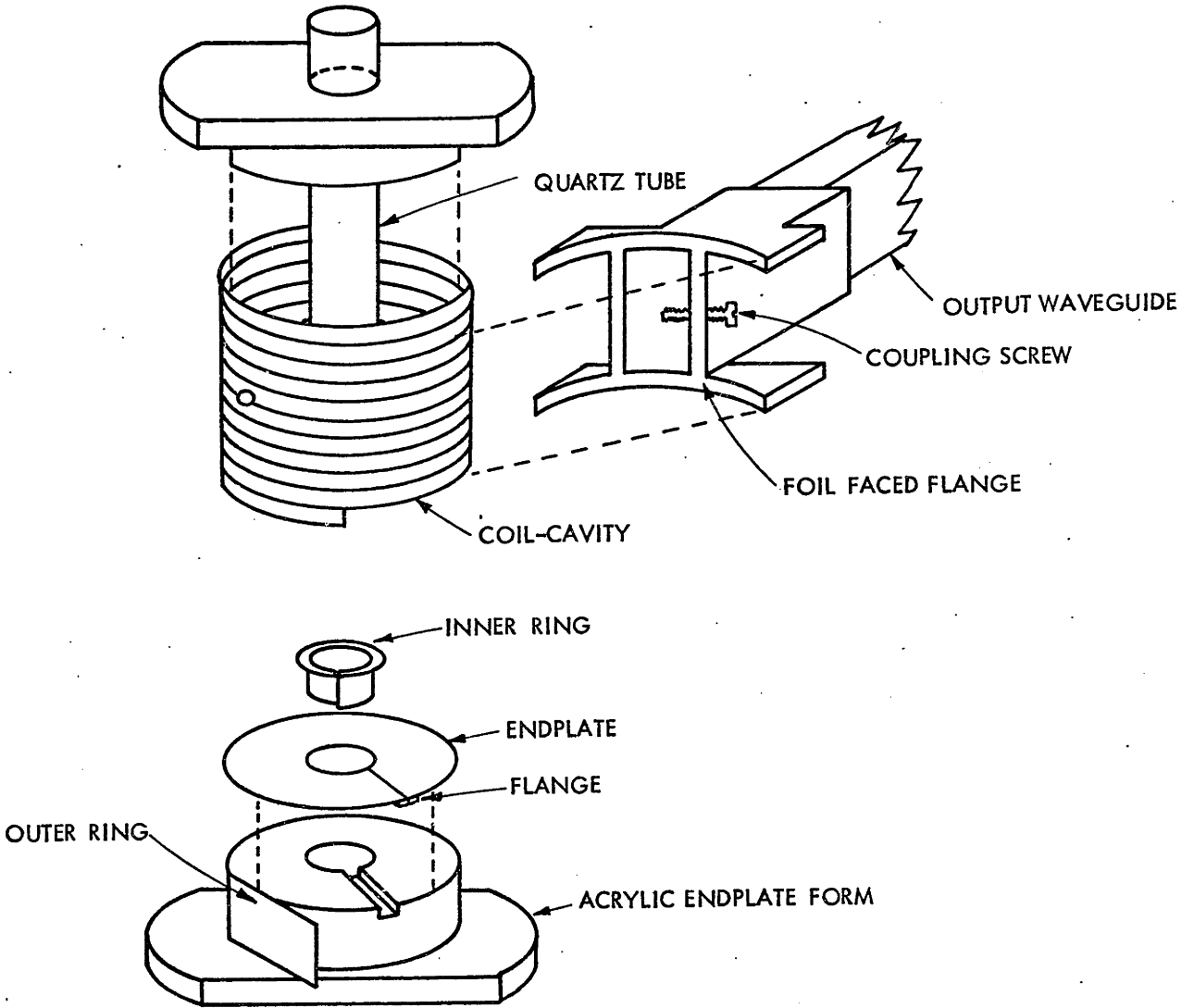


FIG. 7 EXPLODED VIEW OF CAVITY ASSEMBLY

split disc is glued to the acrylic form with "5 Minute" Epoxy (Devcon Corp., Danvers, Mass.). The endplate is completed with foil rings around the outer and inner diameters of the form. These rings, about 1 cm long, prevent loss of microwave energy through the hole or past the joints. The inner ring makes a loose fit around the quartz tube, the outer ring makes a loose fit into the coil-cavity. The rings are insulated at their overlaps with tape or Duro cement to break the tangential r.f. circuit. They are fixed to the acrylic form with mylar or Scotch magic tape.

The quartz tube is vacuum sealed to the upper acrylic endplate form, which in turn is sealed to the evacuated tube which encloses the state selected atomic hydrogen beam.

Energy is coupled to the microwave cavity by ordinary copper X-band waveguides which mate to acrylic flanges faced with copper foil (see Fig. 7). The foil is insulated against direct contact with the cavity to prevent shorting of the r.f. coil. A coupling screw in the output waveguide allows critical coupling. The acrylic flanges are securely bolted to the top plate so that cavity, waveguides and top plate form a rigid structure. The cavity is tuned by adjusting the penetration of the bottom plate. The waveguides are coupled to the rest of the microwave system with standard waveguide flanges separated by a stack of copper and plastic spacers. The copper spacers, slit to prevent r.f. currents, prevent excessive capacitance being coupled to the coil via the waveguides.

The coil is coupled and tuned by means of a capacitor network which joins it to the input and output coaxial cables. The arrangement is shown schematically in Fig. 8. The capacitance values were chosen to give the best output coupling and minimum loading due to input coupling.

The microwave cavity resonates at 9200 MHz in the TE_{011} mode with a Q of about 2000. The coil is tuned to 15 MHz, with a Q of about 20. The r.f. field strength was mapped and found to vary by no more than $\pm 5\%$ peak deviation over the volume occupied by the sample bulb.

III.5 Electronics and Data Acquisition

A simplified block diagram of the maser electronics is shown in Fig. 9. The klystron frequency, $9200 \text{ MHz} - \nu_\ell$, where ν_ℓ is nominally 29.988 MHz or 29.992 MHz, is mixed with a gated signal at 32 MHz to produce pulses at $9232 \text{ MHz} - \nu_\ell$ which drive the electron spins into free precession. Pulse length is adjusted to provide a 90° pulse. The magnetic field is adjusted so that the electron resonant frequency ν_{23} is about 2 kHz above or below the electron drive frequency. The signal radiated at frequency ν_{23} , nominally 9202.01 MHz, is mixed with the klystron frequency to produce an i.f. signal 2 kHz above or below 32 MHz. The i.f. signal is then converted to 2 kHz by mixing with 32 MHz in an audio mixer. A gate eliminates the driving pulse to avoid saturating the audio mixer. The audio amplifier incorporates a lowpass filter with a bandwidth of about 3 kHz. The use of two values for ν_ℓ yields

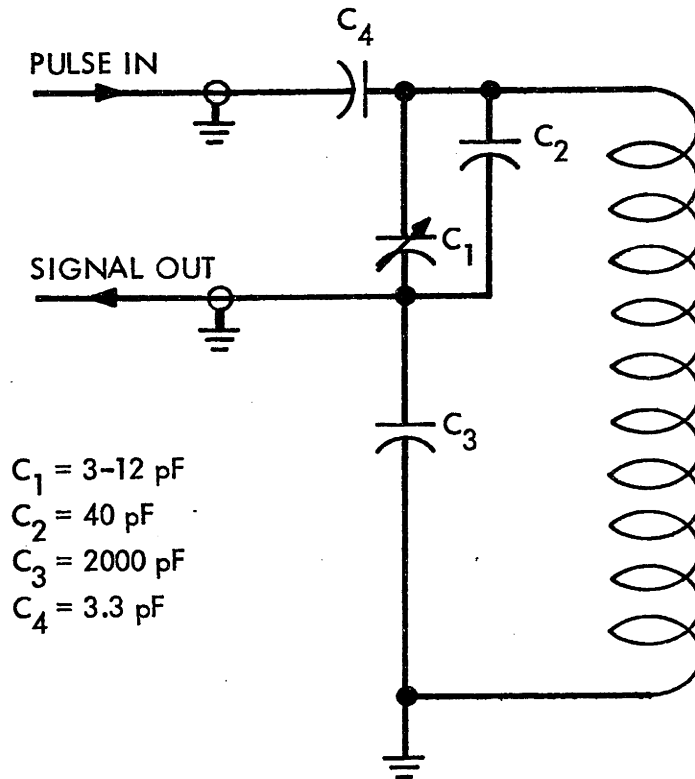


FIG. 8 COIL COUPLING CIRCUIT

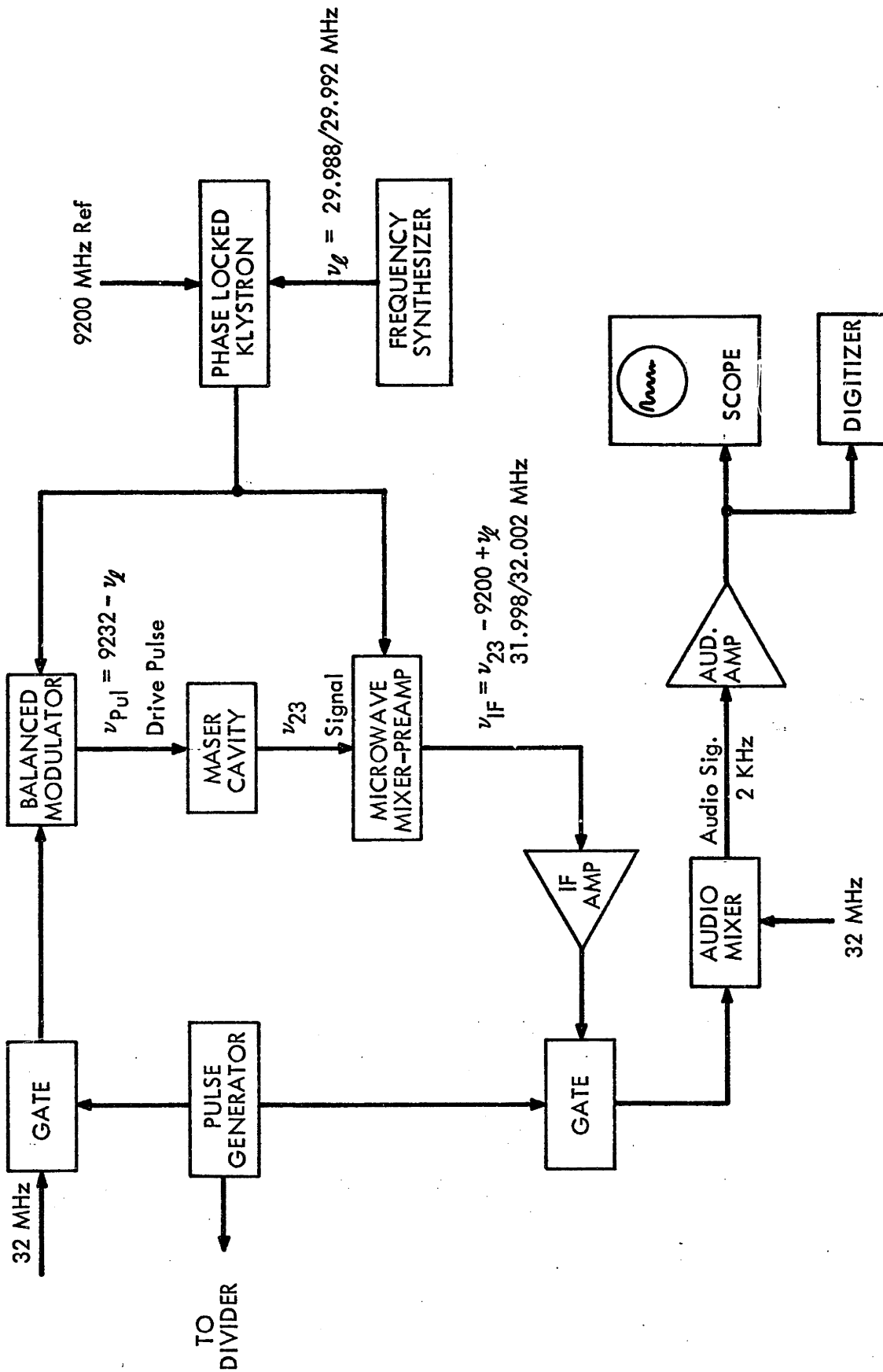


FIG. 9 MASER ELECTRONICS

what are essentially both positive and negative audio beat frequencies, which we refer to as the positive and negative sidebands. By comparing data from the two sidebands we can determine whether any frequency pulling effects exist in the audio detection system. These would show up as a difference in the apparent value of ν_{23} depending on the sideband used.

All of the generated frequencies shown in Fig. 9 are ultimately referred to the laboratory standard, a stable crystal oscillator which is compared periodically with WWVB. The generated frequencies may be taken as exact for the purpose of this measurement, being accurate to better than 1 ppb.

The NMR electronics is shown in Fig. 10. The r.f. driving signal, determined by the frequency synthesizer, is chosen to be about 950 Hz above or below the proton resonant frequency ν_p' . Because of the large offset frequency and since the driving signal is weakly coupled into the coil, it was not possible to achieve a 90° pulse. The output of the coil is critically coupled to a 50Ω coaxial cable which feeds a wideband preamp. A pair of crossed high speed germanium diodes which serve as a limiter, plus a gate, blank most of the driving pulse from the audio mixer; the residual feedthru is minimized by adjusting the phase of the reference to the mixer. The audio signal, ~ 950 Hz, passes through a 100 kHz cutoff lowpass filter into a bandpass amplifier, centered near 950 Hz with a bandwidth of about 60 Hz. Both positive and negative beat frequencies can be used to check for audio pulling effects. All generated frequencies are derived from the laboratory standard.

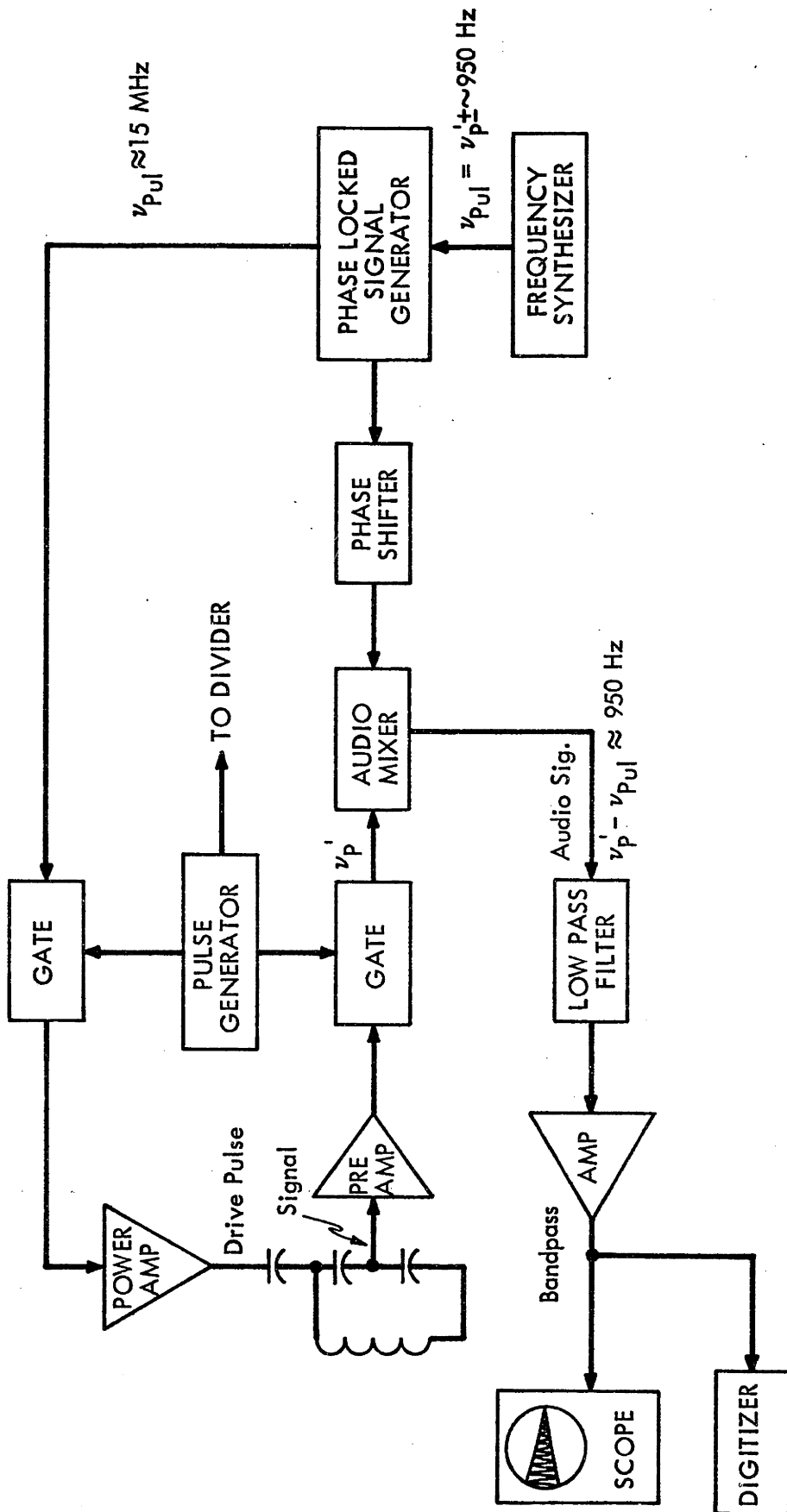


FIG. 10 NMR ELECTRONICS

The data digitization scheme, identical for the electron and NMR signals, is shown in Fig. 11. A 10 MHz signal derived from the laboratory standard is digitally divided by 1202 to produce clock pulses at 8319.46...Hz. The divider is cleared by the pulse which triggers the NMR or maser drive pulse, so that the clock pulses are fixed in time with respect to each free decay signal. The clock pulses trigger a sample and hold circuit which samples the signal; an analog-to-digital converter produces a serial digital signal for each sampled point. This digital signal is read by the computer, a PDP-11/20, via a CAMAC interface system. The maser signals are stored at the ~ 8 kHz rate, the maximum consistent with the conversion rate of the ADC. (The NMR rate is limited to ~ 4 kHz since data must be taken for ~ 1 sec and 4096 points is the largest set which can be fast fourier transformed by the computer.)

Successive signals from either the maser or NMR are averaged by accumulating them in core. After a preset number of signals is accumulated, the averaged data is presented on a storage scope for visual display and transferred to disc storage.

III.6 Procedure

Preparatory to taking data, the resonant frequencies of the NMR coil and maser cavity are adjusted by observing the transmission with varying input frequency. The magnetic field is shimmed for maximum homogeneity by observing the NMR free decay signal while adjusting the current in various electrical

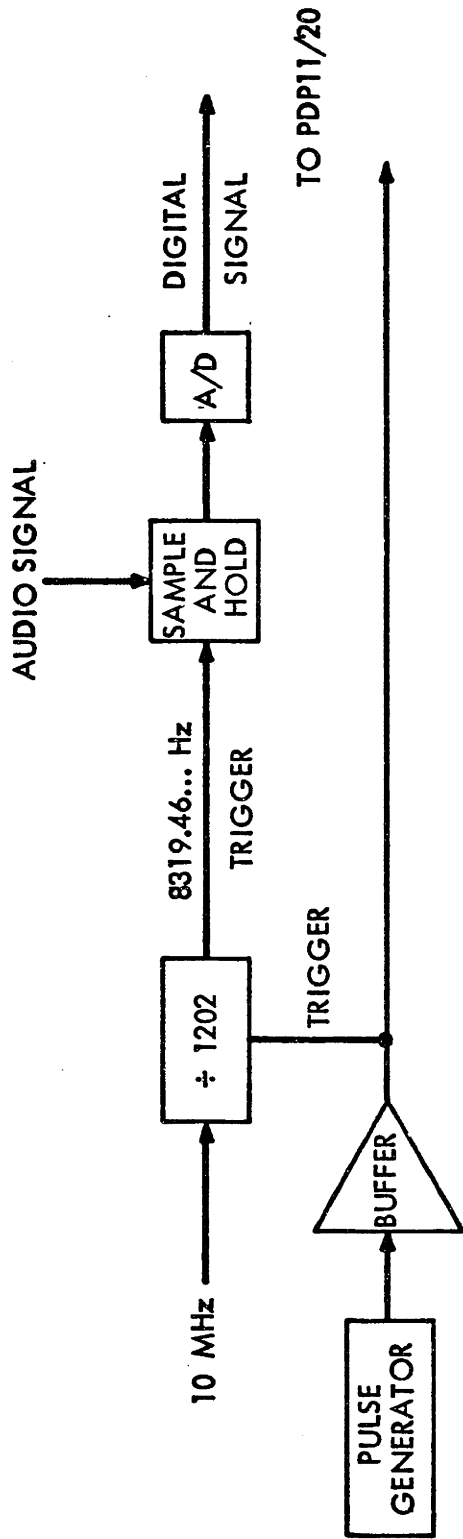


FIG. 11 DATA DIGITIZER

shims. If the signal-to-noise ratio is especially poor or if very fine adjustments are to be made, effects of the shims are observed using computer averaged signals. The NMR pulse length, typically 450 μ sec is set at this time to give the maximum signal. Pulse separation is typically 5 - 10 sec.

The sample assembly is next translated so that the maser bulb is in position. The magnetic field is set to give the desired maser frequency by changing the current through a trim coil. Maser pulse length, typically 100 μ sec, and pulse separation, \sim 10 msec, are also set at this time. The field is not disturbed from the time the field is set until a complete run of data is obtained. Care must be taken, for even moving a steel chair in the laboratory can cause shifts of tens of ppb.

Data taking begins with the maser signal. 256 to 512 maser signals are averaged. Somewhat more than 64 signal points are sampled, of which 64 will be fourier transformed. At a sample rate of \sim 8 kHz the observation time is about 8 msec, adequately long compared to the electron signal lifetime, less than 1 μ sec. Five separate averages are recorded. The klystron lock frequency is adjusted to change the sign of the audio beat frequency and 5 more averages are obtained. Total observation time is about 40 sec or 4 sec per average. Real time is about 80 sec, including the time to change klystron frequency.

The bulbs are next translated to the NMR position by one experimenter, while a second makes the necessary changes in the electronics. Simultaneously, the computer transfers the maser data to magnetic tape. Elapsed time between last maser signal

and first NMR signal is about 3 minutes. Four to nine NMR signals are averaged with 4096 or more points sampled. The observation time per signal is about 1 sec; the NMR signal lifetime is typically 200 μ sec. Three averages are recorded, the NMR drive frequency is changed to reverse the sign of the NMR beat, and three more averages are obtained. Total observation time is about 30 - 60 sec. Real time is about 3 - 6 minutes.

The bulb and electronics change process is now reversed to prepare for another collection of maser data. Five complete cycles of maser and NMR data constitute a run, taking about one hour of real time. The time at which each signal average is completed is recorded by the computer. Occasionally data for one cycle is taken with no signal so that the pulse response of the audio detection system can be observed. Data is limited to 5 cycles by the capacity of a magnetic tape and the stamina of the experimenters. During a complete run the magnetic field would generally drift less than 1 part in 10^7 ; if the drift exceeded this, the klystron frequency would be adjusted to keep the maser audio signal close to its nominal value of 2 kHz. The temperature of the gap was measured from time to time but was never found to depart from 34.7°C .

Two or three runs were often taken during any one night and several nights of data were taken with each bulb configuration. After sufficient data was obtained with a given bulb configuration, the bulb assembly was carefully removed from the apparatus to be measured and photographed.

The sample assemblies were measured for sphericity and the location of the water meniscus was determined using a Jones and Lamson Model FC-14 optical comparator. The set-up is shown in Fig. 12. To avoid optical distortion due to the quartz spheres, the bulbs are placed in a rectangular viewing box with flat windows on four sides. The box is filled with a fluid whose index of refraction matches that of fused quartz (trichloroethylene and isopropanol or glycerol and water can be mixed to achieve the proper index). Bulbs can be checked for sphericity by comparing the enlarged images in various orientations with a circular template. The meniscus in the NMR bulb is clearly visible if a diffuser is used between the mercury arc source and the bulbs, and may be photographed by placing a film holder in the image plane. A magnification of $\times 10$ is used for the photographs.

The object table of the comparator is rotatable and mounted on ways which translate in directions orthogonal to the optic axis. Thus the distance between the bulbs can be accurately determined. The average pitch of the lead screw in the sample translator is also measured using the optical comparator.

When the measurements on the bulbs are completed, the bulb configuration is switched with each collimator and collimator holder staying with their respective bulbs. The epoxy joint between the two bulbs and the joint to the push rod (see Fig. 5) are broken by heating. The NMR bulb is emptied and recoated and all old epoxy is removed from the joints. If the boron-

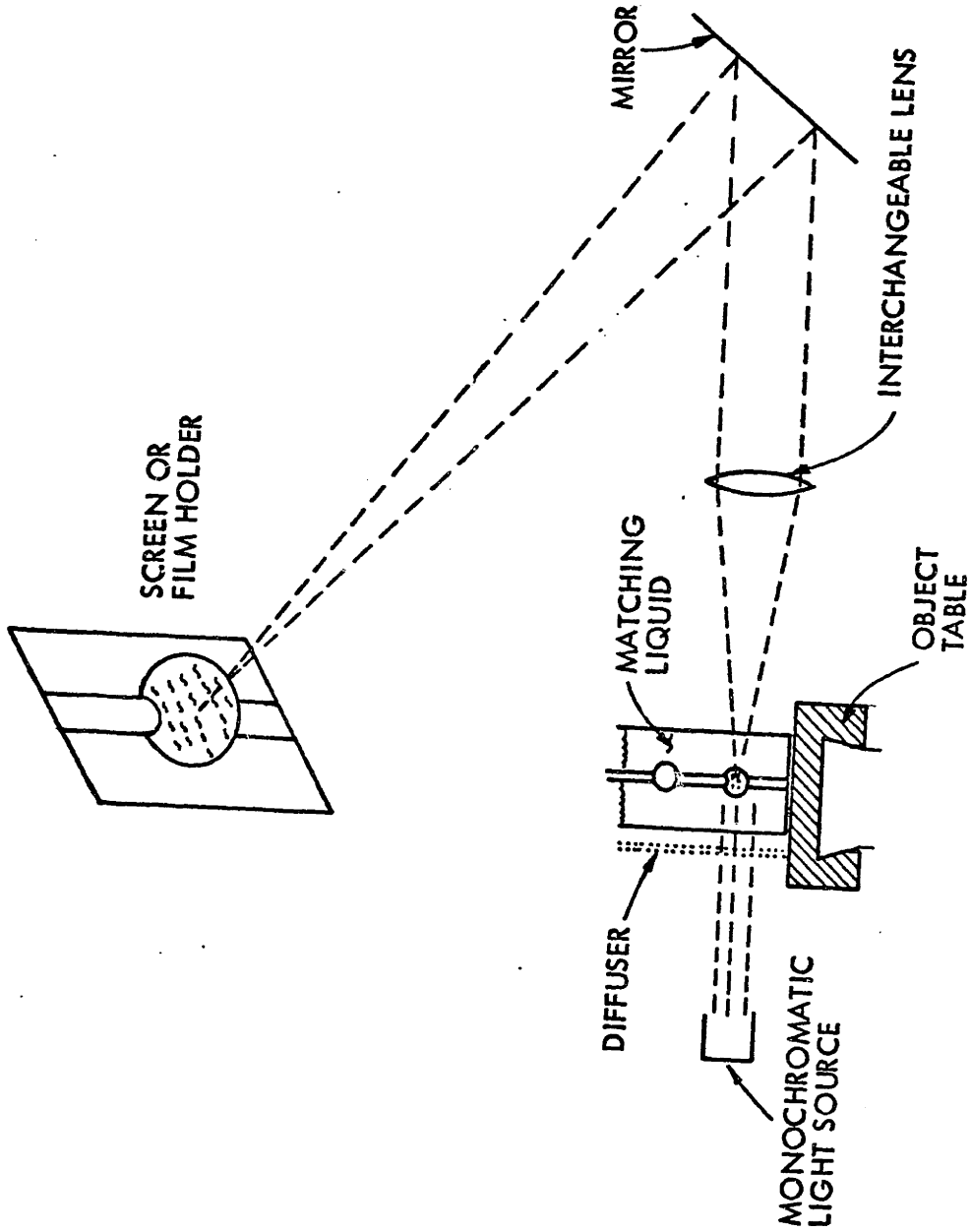


FIG. 12 BULB MEASUREMENT SET-UP

nitride fittings are destroyed in the disassembly process, new ones machined to the same dimensions are installed. If a collimator separates from its holder, it is cleaned, re-coated and re-mounted. The reassembly of the bulbs in reversed positions is according to the procedures already discussed. Data is taken on each of the two possible configurations for each of the pairs of bulbs.

IV. RESULTS AND ANALYSIS

In this section we describe the plan for analyzing the data, give details on the procedures for treating the electron and proton signals, describe various systematic corrections, and present the final result.

IV.1 Plan

- 1) Raw data for each cycle of 4 or 5 sample interchanges in a given run are fourier transformed to provide a series of beat frequencies, both positive and negative. Proton or electron frequencies in each interchange cycle are calculated from the beat frequencies and the results are then averaged separately for each sideband. The values for the positive and negative sidebands are then averaged together, yielding a set of four or five electron and proton frequencies, one pair for each interchange cycle. These frequencies represent averages over periods of a few minutes in the course of an hour, during which the magnetic field may have drifted appreciably.
- 2) The electron and proton frequencies are combined to give a series of values for $g_j(H)/g_p'$ in a manner which eliminates first order effects of field drift. The results are averaged to give a final value of $g_j(H)/g_p'$ for that run.
- 3) The procedure is repeated for a number of such runs taken over several days. The sample holders are then dismantled, the geometry of the water sample is measured photographically,

and the sample holders are reassembled with their roles interchanged.

- 4) The procedure is repeated with the new configuration.
- 5) The results for all the runs in each configuration are averaged.
- 6) Corrections are made for the systematic errors for each of the two configurations.
- 7) The corrected results for the two configurations are averaged, yielding a final value of $g_j(H)/g_p'$ for the set of sample holders.
- 8) The entire procedure is repeated with a second set of sample holders to check for consistency. The results of the two determinations are combined to yield a final value for $g_j(H)/g_p'$.

IV.2 Analysis of the Electron Signal

The first few points of the electron signal are discarded to avoid effects of the driving pulse, and a set of 64 consecutive points is selected for fourier analysis. Fig. 13 shows the first 32 points of a typical maser signal, the average of 256 individual sweeps taken over a 2.5 sec interval. (The signal-to-noise ratio for individual sweeps, as observed on an oscilloscope during data taking, is unity.) The fourier transform of this signal is shown in Fig. 14.

The solid line is the least squares fit to a lorentzian

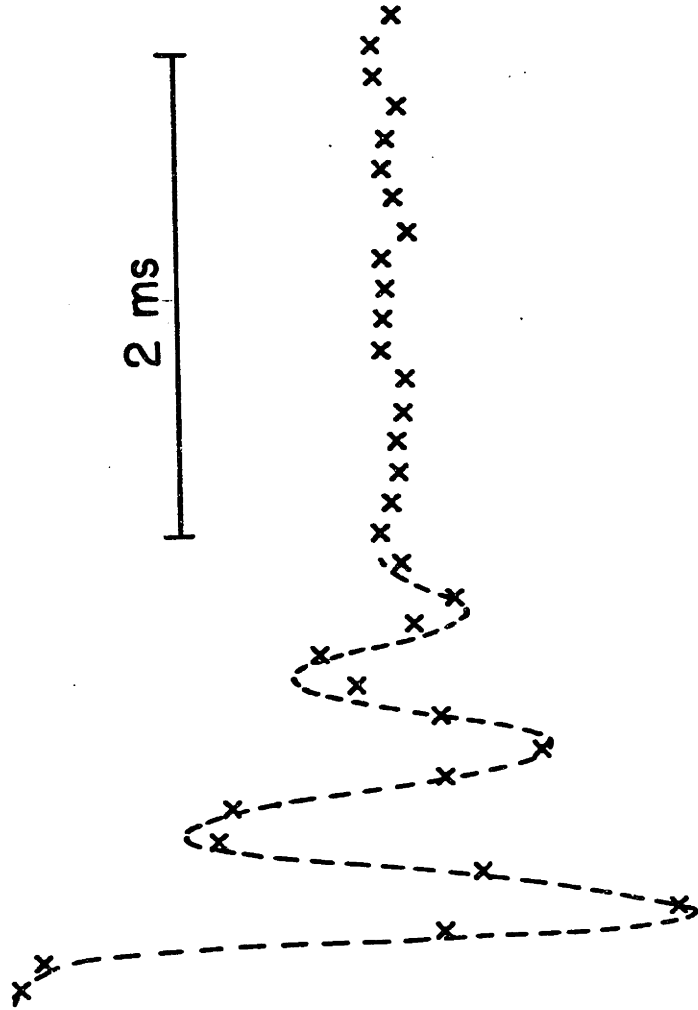


FIG. 13 MASER SIGNAL

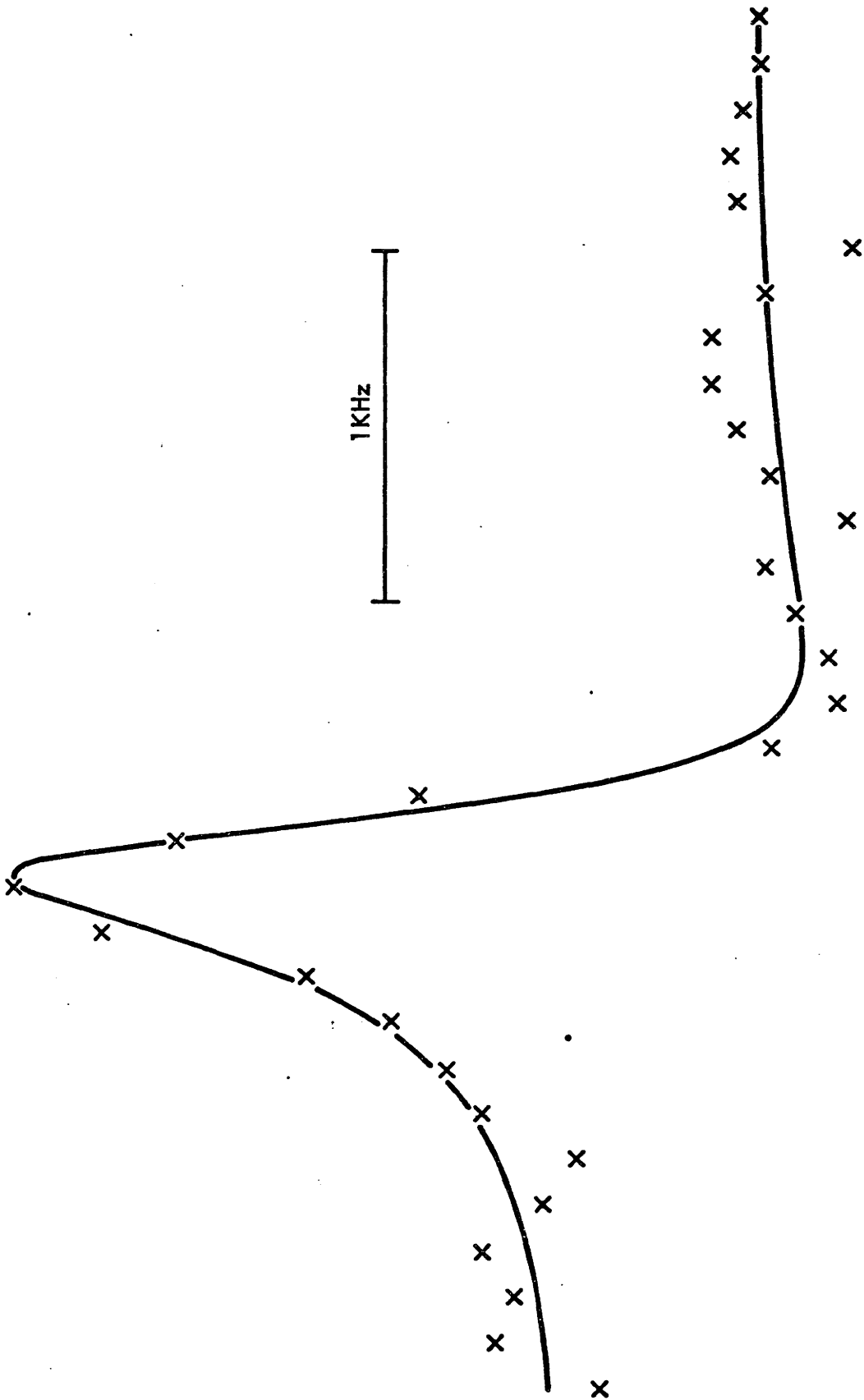


FIG. 14 TRANSFORM OF MASER SIGNAL

absorption dispersion curve which has been modified for effects of the image and several periodic repetitions. (The effect of the second periodic repetition is less than 1 ppb.) The rms scatter of points about the fitted line represents a S/N of 15, as expected for a 256 sweep average of a free decay signal with S/N = 1. The fit corresponds to an absorptive full width at half maximum of about 500 Hz. Note that this linewidth represents only 50 ppb in the electron frequency, so that even with S/N = 15 (which is lower than average), we can determine the line center to a precision of a few ppb with a single determination. The standard deviation of the frequency fit to consecutive maser signals is typically 4 ppb, which is consistent with the known average magnitude of field fluctuations over the few seconds separating the measurements.

The mean difference between the results obtained from positive and negative sidebands for any one run is typically less than 2 ppb with a standard deviation of 4 ppb. Averaged over all the runs the discrepancy is less than 1 ppb indicating that audio frequency pulling effects are negligible.

The field coupled part of the electron frequency is calculated from each measured maser frequency by solving Eq. (11a) for ν_j . This is done numerically using for the hyperfine frequency $\nu_0 = 1420.405\ 751\ 768(2)$ MHz (HEL70) and for the electron-proton g-factor ratio $g_j(H)/g_p(H) = 658.210706(6)$ (WIN72). For a maser frequency of 9202 MHz the field coupled frequency

is 9861 MHz.

IV.3 Analysis of the Proton Signal

The proton resonance spectrum is obtained by taking the fourier transform of 4096 points from each NMR signal average. The first 32 points, representing an 8 msec period, are discarded, to eliminate effects of the driving pulse. (The long delay is required because of ringing of the audio bandpass amplifier.) Failure to discard the initial points can lead to frequency shifts of tens of ppb when the pulse leakage is great. Additional delay beyond 8 msec produces no shifts statistically significant at the level of 3 ppb.

Fig. 15 shows a typical NMR signal, the average of 9 sweeps. (To avoid confusion only every fifth point is displayed.) Fig. 16 shows a small portion of the fourier transform of this signal; the real and imaginary parts have been combined to give a purely absorptive line using Eq. (18). The number of points per resonance linewidth is proportional to the number of decay lifetimes observed. Because of the high sampling rate and limitations imposed by computer storage capability, the 4096 data points cover only about five lifetimes. The resulting relatively small number of points within the resonance width, however, does not represent any loss of information and does not interfere with accurate analysis.

The phase ϕ , is determined by optimizing the line symmetry

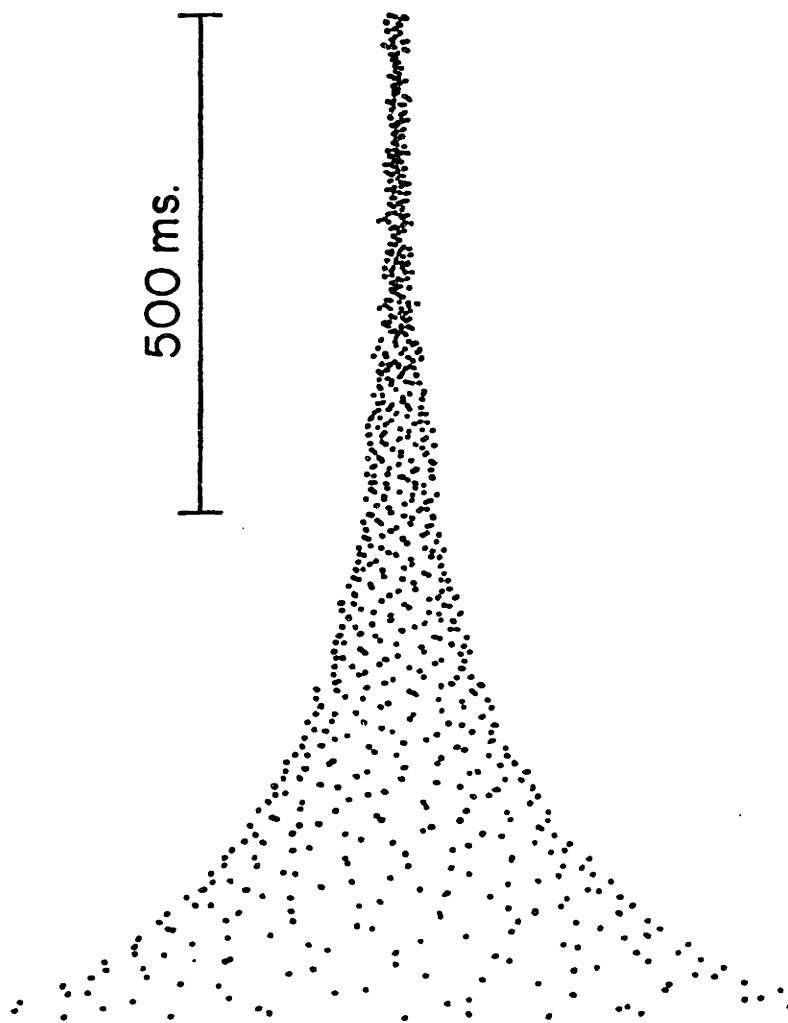


FIG. 15 NMR SIGNAL

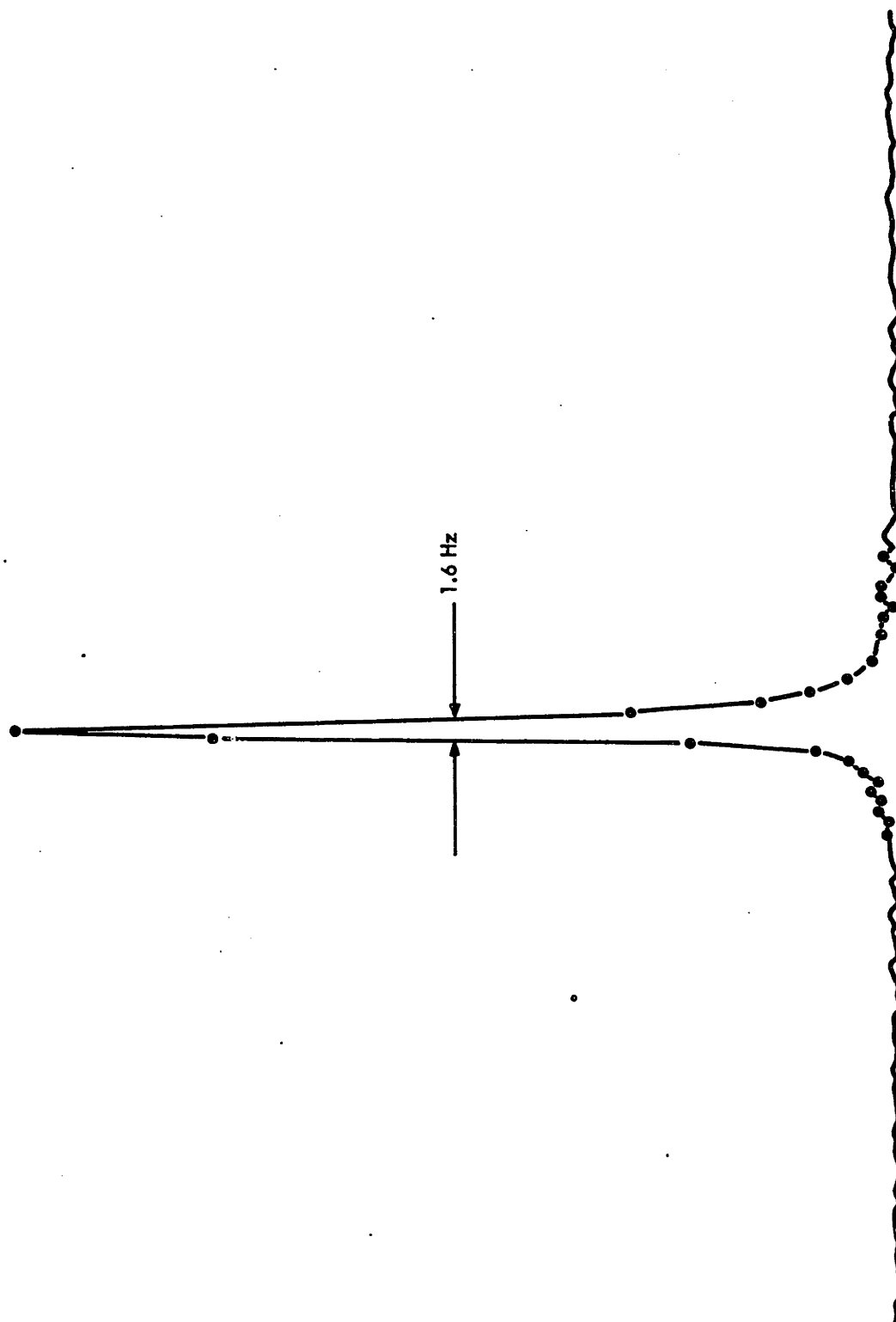


FIG. 16 TRANSFORM OF NMR SIGNAL

as follows: twenty points on each side of the assumed line center are compared, the closest of these being 10 points from the center. (The points are separated by about 1 Hz, so that the comparison points are in the far wings of the resonance.) The phase is chosen to equalize the values of these points, properly weighted about the assumed line center. The true line center is then determined by integrating the absorptive line over a region 60 points wide, symmetric about the assumed center, according to Eq. (17). The process is iterated, using the calculated center to determine a new center for symmetrization and integration intervals.

The fractional linewidth of the NMR signal is about 100 ppb, and with S/N greater than 100 one might expect the standard deviation of a single determination of the centroid to be about 1 ppb. This is not in fact achieved, since the phase-finding routine operates in the wings of the line where the S/N is much lower than 100. The average scatter for successive NMR measurements is 13 ppb. Part of this scatter is attributable to field fluctuations over the few minute intervals between measurements, but much of it is due to statistical error in the phase-finding routine.

Line centers for positive and negative beat frequencies agree well, the typical average difference for one run being 8 ppb with a standard deviation of 14 ppb, indicating no significant pulling effects. The mean difference between results

from positive and negative sidebands averaged over many runs is about 1 ppb with a scatter of 10 ppb, which supports this conclusion.

The reasoning behind the choice of the symmetrization interval for determining the phase is as follows: 20 Hz (1300 ppb) about the center of the resonance are excluded since the NMR line might reasonably be expected to be broadened by field inhomogeneity over this region and therefore not be necessarily symmetric. The use of twenty points for averaging is to provide adequate signal-to-noise. These choices are by no means unique. Since this could be a potentially serious source of error we have reanalyzed a large portion of the data by other means to check the correctness of the analysis method. This reanalysis, described in the appendix, indicates that our symmetrization analysis is accurate to a few ppb.

IV.4 Corrections

Table 1 shows the results for $g_j(H)/g_p'$ from every run. (The configuration is designated by the NMR bulb.) Each result is based on 6 or 8 frequency ratios, as described in Sec. IV.1; the error is the standard deviation of those values. No data has been discarded.

The mean of a configuration is the unweighted average of results for all the runs. The uncertainty is the standard deviation of these results.

Table 1
Results of all Runs

<u>Date</u>	$\underline{g_j(H)/g_p}$	<u>Date</u>	$\underline{g_j(H)/g_p}$
	Configuration #1		Configuration #3
12 Nov 74	658.216 0697 (57)	30 Nov 74	658.215 9775 (42)
13 Nov 74	6 0794 (24)	30 Nov 74	5 9758 (47)
13 Nov 74	6 0945 (151)	30 Nov 74	5 9759 (30)
14 Nov 74	6 0608 (206)	01 Dec 74	5 9839 (62)
14 Nov 74	6 0763 (50)	01 Dec 74	5 9715 (41)
14 Nov 74	6 0714 (58)	01 Dec 74	5 9768 (35)
	Configuration #2	07 Dec 74	5 9786 (46)
20 Dec 74	6 0325 (45)		Configuration #4
21 Dec 74	6 0407 (20)	15 Dec 74	6 0786 (41)
21 Dec 74	6 0409 (20)	15 Dec 74	6 0738 (23)
22 Dec 74	6 0393 (33)	16 Dec 74	6 0658 (58)
24 Dec 74	6 0387 (47)	16 Dec 74	6 0742 (59)
24 Dec 74	6 0349 (78)	17 Dec 74	6 0654 (40)
16 Jan 75	6 0430 (22)	17 Dec 74	6 0757 (42)
16 Jan 75	6 0374 (38)		

Configuration Means

#1	658.216 0754 (113)
#2	6 0384 (34)
#3	5 9771 (37)
#4	6 0723 (54)

Each of the configuration results must be corrected for various systematic errors associated with the given configuration. A summary of the corrections and their uncertainties is given in Table 2. (The statistical uncertainties shown are those of the configuration means given in Table 1.) We describe below each class of correction.

Shape Correction

This correction accounts for the distortion in the field of the NMR sample due to the intrusion of the meniscus into the assumed spherical shape. The correction is based on measurements from the photographs of each bulb and meniscus made after data taking.

A drawing based on one of the photographs of bulb #4 is shown in Fig. 17. Even though distortion due to the outside quartz surface is eliminated by the matched refractive index fluid in the viewing box (see Section III.6), there is still a distortion or lensing effect due to the spherical interface between the water and the quartz. Because the surface is spherical it is easy to calculate the effect based on the indices of refraction of water and quartz. By ray tracing we have mapped the observed meniscus into the true meniscus shown as a dotted line. The extension of the spherical surface of the bulb and the position of the collimator are also indicated.

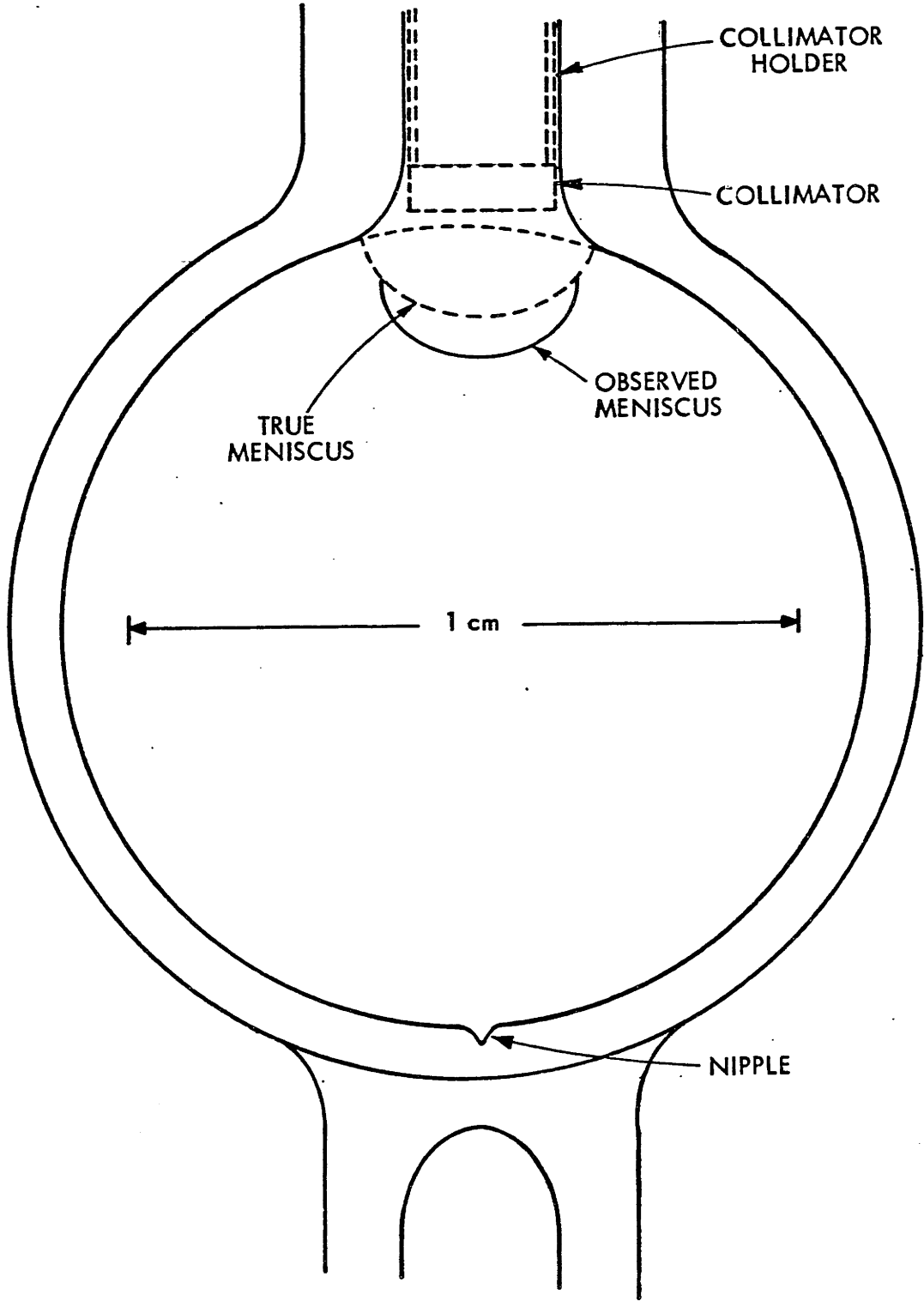


FIG. 17 NMR BULB

Table 2

Corrections and uncertainties in $g_j(H)/g_p'$, ppb

Configuration	1	2	3	4
Statistical	(17.2)	(5.2)	(5.6)	(8.2)
Shape	-47.1 (15.6)	-41.2 (13.7)	-14.9 (5.0)	-8.5 (2.9)
Gradients	-29.8 (9.9)	-26.6 (8.8)	-10.5 (5.3)	-4.0 (2.4)
Collimator	8.1 (4.0)	8.1 (4.0)	2.7 (1.4)	2.7 (1.4)
H ₂ O diamag.	-7.6 (1.5)	-7.6 (1.5)	-7.6 (1.5)	-7.6 (1.5)
Ambient	(5.0)	(5.0)	(5.0)	(5.0)
Other	(11.6)	(11.6)	(3.8)	(3.8)

Once the meniscus is measured, its effect is calculated as follows: It is a well known result from electrostatics that a dielectric sphere placed in a uniform field becomes uniformly polarized with a uniform interior field. This result also applies to a diamagnetic sphere in a uniform magnetic field. We have modeled the NMR sample as the superposition of a uniformly magnetized sphere and an oppositely magnetized section occupying the volume between the true sample and the sphere. The meniscus surface is approximately spherical; the meniscus region is the intersection of this sphere with the bulb sphere. We calculated the dipole, quadrupole and octopole moments of the meniscus region using the center of the meniscus sphere as the origin. The susceptibility of water is taken to be (CRC62)

$$\chi = -4\pi \times .72 \times 10^{-6} \quad (19)$$

where χ is defined by

$$B = \mu_0 H(1 + \chi) \quad . \quad (20)$$

The average contribution to the field of these multipole moments in the sample region is calculated numerically. The octopole contribution is only a few percent of the dipole contribution, and the expansion is safely terminated with that term. Results for the shape correction are shown in Table 2.

The error has been assigned from estimates of uncertainty in the determining the meniscus geometry, errors in the numerical procedures, and effects of uncalculated terms. The corrections, and their uncertainties, are smaller for bulb Pair B because their smaller necks result in smaller menisci.

Gradient Corrections

The next class of corrections arises because the hydrogen atoms sample the field in the portion of the maser bulb which corresponds to the meniscus region of the partner NMR bulb. Local field gradients produced by the bulb assembly cause the field in this region to differ from the field in the rest of the bulb. Assuming a uniform ambient field at the maser bulb we have calculated numerically the average field in the bulb and in the meniscus region due to the diamagnetism of all components within about 2.5 cm of the bulb center. These include the upper and lower stems, the collimator, and deviations of the bulb itself from a spherical shell which produces a uniform interior field. The component materials are all assumed to have the susceptibility of fused quartz:

$$\chi_{\text{Quartz}} = -4\pi \times 1.08 \times 10^{-6} \quad (20)$$

based on a molecular susceptibility of $-4\pi \times 29.6 \times 10^{-6}$, and a density of 2.2 g/cm^3 (CRC62). (The collimator has 50% transmission and is assumed to have half the susceptibility of

quartz.) The major contribution is from the upper stem; the contribution from the lower stem is opposite in effect, but much smaller. Small contributions arise from the collimator and the missing bulb wall above the meniscus. The sum of all these corrections is indicated in Table 2. The error is based on the uncertainties in the approximation of various components with simple geometric forms, neglect of ambient gradients, and uncertainty in the susceptibility of non-quartz materials such as the glass collimator. As in the shape corrections, the gradient corrections are smaller for the small necked bulbs since the relative contribution of the smaller meniscus region is less.

Collimator

The third source of error arises because the hydrogen atoms sample the collimator volume and "see" a different field due to the shielding effects of the collimator. The collimator is modeled as an infinite disc parallel to \vec{H} with half the susceptibility of quartz (to account for the holes). The field inside the holes, taken as infinite cylinders, is calculated on the basis of the ambient field in the disc. The atom density is assumed to be half the density of the bulb. The error is based on uncertainties in the approximations involved in determining the collimator field, and in neglecting the effects of gradients in the ambient field. The smaller collimator of bulbs 3 and 4 account for the smaller correction compared to bulbs 1 and 2.

Water Correction

While the difference in fields "seen" by the two samples due to differences in the bulbs is cancelled by interchanging the bulbs, differences caused by diamagnetic effects of the contents of the opposite bulb is not. We calculated the field at the maser bulb due to the dipole moment of the water in the NMR bulb. Since the distance between the bulbs is comparable to the separation of the magnet pole pieces, the effect of the pole pieces was also considered. This was done by assuming an infinite permeability for the iron pole pieces and calculating the effects of the images of the water dipole in each pole piece, as well as the images of images. Convergence is rapid; the effect is to increase the shift 30% over the value in the absence of pole pieces. The correction is the same for all configurations.

Miscellaneous Corrections

There remain a number of corrections, difficult or impossible to calculate, whose magnitude we estimate and include as an additional uncertainty.

Uncertainty in the field in the volume of the maser bulb above the meniscus region and below the collimator contributes an uncertainty of 11 ppb in set A and 2 ppb in set B. This estimate is based on the size of the region and the magnitude of possible gradients estimated from stem gradient calcula-

tions. Deviations from sphericity in the overall shape of the bulbs, based on comparison of bulb photographs with photographs of ball bearings using the same optics, are of the order of 10^{-3} . The contribution to the uncertainty is determined from a comparison of the internal fields of polarized spheres and ellipsoids (see, for example, STR41) and is 1.5 ppb for all bulbs. (The effect of the dimple at the bottom of the bulb, shown in Fig. 17, is negligible, being about .1 ppb.) Effects of non-uniformity of bulb wall thickness are 2 ppb for set A and negligible for set B. Errors due to positioning the bulbs incorrectly in the field are estimated at 2 ppb based on known errors in the bulb separation measurements, and the measured frequency shifts when the bulbs were moved (less than 3 ppb per .06 cm). Estimated error in the NMR frequency determination procedure, based on comparison with alternative methods, is 2 ppb (see Appendix).

When #3 was used as the NMR bulb, a little water was found in the region between the collimator holder and the bulb stem. The volume was estimated at about 10^{-3} of the bulb volume. It is not known whether the water was there during measurement or got there during removal of the bulbs from the magnet. The field might be as much as 10^{-6} different in the neck region, so we add 1 ppb additional uncertainty.

We have computed the effect of cavity mistuning on the maser signal. The pulling is given in terms of the cavity and

line Q's, the mistuning, and the ratio of H atoms flux to the threshold flux (WIN72, PHI72). Estimating our flux on the basis of earlier work (WIN72, WAL72) and scaling to our cavity and bulb size yields a maximum error of 0.1 ppb. The theory of cavity pulling may be generalized to the NMR signal (PHI72). A pessimistic estimate leads to a limit of error of 1 ppb.

The presence of hydrogen atoms in the neck above the collimator is not important since these are quickly relaxed due to collisions with the uncoated surfaces. Relaxation due to escape is also greater in the neck since there is no collimator to prevent escape.

The glue joint which joins the two bulbs together is different for each configuration. The total effect of glue diamagnetism is of the order of 1 ppb, and differences from one configuration to the next should be negligible.

Errors due to gradients in the ambient field were estimated by applying gradients of known distribution sufficient to double the NMR linewidth, and comparing the results obtained with those in the best shimmed field. Gradients linear along one of axes parallel to the pole faces were applied on the second run of 13 Nov and the third run of 14 Nov. In neither case was the difference from the configuration mean significantly altered by the applied gradient. Unfortunately, the statistical error for this configuration is tens of ppb. The first run of 01 Dec had a gradient quadratic along a radius

vector in the plane of the pole faces. In this case, the statistics are better, 8 ppb, and the shift is 9 ppb. The most likely mechanism for ambient gradients affecting the result is non-uniformity of the NMR r.f. field. If portions of the bulb which "see" different fields do not contribute equally to the signal, the signal will not reflect the average field. Since non-uniformities in the r.f. field are expected to be symmetric about the coil center, only symmetric inhomogeneities can affect the result through this mechanism. Measurements of r.f. intensity variations give a maximum value of 5%. For NMR widths of 1.5 Hz we therefore estimate a maximum error of .075 Hz or 5 ppb, consistent with observations with the applied quadratic gradient. It is important to note that any measurement of a gradient effect is an upper limit, for it assumes that all the ambient gradient affecting the linewidth is of the nature of the applied gradient. In addition, it is clear that the distribution of gradients changes from day to day, so some averaging of the effects might be expected. For these reasons, we feel that 5 ppb is a reasonable uncertainty to ascribe to effects of ambient field gradients.

IV.5 Final Results

The two corrected results for each pair of bulbs are averaged to cancel the remaining effects of the sample holders. Care must be taken in computing the uncertainty of this

averaged result because the uncertainties for the two bulbs of a pair are not independent. In fact, since the meniscus and collimator are similar within a pair, the corrections and uncertainties are almost the same. The contribution of the uncertainties in these corrections to the average is computed by averaging the uncertainties for each bulb. The statistical error is taken to be the rms scatter of the run results from their configuration mean, averaged over both configurations of the pair. Statistical error is added quadratically to the rest of the error. The results of this procedure are the pair results shown in Table 3. The difference between the two pairs is only 1 ppb. Since the corrections applied to Pair A are much larger than those for Pair B, the good agreement is evidence that the correction procedure is valid.

The final result is the weighted mean of the two pair results. The relative weighting of the pair results is based only on those errors which are independent. We assume the errors based on the size of the meniscus and collimator to be independent since these are so different between the two pairs. Errors such as those due to ambient field gradients, water diamagnetism, and NMR frequency determination, which are the same for each pair are not included in the weighting. The error in the final result due to the errors which are independent for the two pairs is given by

Table 3

Corrected values of $g_j(H)/g_p'$

Single Configuration Results

1: 658.216 0251 (188) (29 ppb)
2: 658.215 9941 (142) (22 ppb)
3: 658.215 9572 (75) (11 ppb)
4: 658.216 0608 (74) (11 ppb)

Pair Results

A: 658.216 0096 (162) (25 ppb)
B: 658.216 0090 (72) (11 ppb)

Final Result 658.216 0091 (69) (10 ppb)

$$\sigma_{\text{ind}}^{-2} = \sigma_{\text{A,ind}}^{-2} + \sigma_{\text{B,ind}}^{-2} \quad (21)$$

The total error is found by adding the remaining non-independent errors quadratically to the independent errors. The final result is

$$g_j(\text{H})/g_p' = 658.216\ 0091(69) (10 \text{ ppb})$$

at a temperature of 34.7°C. The uncertainty has the significance of a 70% confidence interval.

Some small differences between some of the figures in Tables 2 and 3 and those published earlier (PHI75) are due to the inclusion in the present work of data from some runs which had not been analyzed at the time of the earlier publication. None of the differences are statistically significant, and the final result is unchanged.

V. DISCUSSION

V.1 Previous Work

A review of the history of measurements of $g_j(H)/g_p'$ has been given by Cohen and Taylor (COH73). The most accurate measurement prior to this work is by Lambe and Dicke (LAM59) who compared the electron transition in hydrogen, using electron spin resonance, with the NMR frequency of a spherical water sample. The electron resonance width was 20,000 Hz, and the S/N was 8 in contrast to the present work, for which the figures are 600 Hz and 100 respectively, for comparable observation times. The result was:

$$g_j(H)/g_p' = 658.215\ 9088\ (436)\ (66\ \text{ppb}) \quad (22)$$

to be compared with our result:

$$g_j(H)/g_p' = 658.216\ 0091\ (69)\ (10\ \text{ppb}) \quad (23)$$

The two results differ by 152 ppb, or more than twice the estimated uncertainty of the Lambe-Dicke result. There are several possible explanations for the discrepancy.

The uncertainty quoted by Lambe and Dicke is based on the standard deviation of the mean of about 50 measurements for each of two electron transitions in hydrogen. The statistical error was doubled to account for possible systematic errors, suggested by a correlation between the results and operating conditions of the hydrogen discharge. We feel that adoption

of an error based on the standard deviation of the mean of a large number of measurements is overly optimistic when there is the possibility of a systematic error buried in the scatter. Thus, the assigned error in the Lambe-Dicke experiment is probably too small.

Another explanation for the discrepancy is the effect of sample temperature. As discussed below, the proton moment in water decreases with temperature at a rate of about 10 ppb/ $^{\circ}\text{C}$. While our operating temperature was stabilized at 34.7°C , the temperature of the Lambe-Dicke sample, the ambient laboratory temperature, was not measured (LAM75). Another possible source of error is diamagnetism in the cylindrical neck of the Lambe-Dicke sample holder. We estimate that bulk diamagnetism of the Teflon sample holder would reduce the field in the neck relative to the bulb by about 1000 ppb. The neck volume was about 15% of the total volume, which would affect the observed hydrogen frequency by 150 ppb. (This effect is similar to the gradients and collimator effects of our Table 2, which total only 22 ppb in the worst case.)

V.2 Temperature Effects

The effective moment of the proton in water is affected by temperature due to change in density and the degree of molecular association. The temperature dependence has been measured by Hindman (HIN66) over the range $-15^{\circ}\text{C} < T < 100^{\circ}\text{C}$.

The measurements were made in a cylindrical sample and corrected for shape effect to a spherical sample using data on the temperature dependence of the magnetic susceptibility of water. We have obtained a quadratic fit to Hindman's corrected results:

$$\mu_p'(T) - \mu_p'(0) = -11.88(9)T + 0.020(9)T^2 + 0.2(15) \quad (23)$$

where T is in °C and the correction is in ppb. (The uncertainties are based only on the fit and are not meant to indicate an estimate of possible systematic errors.) As a comparison Schneider et al (SCH58) report a linear coefficient of -9.5 ppb/°C for a cylindrical sample in the range 25°C < T < 110°C. This may be compared with Hindman's uncorrected data which yield an average slope of -10.0 ppb/°C over this range.

V.3 Derived Results

From our value of $g_j(H)/g_p'$ we can calculate the proton moment in Bohr magnetons according to

$$\frac{\mu_p'}{\mu_B} = \frac{g_p'}{g_j(H)} \cdot \frac{g_j(H)}{g_e} \cdot \frac{g_e}{2} \quad (24)$$

Using the theoretical value calculated by Grotch and Hegstrom (GRO71):

$$g_j(H)/g_e = 1 - 1.7705 \times 10^{-5} \quad (25)$$

and the accepted value (COH73) for the electron g factor anomaly based on measurements by Wesley and Rich (WES71):

$$g_e/2 = 1.001\ 159\ 6567\ (35) \quad , \quad (26)$$

we obtain

$$\mu_p'/\mu_B = 0.001\ 520\ 992\ 983\ (17)\ (11\text{ppb}) \quad . \quad (27)$$

The shielding constant for water is determined according to

$$\sigma(\text{H}_2\text{O}) = 1 - \frac{g_p'}{g_j(\text{H})} \cdot \frac{g_j(\text{H})}{g_p(\text{H})} \cdot \frac{g_p(\text{H})}{g_p} \quad . \quad (28)$$

We use the theoretical value (GRO71)

$$g_p(\text{H})/g_p = 1 - 1.7733 \times 10^{-5} \quad (29)$$

and the experimental value (WIN72)

$$g_j(\text{H})/g_p(\text{H}) = 658.210\ 706\ (6) \quad (30)$$

to obtain

$$\sigma(\text{H}_2\text{O}) = 25.790\ (14) \times 10^{-6} \quad (31)$$

for a spherical sample of water at 34.7°C.

We have mentioned in Sec. IV many involved corrections which were necessary to achieve a final uncertainty of 10 ppb.

Most of these corrections arose because of the constraint imposed by the need to use each bulb as a maser storage bulb as well as an NMR sample holder, in particular, the need for a large neck and a collimator. An NMR sample holder for measuring a field to 10 ppb can be much simpler. A thin wall spherical sample holder with capillary neck, for instance, eliminates the majority of corrections. The temperature correction should not be neglected, but by operating near 34.7°C , the uncertainty introduced is small.

APPENDIX

A. Verification of NMR Frequency Determination

In an attempt to check the validity of the symmetrization procedure described in Sec. IV.3, we reanalyzed much of the data using different intervals for symmetrization. To test the effect of a different choice of interval, we reanalyzed data from two runs on different nights for each of the 4 bulb configurations using an interval of 20 points starting 30 points from the center. The mean change for given runs was 31 ppb with a standard deviation of 36 ppb. While the difference is not statistically significant, neither are the statistics good enough to confirm the earlier analysis. Several other methods of analysis, such as fitting to a lorentzian and determining the zero crossing frequency of the decay signal, failed to properly analyze computer models of the signals.

The method which we settled upon for checking the symmetrization analysis is based upon the following idea: It is easy to show that if the centroid of a lorentzian line with a small dispersive component is determined by integrating over a region large compared to the linewidth and symmetric about the line center, the centroid is a linear function of the length of the integration region and of the percent dispersion. In the absence of dispersion the centroid always gives the true line center and in the presence of dispersion the centroid

extrapolates to the true center with decreasing integration interval. Computer analysis confirmed that this is also true for asymmetric distributions of lorentzians as long as the integration interval is at least as large as the asymmetric linewidth. Errors involved are about 1 ppb for realistic asymmetries.

We applied this technique to our data by first using the symmetrization routine to obtain an approximately absorptive line and then calculating the centroid for symmetric integration intervals from 2 to 24 Hz about each side of the line center. The intervals for initial symmetrization differed from those used previously, so different mixtures of absorption and dispersion generally resulted. The computed centroid was plotted against the integration length. An example is given in Fig. A1. The plot is linear for intervals of 4 to 13 Hz. The low limit indicates the extent of line asymmetry and the upper limit is due to noise or bandpass effects. The majority of cases showed linearity to within 4 Hz of the center.

The runs chosen for this analysis were the same ones used in the second symmetrization analysis. The standard deviation of successive NMR frequency determinations was typically 7 ppb. The mean difference between the extrapolation results and the first symmetrization results was 2(3) ppb. As with the first analysis, there was no significant discrepancy between results for positive and negative beat frequencies. Because of the

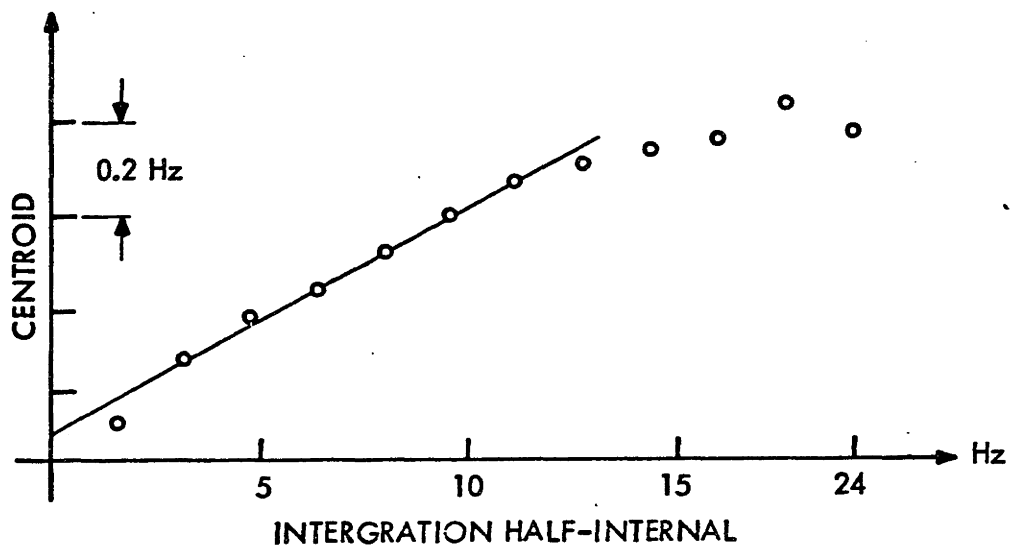


FIG. A1 CENTROID EXTRAPOLATION

good agreement between the two methods, we feel that adoption of the symmetrization analysis is justified.

B. Details of Correction Calculations

Shape: Corrections for non-sphericity of the water sample are due to the meniscus. The location of the meniscus surface for each NMR bulb is determined as described in the text. The best fit of this surface to a spherical surface is determined by eye from the bulb photographs. We assume cylindrical symmetry about the vertical axis. The resulting parameters are the radius of the sphere and the separation between the meniscus sphere center and the bulb sphere center. These parameters are used in the program MULPOL to calculate the dipole, quadrupole and octopole moments of the meniscus region. It is convenient to choose the origin for calculation of the multipole moments to be the center of the meniscus sphere. MULPOL uses a magnetic surface charge formalism to calculate the moments by integrating over the two spherical surfaces bounding the meniscus region. The moments of interest are

$$\text{dipole: } P_x = \int_S d^2\vec{r} \sigma(\vec{r}) \cdot x$$

$$\text{quadrupole: } Q = \int_S d^2\vec{r} \sigma(\vec{r}) 3xz$$

$$\text{octopole: } C_1 = \int_S d^2\vec{r} \sigma(\vec{r}) 3x(5z^2 - r^2)$$

where in each case the integration is over the surfaces bounding the meniscus region. $\sigma(\vec{r})$ is the surface magnetic charge density, and the external field is in the x direction. The z

axis is the symmetry axis,

The fields produced by these moments are averaged over the volume of the bulb according to

$$H_{x(\text{dip})} = P_x \frac{1}{V} \int d^3\vec{r} \frac{1}{r^3} (3(\hat{r} \cdot \hat{x})^2 - 1)$$

$$= P_x \frac{\pi}{V} \int_{u_{\min}}^1 du (1 - 3u^2) \ln \frac{r_{\max}}{r_{\min}}$$

$$H_{x(\text{quad})} = Q \cdot \frac{1}{V} \int d^3\vec{r} \frac{z}{r^7} (5x^2 - r^2)$$

$$= Q \frac{\pi}{V} \int_{u_{\min}}^1 du (3u - 3u^3) \left(\frac{1}{r_{\min}} - \frac{1}{r_{\max}} \right)$$

$$H_{x(\text{oct})} = \frac{C_1}{8} \frac{1}{V} \int \frac{d^3\vec{r}}{r^9} (x^2 (3r^2 - 7x^2) + (y^2 - 4z^2) (r^2 - 7x^2))$$

$$= \frac{C_1 \pi}{8V} \int_{u_{\min}}^1 du (30u^2 - 35u^4 - 3) \left(\frac{1}{2r_{\min}^2} - \frac{1}{2r_{\max}^2} \right)$$

In each case the volume integral extends over the bulb, exclusive of the meniscus region. Using the meniscus sphere center as the origin for spherical coordinates, we have done the radial and azimuthal integrations. The remaining integration is done by the programs DIPAV, QUADAV and OCTAV. DIPAV calculates P_x , while the results of the other programs must be multiplied by the MULPOL moments. In the calculations the bulb sphere is assumed to have a 1 cm radius and cgs units are used throughout (all quantities in the text are expressed in

S.I. units). The external field is set to unity, so the multipole contributions are in relative units. The term "RAT" which appears in the programs is the ratio of meniscus to total volume, and is used to determine the bulb volume.

Gradients: Corrections for the difference in field between the meniscus and bulb regions arise from the field gradients caused by the diamagnetism of the bulb assembly. If the bulb were simply a uniform spherical shell there would be a uniform field inside. From the bulb photographs and the known dimensions of the collimator and holder, the deviations from this condition are determined. Since we have a cylindrical symmetry the material missing from the spherical shell or in excess of the spherical shell is approximated by a set of rings with height, inner, and outer radii which represent the geometry of the material. A negative or positive susceptibility is assigned depending on whether the ring represents presence or absence of material. For the stems and collimators, this is a good approximation. For such elements as the missing parts of the spherical shell it is less so, but these contribute little to the effect.

The program NECK calculates the field due to the diamagnetic rings averaged over the meniscus volume. By choosing the parameters properly, any of the stems, collimator, etc. can be included. Choosing the meniscus dimensions equal to the entire bulb allows the field over the bulb to be calculated. The correction is determined from the difference between the field

in the meniscus and in the total volume along with the ratio of meniscus to bulb volume.

C. Computer Programs

SAF2 is one version of the program used for taking data. It differs from other versions in details such as ability to interrupt data taking and the formatting of output files. Switch settings tested by the ISWTST routine are used to interact with the program while running.

Several subprograms are called by SAF2. SIGAV averages and plots data and stores it on the disc. SIGSET is called from SIGAV and is the machine language routine which reads data into memory from the input register. Also called by SAF2 are OUTI which writes the data onto tape and TEXTO which allows comments to be written onto a file after data taking.

DELAY8 fourier transforms the NMR data taken by SAF2 after discarding the first 32 points. Variations on this program have incorporated different delays, different data input/output format and baseline filling at the end of signals where insufficient points were taken to leave 4096 after the 32 point delay. Only 256 complex points in the region of the resonance are outputted. FFT is called by DELAY8 and performs the actual fourier transforming.

FIX2 transforms the maser signal. Since the data is stored as integers in 16 bit words, there is occasional overflow of the maximum allowable integer. FIX2 corrects for this by subtracting the baseline from each point.

MASAN fits the maser transformed signal to an absorption

- dispersion lorentzian with periodic repetitions. The subroutine LORFIT does the actual fitting. LORFIT calls SIMQ, an IBM scientific subroutine for solving simultaneous equations which we do not show here. Also called are COMPL, a plotting routine, EFREQ, which calculates the field coupled part of the maser frequency from the fit to the beat frequency, and STOUT and SHOUT which output results.

CENTR calculates the centroid of NMR signal transforms after forming an absorptive spectrum from the complex transform spectrum.

The remaining programs listed here have been discussed in appendix B.

Programs: SAF2

SIGAV

SIGSET

OUTI

TEXTO

BELL

DELAY8

FFT

CODE

FIX2

MASAN

LORFIT

COMPL

EFREQ

STOUT

SHOUT

CENTR

MULPOL

DIPAV

QUADAV

OCTAV

NECK

SAF2, p. 1

```

DIMENSION IDATA(4300)
LOGICAL ISWTST
COMMON ISKQ
INUM1=0
INUM3=0
WRITE (6,101)
C POINTS PER AVERAGE
101 FORMAT (' MNX=' )
READ (6,201) MNX
201 FORMAT (I4)
WRITE (6,102)
C BURSTS PER AVERAGE
102 FORMAT (' MBURST=' )
READ (6,201) MBURST
WRITE (6,103)
C AVERAGES PER SIDEBAND
103 FORMAT (' MPOINT=' )
READ (6,201) MPOINT
WRITE (6,301)
301 FORMAT (' NNX=' )
READ (6,201) NNX
WRITE (6,350)
350 FORMAT (' # OF PTS TO SKIP = ' )
READ (6,201) ISKQ
WRITE (6,302)
302 FORMAT (' NBURST=' )
READ (6,201) NBURST
WRITE (6,303)
303 FORMAT (' NPOINT=' )
READ (6,201) NPOINT
WRITE (6,202)
202 FORMAT (' ICHANG=' )
READ (6,201) ICHANG
ISTQ=0
WRITE (6,203)
203 FORMAT (' ASSIGN'// 1 MASER DISK'// 2 MASER DT'//
1' 3 NMR DISK'// 4 NMR DT'// 5 TEXT DT')
PAUSE 1
NPOINT=NPOINT*2
MPOINT=MPOINT*2
NRUN=NPOINT*ICHANG
MRUN=MPOINT*ICHANG
NNX4=NNX+4
MNX4=MNX+4
DEFINE FILE 1(MPOINT,MNX4,U,IVAR1)
DEFINE FILE 3(NPOINT,NNX4,U,IVAR3)
79 ISTQ=ISTQ+1
KQ=1
ISCALE=64
ISKTEM=ISKQ

```

SAF2, p. 2

```

ISKQ=0
CALL SIGAV(KQ,MNX, IDATA, ISCALE, MBURST, MPOINT)
CALL BELL
WRITE (6,401) ISTQ
401  FORMAT (' MASER FINISHED CHANGE BULBS'// ' DATA SET #',I4)
CALL OUTI(IDATA,MNX,KQ, INUM1, MPOINT)
CALL BELL
WRITE (6,402)
402  FORMAT (' DT IS WRITTEN')
PAUSE 2
ISKQ=ISKTEM
IF (.NOT. ISWTST(1)) GO TO 597
WRITE (6,593)
593  FORMAT (' # TO SKIP (I2)')
READ (6,594) ISKQ
594  FORMAT (I2)
597  KQ=3
      ISCALE=1
CALL SIGAV(KQ,MNX, IDATA, ISCALE, NBURST, NPOINT)
CALL BELL
WRITE (6,403) ISTQ
403  FORMAT (' NMR FINISHED, CHANGE BULBS'// ' DATA SET #',I4)
CALL OUTI (IDATA,MNX,KQ, INUM3, NPOINT)
CALL BELL
WRITE (6,402)
IF (ISTQ.EQ. ICHANG) GO TO 501
PAUSE 3
GO TO 79
501  WRITE (6,500)
500  FORMAT (' WRITE TEXT, SIGNAL END WITH SW #4')
CALL TEXTQ
END FILE 1
END FILE 3
STOP
END

C
SUBROUTINE OUTI (IDATA,MNX,KQ, INUM1, MPOINT)
DIMENSION IDATA(MNX)
DO 10 I=1, MPOINT
INUM1=INUM1+1
READ (KQ,I) IDATA, IBURST, IFLAG, ITIM1, ITIM2
KQ1=KQ+1
WRITE (KQ1) IDATA, IBURST, IFLAG, ITIM1, ITIM2
10  CONTINUE
RETURN
END

```

SAF2, p. 3

```

SUBROUTINE SIGAV(KQ, NNX, IDATA, ISCALE, NBUKST, NPOINT)
COMMON ISKQ
C AVERAGES MASER OR NMR DATA
C USE WITH ASSEMBLER PROG SIGSET
C ISKQ= # OF PTS SKIPPED
DIMENSION IDATA(NNX)
LOGICAL ISWTST
INUM=1
NP2=NPOINT/2
92 CONTINUE
INDX=0
IERR=0
IFLAG=0
IBURST=0
NNX2=NNX*2
137 DO 37 I=1, NNX
37 IDATA(I)=0
CALL SIGSET (IDATA, IERR, IBURST, INDX, NBUKST, NNX2, ISKQ)
IBURST=0
1 CONTINUE
WRITE (6, 700)
700 FORMAT (' STEP 1')
IF (ISWTST(0)) GO TO 20
WRITE (6, 701)
701 FORMAT (' STEP 2')
IF (NBUKST.GT. IBURST) GO TO 1
GO TO 11
703 WRITE (6, 704)
704 FORMAT (' STEP 3')
20 IBURST=NBUKST
CALL BELL
PAUSE 4
IFLAG=0
IERR=0
GO TO 137
11 CALL NSTORE
CALL STORE
TEMP=0
IF (KQ.NE. 1) GO TO 55
DO 394 I=0, NNX
394 TEMP=TEMP+IDATA(I)
TEMP=TEMP/(NNX-7)
IAY=TEMP
55 DO 9 I=1, NNX
IF (KQ.NE. 1) GO TO 56
INDATA=(IDATA(I)-IAY)/16
GO TO 57
56 INDATA=IDATA(I)/NBUKST
57 IX=ISCALE*1-2048
93 CALL PENNY (IX, INDATA)

```

SAF2, p. 4

```

CALL PENDN
9  CALL PENUP
10 IF (IERR.EQ.1) IFLAG = 1
    CALL TIME (ITIM1,ITIM2)
    IF (.NOT.ISWTST(0)) GO TO 13
    CALL BELL
    PAUSE 5
    IERR=0
    IFLAG=0
    GO TO 137
13  WRITE (6,INUM) IDATA, IBURST, IFLAG, ITIM1, ITIM2
    IF (INUM.EQ.NPOINT) GO TO 90
    IERR=0
    IFLAG =0
    IF (INUM.EQ.NP2) GO TO 91
    INUM=INUM+1
    GO TO 137
91  CALL BELL
    INUM=INUM+1
    WRITE (6,200)
200 FORMAT (' CHANGE SIDEBANDS')
    PAUSE 6
    GO TO 92
90  CONTINUE
    RETURN
    END

C
    SUBROUTINE TEXT0
    DIMENSION IOUT(36)
    LOGICAL ISWTST
10  READ (6,102) IOUT
101  FORMAT (1X,36A2)
    WRITE (5,101) IOUT
102  FORMAT (36A2)
    IF (ISWTST(3)) GO TO 11
    GO TO 10
11  RETURN
    END

C
    SUBROUTINE BELL
101  WRITE (6,101)
    FORMAT (' ')
    RETURN
    END

```

SAF2, p. 5

```

        .TITLE SIGSET
; CALL SIGSET(IDATA, IERR, IBURST, INDX, NBURST, NNX2, ISKQ)
; AVERAGES NBURST DATA SWEEPS
; SKIPS ISKQ PTS
        .GLOBL SIGSET
        .ASECT
        .=130
        .WORD ISRAD
        .WORD 340
        .=404
        .WORD ISRIR
        .WORD 240
        .CSECT
        R5=25
NUMB:   .WORD 0
ISKQ:   .WORD 0
SKIPO:  .WORD 0
BSTOP:  .WORD 0
ERR:    .WORD 0
SAVE:   .WORD 0
SAVE1:  .WORD 0
INDX:   .WORD 0
TMP:    .WORD 0
GARB:   .WORD 0
SIGSET: MOV 2(R5),SAVE ;SAVE ADD 00 ARRAY
        MOV 4(R5),ERR ;SAVE ADD OF ERROR FLAG
        MOV 6(R5),SAVE1 ;SAVE ADD OF IBURST
        MOV 10(R5),INDX
        MOV 12(R5),BSTOP
        MOV 14(R5),NUMB
        MOV 16(R5),ISKQ
        MOVB #26, @#165340 ;ALLOW LAM TO BE SET
        CLR @#176770
        BIS #100, @#164010 ;INTERUPT ENABLE
        RTS R5
ISRAD:  CMP @NUMB, @INDX ;INDEX TOO LARGE?
        BEQ OUT ;YES
        CMP #0, SKIPO
        BEQ CONT1
        INC SKIPO
        MOV @#176772, GARB
        BR GO
CONT1:  MOV SAVE, TMP
        SUB @ISKQ, SKIPO
        ADD @INDX, TMP
        ADD @#176772, @TMP
        SUB #4000, @TMP
CONT:   ADD #2, @INDX ;INDEX=INDEX +2
        BIT #40000, @#176770 ;TEST FOR SERV ERROR
        BNE ERROR

```

SAF2, p. 6

```
      BIT #40, @#176770      ; TEST FOR RECEIPT ERROR
      BNE ERROR
      BR GO
ERROR:  MOV #1, @ERR
GO:    BIS #100, @#176770    ; TURN ON INT ENAB
OUT:   RTI
ISRIR:  MOVB #10, @#165340   ; CLEAR LAM
      CLR @INDX             ; RESET INDEX
      CLR SKIPO
NXT:   CMP @BSTOP, @SAVE1
      BNE NORM
      CLR @#176770
      CLR @#164010
      BR OUT1
NORM:  INC @SAVE1
      CLR @#176770         ; INITIALIZE
      MOV #102, @#176770
OUT1:  RTI
      .END
```

DELAY8

```

C      DELAY8
      DIMENSION X(4204),IDATA(4204),Y(256)
      COMPLEX X,Y
      EQUIVALENCE (IDATA(1),X(3072))
      EQUIVALENCE(X(832),Y(1))
      WRITE (6,100)
100    FORMAT (' DELAY8 TAKES FT OF 30 REC 4200 PTS EA')
      WRITE (6,101)
101    FORMAT (' AFTER 32 PT DELAY AND OTPTS 30 REC 256 PTS EA')
      WRITE(6,102)
102    FORMAT(' INPUT IS LINKED, OTPT IS CONTIG:AS BEFOR RUN TO 1,2')
      N=30
      DEFINE FILE 2(N,1024,U,IVAR)
      IDSKP=32
      IDSRT=IDSKP+1
      IDSTP=IDSKP+4096
905    DO 10 I=1,N
      READ(1) IDATA
      DO 12 J=IDSRT, IDSTP
      JJ=J-IDSKP
      X(JJ)=IDATA(J)
12     CONTINUE
      IGAMMA=12
      SIGN=1
      CALL FFT(IGAMMA,X,SIGN)
      WRITE(2,'I) Y
      WRITE(6,105) I
105    FORMAT(' COMPLETED FT #',I2)
10     CONTINUE
      END FILE 2
      STOP
      END

```


FIX2

```
DIMENSION INPO(71), IDATA(64), X(64)
COMPLEX X
EQUIVALENCE (INPO(3), IDATA(1))
IGAMMA=6
N=64
SIGN=1
CALL SETERR(3, -1)
WRITE (6, 100)
100  FORMAT (' ASSIGN I/O TO 1/2 BEFORE RUNNING')
DEFINE FILE 2(50, 256, U, IVAR1)
DO 10 I=1, 50
READ (1) INPO
DO 11 J=1, 64
X(J)=IDATA(J)-IDATA(64)
11  CONTINUE
CALL FFT (IGAMMA, X, SIGN)
WRITE (2, 1) X
WRITE (6, 800) I
800  FORMAT (' FT # ', I4)
10  CONTINUE
END FILE 2
END
```

MASAN, p. 1

```

C      MASAN - ANALYSIS OF MASER TRANSFORMS
C
C      NEEDS CONTIGUOUS INPUT FILE
C      DESIGNED TO RUN UNDER BATCH
C      CAMAC (CONSOLE) SWITCH CONTROL
C
C      1 (0) - UP ALLOWS RECORD # INPUT
C      2 (1) - UP ALLOWS PLOTTING
C      3 (4) - UP INHIBITS SIDEBAND STATS
C      4 (3) - UP KILLS PRESENT RECORD
C
C
C      DIMENSION X(64),XY(64),VX(50),XINIT(2,6)
C      COMMON IFLAG,ICHFL
C      LOGICAL ISWTST
C      COMPLEX XY
C      DOUBLE PRECISION VX
C      N=2
C      DEFINE FILE 1(50,256,U,IVAR)
C      JPOINT=1
510    IF (.NOT. ISWTST(0)) GO TO 511
C      WRITE (6,200)
200    FORMAT (' REC # (I2)')
C      READ (6,201) JPOINT
201    FORMAT (I2)
511    IF (ISWTST(2)) INEW=1
C      READ (1,JPOINT) XY
C      YMAX=0
C      DO 10 I=1,64
C      Y=CABS(XY(I))
C      X(I)=REAL(XY(I))
C      IF (I.EQ.1) GO TO 10
C      IF (I.GT.31) GO TO 10
C      IF (YMAX.GT.Y) GO TO 10
C      YMAX=Y
C      IMAX=I
10    CONTINUE
C      ISETW=(JPOINT-1)/5
C      ISDBD=(3-(-1)**ISETW)/2
C      IF (INEW.EQ.1) GO TO 100
C      IF (XINIT(ISDBD,1)) 512,100,512
100    IFLAG=0
C      ICHFL=-1
C      RIN=-(YMAX)
C      PHI=ATAN(X(IMAX)/SQRT(YMAX**2-X(IMAX)**2))
C      CIN=3.0
C      X0IN=IMAX
C      EIN=0.0
C      GO TO 39
512    RIN=XINIT(ISDBD,2)

```

```

SUBROUTINE FFT (IGAMMA, X, SIGN)
  DIMENSION X(4096)
  COMPLEX A, X
  N=2**IGAMMA
  ARG=2. *3. 14159265358979/N
  M2=0
  DO 51 K=1, IGAMMA
    IGK=N/2**K
    M2=(2**K)-1
    IP=2**(K-1)
    LA=-IP
    DO 52 I=1, IGK
      LA=LA + IP
      B1=COS(ARG*LA)
      B2=SIN(ARG*LA)
      A=CMPLX(B1, B2*SIGN)
      MX = -IGK*2
    DO 53 M=M2, 2, 2
      MX=MX+(IGK*2)
      IPMX= I+MX
      IPMM=IPMX + IGK
      X(IPMX)=X(IPMX)+X(IPMM)
      X(IPMM)=A*(X(IPMX)-2*X(IPMM))
53 CONTINUE
52 CONTINUE
51 CONTINUE
  CALL CODE (IGAMMA, X)
  RETURN
  END
  SUBROUTINE CODE (IGAMMA, X)
  DIMENSION INDXR(12), X(4096)
  COMPLEX X, DUM
  N=2**IGAMMA
  DO 66 I=1, IGAMMA
66 INDXR(I)=0
    N1=N-1
    DO 60 J=2, N1
      L=1
      DO 65 I=1, IGAMMA
        IF (INDXR(I)) 65, 62, 65
62 INDXR(I)=1
        GO TO 63
65 INDXR(I)=0
63 DO 64 I=1, IGAMMA
64 L=L+INDXR(I)*2**(IGAMMA-I)
        IF (L-J) 60, 60, 67
67 DUM=X(J)
        X(J)=X(L)
        X(L)=DUM
60 CONTINUE
  RETURN
  END

```

MASAN, p. 2

```

PHI=XINIT(ISDBD,3)
CIN=XINIT(ISDBD,4)
XOIN=XINIT(ISDBD,5)
EIN=XINIT(ISDBD,6)
JCHFL=0
39 M=64
CALL LORFIT(AIN,PHI,XOIN,CIN,EIN,X,M,N,JPOINT)
IF (JCHFL.EQ.1) GO TO 100
IF (IFLAG.EQ.1) GO TO 513
XINIT(ISDBD,1)=1.
XINIT(ISDBD,2)=AIN
XINIT(ISDBD,3)=PHI
XINIT(ISDBD,4)=CIN
XINIT(ISDBD,5)=XOIN
XINIT(ISDBD,6)=EIN
513 CONTINUE
CINT=CIN*125./(8.0*0.1202)
XOINT=XOIN*125./(8.0*0.1202)
PHIT=PHI*180./3.14
WRITE (2,850) XOINT,PHIT,CINT,AIN,EIN,M
850 FORMAT (5E15.7,I2)
CALL EFREQ(ISDBD,XOINT,VX,JPOINT)
JPOINT=JPOINT+1
IF (JPOINT.LE.50) GO TO 510
IF (ISWTST(3)) GO TO 514
CALL STOUT (VX)
GO TO 515
514 CALL SHOUT(VX)
515 CONTINUE
WRITE (5,573)
573 FORMAT(1X,///)
END FILE 1
STOP
END
SUBROUTINE COMPL(X,FLINE,YMAX,MDAT)
DIMENSION X(64),A(4),FLINE(64)
LOGICAL ISWTST
IF (.NOT.ISWTST(1)) GO TO 20
CALL SERASE
CALL SSCALE (10.,10.,0.,0.)
ENCODE (8,298,A)MDAT
398 FORMAT ('DATA #',I2)
CALL SWRITE(A,8,0.1,0.9)
Y2M=2.03*YMAX
YMAXM=-1.015*YMAX
CALL SSCALE(33.,Y2M,0.0,YMAXM)
J0=-1
DO 10 I=2,32
XPT=I
YPT=FLINE(I)

```

MASAN, p. 3

```

      IF (YPT. GT. YMAX) YPT=YMAX
      IF (YPT. LT. YMAXM) YPT=YMAXM
      CALL SPLOT(J0, XPT, YPT)
      J0=1
10    CONTINUE
      DO 20 I=2, 32
      XPT=I
      PPT=X(I)
      CALL SPOINT(1, XPT, PPT, 0.1)
20    CONTINUE
      RETURN
      END
      SUBROUTINE LORFIT(AIN, PHI, X0IN, CIN, EIN, Y, M, N, MDATE)
C     LORFIT -- A PROGRAM TO FIT THE BEST LORENTZIAN TO A SET OF DATA
C     BY LEAST SQUARES
C
C     THIS PROGRAM RETURNS FITTED VALUES OF PARAMETERS
C     INTO THE INPUT PARAMETERS AND THE NUMBER OF ITERATIONS
C     INTO THE INPUT NUMBER OF POINTS
      DIMENSION Y(M), FLINE(64)
      DIMENSION A(5, 5), B(5)
      COMMON IFLAG, ICHFL
      LOGICAL ISWTST
      YMAX=ABS(AIN)
      SDELX=.005
      ITERM=15
      CONVX=.005
100  CONTINUE
101  I1=0
102  I2=I1+1
103  I0=I1+1
      A1=AIN*SIN(PHI)
      A2=-AIN*COS(PHI)
      C=CIN
      X0=X0IN
      E=EIN
      I3=0
      L1=I0
C     BEGIN LOOP TO CALCULATE ITERATED VALUES OF PARAMETERS
      JDIYX=-6
      ITER=1
200  CONTINUE
C     SET MATRICES EQUAL TO ZERO
      DO 210 K=1, 5
      DO 211 J=1, 5
      A(K, J)=0.0
211  CONTINUE
      B(K)=0.0
210  CONTINUE
C     DEFINE VARIABLES AND FORM SUMS

```

MASAN, p. 4

```

SUMSQ=0.0
A(5,5)=M-1
DO 300 K=2,M
  DLX0=0.0
  DLC=0.0
  DLA1=0.0
  DLA2=0.0
  GLINE=0.0
  J=-N-1
311  J=J+1
     DIFA=(K-1-X0-J*M)/C
     DIFB=(X0+K-1-M-J*M)/C
C   EXTRA M (PERIODICITY) IN DIFB BECAUSE FFT GOES FROM 0 TO M
C   NOT FROM -M/2 TO +M/2
     DENA=1.0/(1.0+DIFA**2)
     DENB=1.0/(1.0+DIFB**2)
     D1A=DIFA*DENA
     D1B=DIFB*DENB
     D2A=2.*D1A**2
     D2B=2.*D1B**2
     D12A=2.*DENA*D1A
     D12B=2.*DENB*D1B
     GLINE=GLINE+A1*DENA+A2*D1A+A1*DENB-A2*D1B
  DLA1=DENA +DENB +DLA1
  DLA2=DLA2+D1A-D1B
  DLC=DLC+(A1*(D2A+D2B)+A2*(DIFA*D2A-DIFB*D2B-D1A+D1B))/C
  DLX0=DLX0+(A1*(D12A-D12B)+A2*(D2A-DENA+D2B-DENB))/C
310  IF(J.LT.N) GO TO 311
     GLINE=GLINE+E
     H=Y(K)-GLINE
     FLINE(K)=GLINE
  A(1,1)=A(1,1)+DLA1**2
  A(1,2)=A(1,2)+DLA1*DLA2
  A(1,3)=A(1,3)+DLA1*DLC
  A(1,4)=A(1,4)+DLA1*DLX0
  A(1,5)=A(1,5)+DLA1
  A(2,2)=A(2,2)+DLA2**2
  A(2,3)=A(2,3)+DLA2*DLC
  A(2,4)=A(2,4)+DLA2*DLX0
  A(2,5)=A(2,5)+DLA2
  A(3,3)=A(3,3)+DLC**2
  A(3,4)=A(3,4)+DLC*DLX0
  A(3,5)=A(3,5)+DLC
  A(4,4)=A(4,4)+DLX0**2
  A(4,5)=A(4,5)+DLX0
  B(1)=B(1)+H*DLA1
  B(2)=B(2)+H*DLA2
  B(3)=B(3)+H*DLC
  B(4)=B(4)+H*DLX0
  B(5)=B(5)+H

```

MASAN, p. 5

```

SUMSQ=SUMSQ+H**2
300 CONTINUE
    CALL COMPL(Y,FLINE,YMAX,MDAT)
C   INTERRUPT CALC. OF MATRICES TO WRITE ST. DEV. AND TEST CONVERG.
SIG=SQRT(SUMSQ/(M-2))
IT=ITER-1
IF(IT) 350,350,360
350 WRITE(6,351) SIG
351 FORMAT(//      SIG. OF INITIAL PARAMETERS = ', E15.7)
GO TO 370
360 DELSIG=SIG-OLDSIG
ABSIG=ABS(DELSIG)/SIG
WRITE(6,361) SIG, DELSIG
361 FORMAT(1X,' SIG. = ',E15.7,4X,' DELSIG = ',E15.7/)
IF(DELSIG) 363,362,362
362 JDIVX=JDIVX+1
IF(JDIVX.LT.0.OR.ABSIG.LT.0.01) GO TO 363
366   WRITE (2,367) MDAT
367   FORMAT(I4,' NON CONVERG')
    X0IN=0
    IFLAG=1
    RETURN
363 CONTINUE
    IF(SUMDEL.LT.SDELX.AND.ABSIG.LT.CONVX) GO TO 371
372 IF(ITER-ITERM) 370,370,366
370   IF (ISWTST(4)) GO TO 366
C   FORM SYMMETRIC OTHER HALF OF COEFFICIENT MATRIX
DO 250 K=2,5
  KK=K-1
  DO 251 J=1,KK
    A(K,J)=A(J,K)
251 CONTINUE
250 CONTINUE
475 CONTINUE
C   SOLVE SYSTEM OF EQUATIONS FOR INCREMENTAL PARAMETERS
NEQ=5
CALL SIMQ(A,B,NEQ,KS)
C   CONSTANT VECTOR B(K) HAS BEEN REPLACED BY INCREMENTS
C   FORM NEW PARAMETERS
A1=A1+B(1)
A2=A2+B(2)
FSC=1.
IF (ITER.EQ.1) FSC=0.1
C=C+FSC*B(3)
X0=X0+FSC*B(4)
E=E+B(5)
SUMDEL=ABS(B(4)/X0)
IF (ICHFL.EQ.-1) GO TO 901
IF(SUMDEL.GT.0.20) GO TO 900
901   IF ((X0.LT.0).OR.(X0.GT.32)) GO TO 366

```

MASAN, p. 6

```

C      WRITE NEW PARAMETERS AND INCREMENTS FOR ITERATION
      X1Q=X0*125./(.0+0.1202)
      WRITE(6,403) X1Q
403    FORMAT(' CENTROID =',F10.3)
      OLDSIG=SIG
      ITER=ITER+1
      GO TO 200
900    ICHFL=1
      RETURN
371   CONTINUE
      M=ITER
      PHI=-ATAN(A1/A2)
      CIN=C
      EIN=E
      SIP=SIN(PHI)
      ISP=1
      IF (SIP.LT.0) ISP=-1
      AIN=ISP*A1*SQRT(1.0+(A2/A1)**2)
      X0IN=X0
      WRITE (2,783) MDAT,SIG
783   FORMAT(I4,E15.7)
      RETURN
END
      SUBROUTINE EFREQ(ISDBD,XIN,VX,I)
      DIMENSION VX(50)
      DOUBLE PRECISION VX,TEMP,TEMP1,DEL2,X,DIF
      VX(I)=0
      IF (XIN) 10,20,10
10     DEL2=1.42640575176809
      X=(1.00+1.00/6.5821070602)/DEL2
      DEL2=DEL2/2.00
      IF (ISDBD.EQ.2) GO TO 16
15     VX(I)=2.998007+XIN
      GO TO 17
16     VX(I)=2.999207-XIN
17     TEMP=3.207-VX(I)
      TEMP=9.209+TEMP
      VX(I)=TEMP+6.5939414908
C      WRITE (6,300) ISDBD,TEMP
300   FORMAT(I4,14,5X,D17.10)
11     TEMP1=VX(I)
      DIF=1.00/(X*VX(I))**2
      DIF=DSQRT(1.00+DIF)
      DIF=X*VX(I)*(1.00-DIF)
      VX(I)=TEMP+DEL2*(1.00+DIF)
      DIF=DABS(VX(I)-TEMP1)
      IF(DIF.GT.1.) GO TO 11
20     CONTINUE
      RETURN
      END

```



```

SUBROUTINE STOUT(VX)
DIMENSION VX(50)
DOUBLE PRECISION VX, SAVM
WRITE (5,100)
100 FORMAT (' MASER ANALYSIS UNDER PROGRAM "MASAN"',/,
1'REC#', 6X, 'FREQUENCY', 11X, 'SIDEBAND MEAN', 8X, 'S. D. ')
DO 10 I1=0, 45.5
WRITE (5,101)
101 FORMAT (' ')
EMN=0
STD=0
ICT=0
DO 11 I2=1, 5
K=I1+I2
IF (VX(K).EQ.0) GO TO 11
CODE=VX(K)-9.861403990D9
EMN=EMN+CODE
STD=STD+CODE**2
ICT=ICT+1
11 CONTINUE
DO 12 I2=1, 5
K=I1+I2
IF (I2.EQ.3) GO TO 20
IF (VX(K).EQ.0) GO TO 30
21 WRITE (5,102) K, VX(K)
102 FORMAT(2X, I2, 4X, D17.10)
GO TO 12
20 IF (ICT.LE.1) GO TO 21
STD=SQRT((STD-(EMN**2)/ICT)/(ICT-1))
SAVM=9.861403990D9+(EMN/ICT)
IF (VX(K).EQ.0) GO TO 25
WRITE (5,103) K, VX(K), SAVM, STD
103 FORMAT(2X, I2, 4X, D17.10, 6X, D17.10, 6X, F5.0)
GO TO 12
25 WRITE (5,104) K, SAVM, STD
104 FORMAT(2X, I2, 4X, 17(' '), 6X, D17.10, 6X, F5.0)
GO TO 12
30 WRITE (5,105) K
105 FORMAT (2X, I2, 4X, 17(' '))
12 CONTINUE
10 CONTINUE
RETURN
END
SUBROUTINE SHOUT(VX)
DIMENSION VX(50)
DOUBLE PRECISION VX
DO 10 I=1, 50
IF (VX(I).EQ.0) GO TO 10
WRITE (5,100) I, VX(I)
100 FORMAT (2X, I2, 5X, D17.10)
10 CONTINUE
END

```

CENTR, p. 1

```

C      CENTR
C
C      COMPUTES ABSORPTIVE PHASE BY SYMMETRIZING TAILS
C      AND COMPUTES CENTROID BY RECTANGULAR INTEGRATION
C      FROM OUTPUT OF DELAY8 OR DELAY9
C      DIMENSION Y(256), TABS(256), TABSO(256)
C      COMPLEX Y, TEMPO
C      LOGICAL ISWTST
C      TAB(PHI, Y)=COS(PHI)*AIMAG(Y)+SIN(PHI)*REAL(Y)
C      WRITE(6, 801)
801    FORMAT(' CAMAC SW#0 KILLS POINT, #1ENABLES PLOT')
C      WRITE(6, 100)
100    FORMAT(' TYPE IN M1, M2, M3 IN 3I2')
C      READ(6, 101) M1, M2, M3
101    FORMAT(3I2)
C      M1=NO. OF PTS AVERAGED FOR SYMMETRIZING
C      M2=CLOSEST DISTANCE FROM CENTER FOR SYM.
C      M3=HALF INTEGRATION RANGE FOR CENTROID
C      WRITE(5, 105)
105    FORMAT(' CENTROID VALUES UNDER PROGRAM 'CENTR' ')
C      WRITE(5, 106) M1, M2, M3
106    FORMAT(' M1, M2, M3 = ', 3(I3, 2X))
107    FORMAT(1H0)
C      WRITE(5, 107)
C      WRITE(5, 108)
108    FORMAT(' REC#      CENTROID      PHI')
C      WRITE(5, 107)
C      WRITE(6, 102)
102    FORMAT(' TYPE IN CENTER FREQ. F7. 0')
C      READ(6, 103) FCENI
103    FORMAT(F7. 0)
C      CENT=FCENI*(4096.*2.404E-04)+1.
C      CENT IS NOW IN UNITS OF RAW FT INDEX
C      CENT=CENT-831.
C      CENT IS NOW IN UNITS OF SHORTENED FT. INDEX
C      WRITE(6, 104)
104    FORMAT(' ASSIGN INPUT FILE TO DEVICE 1')
C      PAUSE
C      DEFINE FILE 1(30, 1024, U, IVAR)
C      DO 10 I=1, 30
C      READ(1, I) Y
C      TEMPO=0. 0
C      DO 300 II=1, 10
300    TEMPO=TEMPO+Y(II)
C      TEMPO=TEMPO/10.
C      DO 301 II=1, 256
301    Y(II)=Y(II)-TEMPO
C      ICOUNT=0
C      PHIOLD=0. 0
C      RETURN POINT FOR PHASE FIND LOOP

```

CENTR, p. 2

```

210 ICEN0=CENT
ICEN1=ICEN0+1
DIF=CENT-ICEN0
I AVL E0=ICEN0-M2
I AVL E1=ICEN1-M2
I AVL B0=I AVL E0-M1+1
I AVL B1=I AVL E1-M1+1
I AVR B0=ICEN0+M2
I AVR B1=ICEN1+M2
I AVR E0=I AVR B0+M1-1
I AVR E1=I AVR B1+M1-1
AVL RE0=0.0
AVL IM0=0.0
AVL RE1=0.0
AVL IM1=0.0
AVR RE0=0.0
AVR IM0=0.0
AVR RE1=0.0
AVR IM1=0.0
C COMPUTE RT & LFT AV FOR PHSE FINDING
DO 11 J=I AVL B0, I AVL E0
AVL RE0=AVL RE0+REAL(Y(J))
AVL IM0=AVL IM0+AIMAG(Y(J))
11 CONTINUE
DO 12 J=I AVL B1, I AVL E1
AVL RE1=AVL RE1+REAL(Y(J))
AVL IM1=AVL IM1+AIMAG(Y(J))
12 CONTINUE
DO 13 J=I AVR B0, I AVR E0
AVR RE0=AVR RE0+REAL(Y(J))
AVR IM0=AVR IM0+AIMAG(Y(J))
13 CONTINUE
DO 14 J=I AVR B1, I AVR E1
AVR RE1=AVR RE1+REAL(Y(J))
AVR IM1=AVR IM1+AIMAG(Y(J))
14 CONTINUE
C FORM WEIGHTED AVE TO ACCOUNT FOR NON-INTEG CENT
WAVL RE=AVL RE1*DIF+AVL RE0*(1.-DIF)
WAVL IM=AVL IM1*DIF+AVL IM0*(1.-DIF)
WAVR RE=AVR RE1*DIF+AVR RE0*(1.-DIF)
WAVR IM=AVR IM1*DIF+AVR IM0*(1.-DIF)
PHI=ATAN((WAVL IM-WAVR IM)/(WAVR RE-WAVL RE))
INTB0=ICEN0-M3
INTE0=ICEN0+M3
INTB1=ICEN1-M3
INTE1=ICEN1+M3
XFSUM0=0.0
FSUM0=0.0
XFSUM1=0.0
FSUM1=0.0

```

CENTR, p. 3

```

DO 20 J=1,256
TABS(J)=TAB(PHI,Y(J))
TABS0(J)=TAB(PHI0LD,Y(J))
20 CONTINUE
DO 15 J=INTB0,INTE0
FSUM0=FSUM0+TABS(J)
XFSUM0=XFSUM0+J*TABS(J)
15 CONTINUE
CEN0=XFSUM0/FSUM0
DO 16 J=INTB1,INTE1
FSUM1=FSUM1+TABS(J)
XFSUM1=XFSUM1+J*TABS(J)
16 CONTINUE
CEN1=XFSUM1/FSUM1
XFSUM=XFSUM1*DIF+XFSUM0*(1-DIF)
FSUM=FSUM1*DIF+FSUM0*(1-DIF)
CENTER=XFSUM/FSUM
CENTR=(CENTER+831. -1 )/(4096. *2. 404E-04)
PHIDEG=PHI*(180./3. 1415926)
WRITE(6,160) 1,CENTR,PHIDEG
160 FORMAT(1X,I2,5X,F15.3,5X,F10.3)
IF(.NOT.1SWTST(1)) GO TO 800
TABMAX=TAB(PHI,Y(1))
TABMIN=TABMAX
TABOMA=TAB(PHI0LD,Y(1))
TABOMI=TABOMA
DO 25 K=1,256
IF(TABS(K).GT.TABMAX) TABMAX=TABS(K)
IF(TABS(K).LT.TABMIN) TABMIN=TABS(K)
IF(TABS0(K).GT.TABOMA) TABOMA=TABS0(K)
IF(TABS0(K).LT.TABOMI) TABOMI=TABS0(K)
25 CONTINUE
SCAL=TABMAX-TABMIN
SCALO=TABOMA-TABOMI
CALL SERASE
CALL SSCALE(512.,SCALO,1.,TABOMI)
DO 30 K=1,256
IP=1
IF(K.EQ.1) IP=0
X=K
CALL SPLOT(IP,X,TABS0(K))
30 CONTINUE
CALL SPOINT(1,CENT,.5*SCALO+TABOMI,.25)
CALL SSCALE(512.,SCAL,257,TABMIN)
DO 40 K=1,256
IP=1
IF(K.EQ.1) IP=0
X=K+256.
CENTR=CENTER+256
CALL SPLOT(IP,X,TABS(K))

```

CENTR, p. 4

```
40      CONTINUE
      CALL SPOINT(1,CENTR,.5*SCAL+TABMIN,.25)
800     IF(ABS(CENT-CENTER).LE.0.001) GO TO 200
      ICOUNT=ICOUNT+1
      IF(ICOUNT.GT.15) GO TO 205
      IF(ISWTST(0)) GO TO 205
      CENT=CENTER
      PHIOLD=PHI
      GO TO 210
205     WRITE(5,150) I,CENTRO,PHIDEG
150     FORMAT(1X,12,' NO CONVERG',F15.3,5X,F10.3)
      GO TO 10
200     WRITE(5,151) I,CENTRO,PHIDEG
151     FORMAT(1X,12,5X,F15.3,5X,F10.3)
      GO TO 10
10      CONTINUE
      WRITE(5,155)
      WRITE(6,155)
155     FORMAT(1H1)
      STOP
      END
```

MULPOL, p. 1

```

C      MULPOL
C
C      MULPOL CALCULATES THE OCTOPOLE MOMENT OF A
C      MENISCUS VOLUME FORMED BY THE INTERSECTION
C      OF TWO SPHERES. CHOICE OF MENISCUS
C      RADIUS, SEPARATION AND ORIGIN OF OCTOPOLE
C      ALSO DOES DIPOLE AND QUADRUPOLE
C
      D1(X,Y,Z)=X*X+Y*Y+Z*Z
      D2(X,Y,Z)=X*X+(Z-SEP)**2+Y*Y
      PI=3.14159265358
      WRITE(6,100)
100    FORMAT(' TYPE THE LINEAR POINT DENSITY ON MENISCUS F7.2')
      READ(6,101) PDS
101    FORMAT(F7.2)
      DEL1=1./PDS
      WRITE(6,104)
104    FORMAT(' TYPE MENISCUS RADIUS')
      READ(6,101) RM
      RMSQ=RM*RM
      WRITE(6,105)
105    FORMAT(' TYPE CENTER SEPARATION')
      READ(6,101) SEP
      WRITE(6,106)
106    FORMAT(' TYPE Z COORD. OF OCTOPOLE ORIGIN')
      READ(6,101) Z0
C
C      NOW GENERATE SPHERE SURFACE
C
      THETA=DEL1
      PHI=0.0
      ICNT=0
210    X=SIN(THETA)*COS(PHI)
      Y=SIN(THETA)*SIN(PHI)
      Z=COS(THETA)
      IF(D2(X,Y,Z).GT.RMSQ) GO TO 200
      ICNT=ICNT+1
      P1(ICNT,1)=X
      P1(ICNT,2)=Y
      P1(ICNT,3)=Z
      P1(ICNT,4)=X
      PHI=PHI+DEL1/SIN(THETA)
      IF(PHI.GT.2.*PI) GO TO 220
      GO TO 210
220    PHI=PHI-2.*PI
      THETA=THETA+DEL1
      IF(THETA.GT.PI/1.5) GO TO 225
      GO TO 210
225    WRITE(6,100)
100    FORMAT(' THETA IS BIGGER THAN PI/1.5')

```

MULPOL, p. 2

```

200    CONTINUE
      WRITE(6,110) ICNT
110    FORMAT(I4,' POINTS ON SPHERE SURFACE')
      A1=(PI/SEP)*(RMSQ-(SEP-1.))**2)
      WRITE(6,111) A1
111    FORMAT(' SPHERICAL AREA IS ',E15.7)
      C
      C    NOW GENERATE POINTS ON MENISCUS SURFACE
      C
      DEL2=DEL1/RM
      THETA=DEL2
      PHI=0.0
      JCNT=0
310    X=RM*SIN(THETA)*COS(PHI)
      Y=RM*SIN(THETA)*SIN(PHI)
      Z=-RM*COS(THETA)+SEP
      IF(D1(X,Y,Z).GT.1.) GO TO 300
      JCNT=JCNT+1
      P2(JCNT,1)=X
      P2(JCNT,2)=Y
      P2(JCNT,3)=Z
      P2(JCNT,4)=X/RM
      PHI=PHI+DEL2/SIN(THETA)
      IF(PHI.GT.2.*PI) GO TO 320
      GO TO 310
320    PHI=PHI-2.*PI
      THETA=THETA+DEL2
      IF(THETA.GT.PI/1.5) GO TO 325
      GO TO 310
325    WRITE(6,100)
300    CONTINUE
      WRITE(6,120) JCNT
120    FORMAT(I4,' POINTS ON MENISCUS SURFACE')
      A2=(PI*RM/SEP)*(1.-(SEP-RM))**2)
      WRITE(6,121) A2
121    FORMAT(' MENISCUS AREA IS ',E15.7)
      C
      C    CALCULATE OCPOLE MOMENT
      C
      POL1=0.0
      QPOL1=0.0
      DIPOL1=0.0
      C21=0.0
      DO 500 I=1,ICNT
      DX=P1(I,1)
      DY=P1(I,2)
      DZ=P1(I,3)-Z0
      RSQ=D1(DX,DY,DZ)
      POL1=POL1+P1(I,4)*(5.*DZ**2-RSQ)*P1(I,1)
      QPOL1=QPOL1+P1(I,4)*3.*P1(I,1)*DZ

```

MULPOL, p. 3

```

DIPOL1=DIPOL1+P1(1,4)*P1(1,1)
500 CONTINUE
C21=C21+P1(1,4)*(DX**3-3.*DX*DY**2)
POL1=POL1*A1/ICNT
QPOL1=QPOL1*A1/ICNT
DIPOL1=DIPOL1*A1/ICNT
C21=C21*A1/ICNT
C22=0.0
POL2=0.0
QPOL2=0.0
DIPOL2=0.0
DO 510 J=1,JCNT
DX=P2(J,1)
DY=P2(J,2)
DZ=P2(J,3)-Z0
RSQ=D1(DX,DY,DZ)
POL2=POL2+P2(J,4)*(5.*DZ**2-RSQ)*P2(J,1)
QPOL2=QPOL2+P2(J,4)*3.*P2(J,1)*DZ
DIPOL2=DIPOL2+P2(J,4)*P2(J,1)
C22=C22+P2(J,4)*(DX**3-3.*DX*DY**2)
510 CONTINUE
POL2=POL2*A2/JCNT
QPOL2=QPOL2*A2/JCNT
DIPOL2=DIPOL2*A2/JCNT
C22=C22*A2/JCNT
POL8=(POL1+POL2)*.72E-06*3.
QPOL=(QPOL1+QPOL2)*.72E-06
DIPOL=(DIPOL1+DIPOL2)*.72E-06
C2=(C21+C22)*5.*.72E-06
WRITE(6,125) POL8
WRITE(6,128) C2
128 FORMAT(' OCTOPOLE MOMENT C2= ',E15.7)
125 FORMAT(' OCTOPOL MOMENT C1= ',E15.7)
WRITE(6,126) QPOL
WRITE(6,127) DIPOL
126 FORMAT(' QUADRUPOLE= ',E15.7)
127 FORMAT(' DIPOLE= ',E15.7)
STOP
END

```


DIPAV

```

FR(U, R, S)=S*U+SQRT((S*U)**2+R**2-S**2)
310 WRITE (6, 311)
311 FORMAT (' TYPE IN # OF STEPS (16)')
READ (6, 312) ISTEP
312 FORMAT (I6)
BM=ISTEP
WRITE (6, 300)
300 FORMAT (' TYPE IN MENIS RAD (F6. 3)')
READ (6, 301) A
301 FORMAT (F6. 3)
WRITE (6, 302)
302 FORMAT (' TYPE IN SEP (F6. 3)')
READ (6, 301) S
SUM=0.
D=S
DS=0.
101 FORMAT (F4. 2)
RAT=. 5*(A**3+1+(S**4-6. *(S*A)**2-6. *S**2
1+6. *A**2-3-3. *A**4)/(8. *S))
713 CONTINUE
200 FORMAT (F6. 4)
I=0
901 I=I+1
U=1-I/BM
RMIN=FR(U, A, DS)
RMAX=FR(U, 1., D)
990 IF (RMAX. LE. RMIN) GO TO 902
SUM=SUM+(1-3*U**2)*ALOG(RMAX/RMIN)/BM
GO TO 901
902 UMIN=U
SUM=3. 14159265*SUM*RAT/(1-RAT)
ERR=SUM*0. 719E-06
ERRAT=ERR/RAT
WRITE (5, 903) A, S, ERR, ERRAT
903 FORMAT(1X, F9. 4, 5X, F9. 4, 5X, E15. 7, 10X, E15. 7, //)
501 CONTINUE
GO TO 310
END

```

QUADAV

```

FR(U, R, S)=S*U+SQRT((S*U)**2+R**2-S**2)
RU(RMIN, RMAX)=1./RMIN-1./RMAX
BM=1000
WRITE (6, 302)
302  FORMAT (' TYPE IN MENIS. RAD. (F6. 3)')
    READ (6, 301) A
    WRITE (6, 303)
303  FORMAT (' TYPE IN SEPARATION (F6. 3)')
    READ (6, 301) S
    WRITE (6, 300)
300  FORMAT (' TYPE IN Z COORD (F6. 3)')
    READ (6, 301) D
301  FORMAT (F6. 3)
    DS=D-S
101  FORMAT (F4. 2)
    RAT=. 5*(A**3+1+(S**4-6. *(S*A)**2-6. *S**2
    1+6. *A**2-3-3. *A**4)/(8. *S))
200  FORMAT (F6. 4)
    I=-1
901  I=I+1
    U=1-I/BM
    RMIN=FR(U, A, DS)
    RMAX=FR(U, 1., D)
990  IF (RMAX. LT. RMIN) GO TO 902
    SUM=SUM+(U*(3. -5. *U**2)*RU(RMIN, RMAX))/BM
    GO TO 901
902  UMIN=U
    SUM=3. *SUM/(4. *(1-RAT))
    ERR=SUM
    WRITE (5, 903) A, S, D, UMIN, RAT, ERR
903  FORMAT (1X, F5. 3, 5X, F5. 3, 5X, F5. 3, /
    1F6. 3, 25X, F5. 3, 5X, E15. 7, //)
501  CONTINUE
    END

```

OCTAV

```

FR(U, R, S)=S*U+SQRT((S*U)**2+R**2-S**2)
RU(RMIN, RMAX)=(1./RMIN**2-1./RMAX**2)/2.
BM=1000
350 WRITE (6,302)
302 FORMAT (' TYPE IN MENIS RAD (F6.3)')
READ (6,301) R
WRITE (6,300)
300 FORMAT (' TYPE IN Z COORD (F6.3)')
READ (6,301) D
S=D
301 FORMAT (F6.3)
DS=D-S
101 FORMAT (F4.2)
RAT= .5*(R**3+1+(S**4-6. *(S*R)**2-6. *S**2
1+6. *R**2-3-3. *R**4)/(8. *S))
200 FORMAT (F6.4)
I=-1
901 I=I+1
U=1-I/BM
RMIN=FR(U, R, DS)
RMAX=FR(U, 1., D)
990 IF (RMAX.LT.RMIN) GO TO 902
SUM=SUM+(30. *U**2-35. *U**4-3. ) *
1RU(RMIN, RMAX)/BM
GO TO 901
902 UMIN=U
SUM=3. *SUM/(32. *(1-RAT))
ERR=SUM
WRITE (5,903) R, S, ERR, RAT
903 FORMAT(1X, F5.3, 5X, F5.3, 5X, E15.7, 10X, E15.7, /)
501 CONTINUE
GO TO 350
END

```

NECK, p. 1

```

C      NECK
C      CALCULATES FIELD DUE TO NECK AVERAGED OVER THE MENISCUS
C
C      DIMENSION P1(2000,3)
C      D1(X,Y,Z)=X*X+Y*Y+Z*Z
C      D2(X,Y,Z)=X*X+Y*Y+(Z-SEP)**2
C      PI=3.14159265358
C      WRITE(6,100)
100    FORMAT(' NECKB ASSIGN INOUT TO 1 BEFORE RUN')
C      READ(1,101) PDS
101    FORMAT(F7.3)
C      DEL1=1./PDS
C      READ(1,101) RM
C      RMSQ=RM*RM
C      READ(1,101) SEP
C      READ (1,501) NDIP
501    FORMAT (I2)
C      READ (1,503) H0
503    FORMAT (F7.3)
C      READ (1,503) DH
C      READ (1,503) RI
C      READ (1,503) RO
C      READ(1,504) ISTOP
504    FORMAT(I2)
C      WRITE(5,250) PDS,RM,SEP,NDIP
250    FORMAT(/'/ PDS= ',F7.3,'RM= ',F7.3,'SEP= ',F7.3,'NDIP=',I2)
C      WRITE(5,251) H0,DH,RI,RO
251    FORMAT(' H0=',F7.3,'DH=',F7.3,'RI=',F7.3,'RO=',F7.3)
C      RNK=SQRT(RI*RI/2+RO*RO/2)
C      V=DH*PI*(RO*RO-RI*RI)/NDIP
C      DIP=1.08E-06*V
C      BTOT=0.0
C      H=H0
C
C      ICNT=0
C      Z=1.
203    Y=1.
202    X=1.
201    IF(D1(X,Y,Z).GT.1.) GO TO 206
C      IF(D2(X,Y,Z).GT.RMSQ) GO TO 200
C      ICNT=ICNT+1
C      P1(ICNT,1)=X
C      P1(ICNT,2)=Y
C      P1(ICNT,3)=Z
200    X=X-DEL1
C      IF(X.LT.-1.) GO TO 210
C      GO TO 201
210    Y=Y-DEL1
C      IF(Y.LT.-1.) GO TO 220

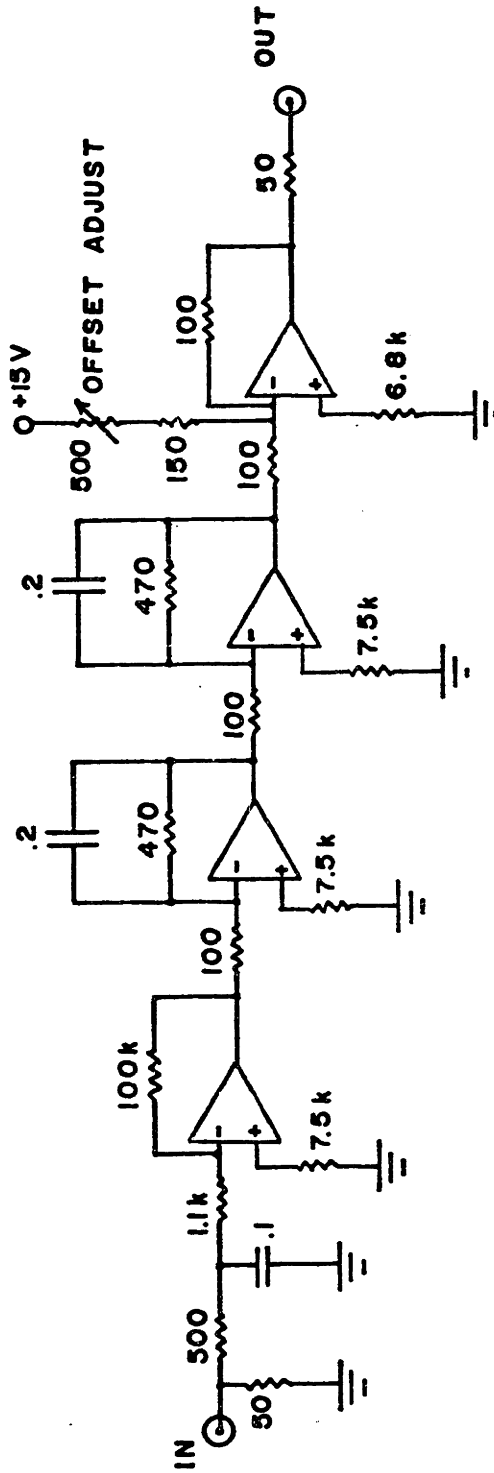
```

NECK, p. 2

```

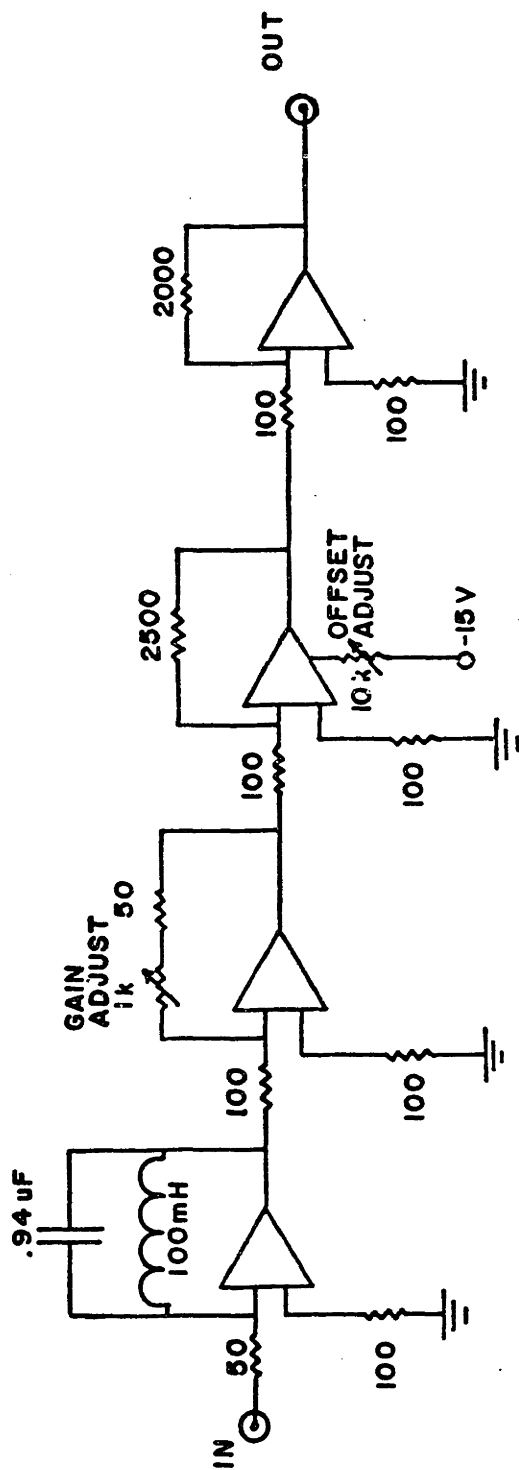
      GO TO 202
220  Z=Z-DEL1
      IF(Z.LT.-1.) GO TO 230
      GO TO 203
230  CONTINUE
      WRITE(6,150) ICNT
      WRITE(5,150) ICNT
      ICALC=0
150  FORMAT(' NO. OF MENISCUS POINTS IS',I4)
      C
      C   GENERATE NECK PTS AN CALC FIELD AVE
      C
799  B=0.0
      PHI=0.0
      DO 700 I=1,NDIP
      X=RNK*COS(PHI)
      Y=RNK*SIN(PHI)
      DO 710 J=1,ICNT
      DX=X-P1(J,1)
      DY=Y-P1(J,2)
      DZ=H-P1(J,3)
      DRSQ=D1(DX,DY,DZ)
      C
      WRITE(6,400) DX,DRSQ,DIP,DZ
400  FORMAT(4E15.7)
      B=B+DIP*(3.*DX*DX/DRSQ-1.)/(SQRT(DRSQ))**3
710  CONTINUE
      PHI=PHI+2.*PI/NDIP
700  CONTINUE
      BAVE=B/ICNT
      BTOT=BTOT+BAVE
      TEST=ABS(BAVE/BTOT)
      WRITE (5,550) BAVE,BTOT
      WRITE (6,550) BAVE,BTOT
      IF(TEST.LE.0.5E-02) GO TO 798
550  FORMAT(1X,'BAVE= ',E15.4,' BTOT= ',E15.4)
      H=H+DH
      ICALC=ICALC+1
      IF(ICALC.LT.1STOP) GO TO 799
798  STOP
      END

```



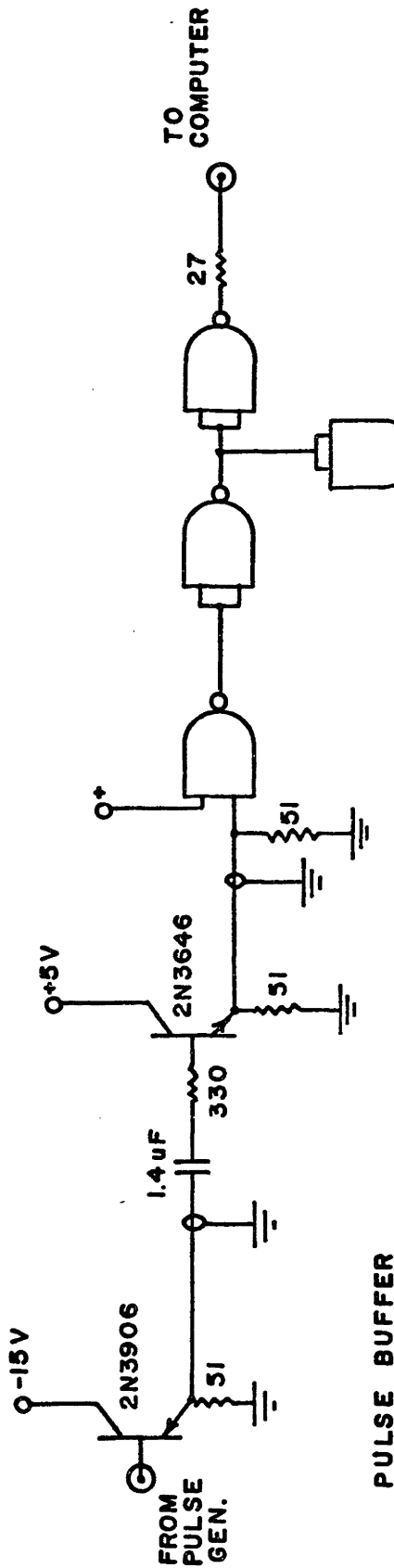
R in OHMS
C in uF
OP AMP = 747

FIG. D1 MASER AUDIO AMPLIFIER

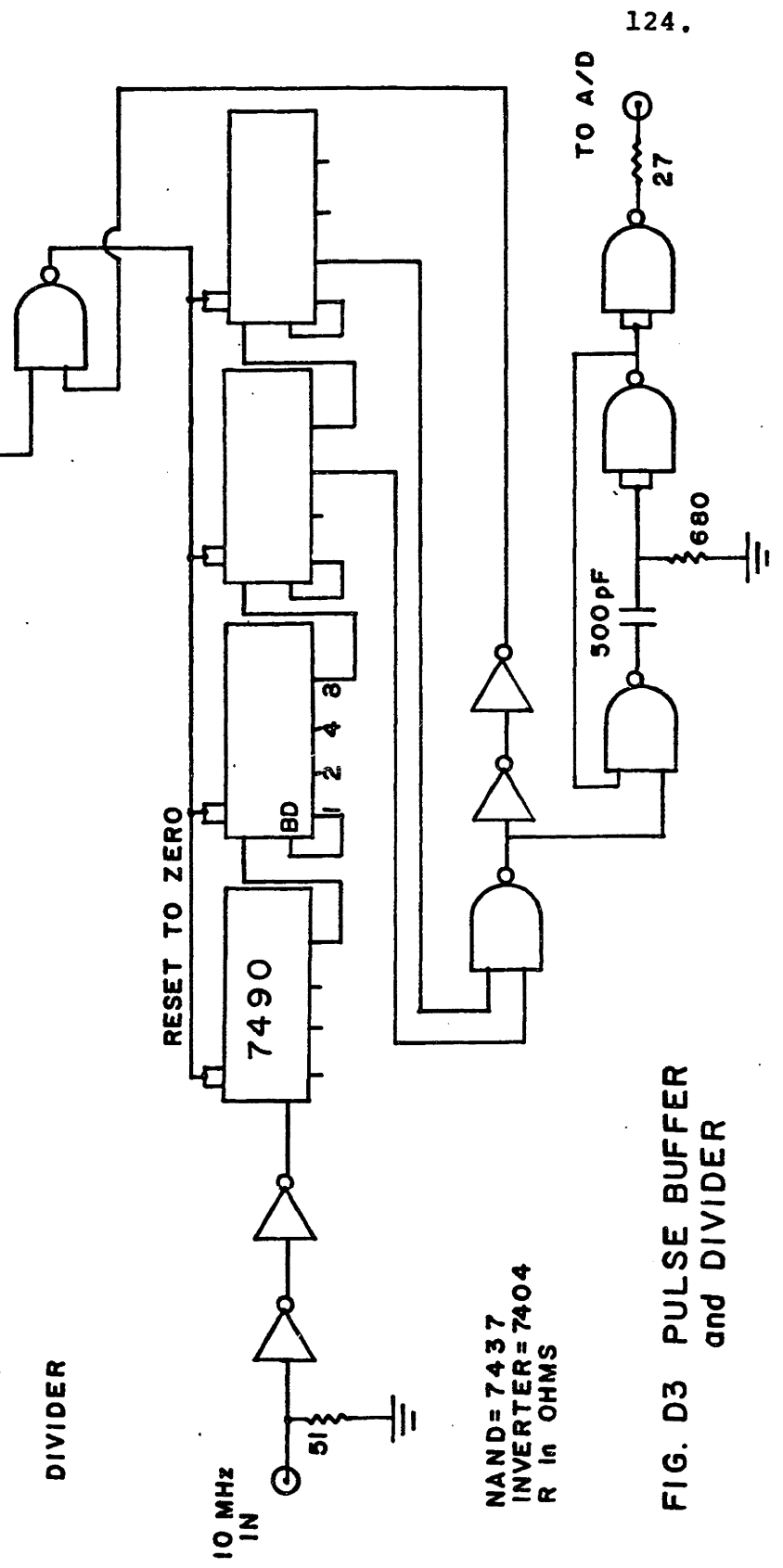


R in OHMS
OP AMP = 747

FIG. D2 NMR AUDIO AMPLIFIER



PULSE BUFFER



DIVIDER

NAND = 7437
 INVERTER = 7404
 R in OHMS

FIG. D3 PULSE BUFFER and DIVIDER

REFERENCES

PART ONE

- ABR61 A. Abragam, Principles of Nuclear Magnetism, Oxford, London, 1961.
- BEL72 R.J. Bell, Introductory Fourier Transform Spectroscopy, Academic Press, New York, 1972.
- COH73 E.R. Cohen and B.N. Taylor, J. Phys. Chem. Ref. Data 2, 663 (1973).
- COO66 J.W. Cooley and J.W. Tukey, Mathematics of Computations 19 (1966).
- CRA73 S.B. Crampton, private communication.
- CRC62 Handbook of Chemistry and Physics, 44th edition, Chemical Rubber Co., Cleveland, 1962.
- FAR71 T.C. Farrar and E.D. Becker, Pulse and Fourier Transform NMR, Academic Press, New York, 1971.
- GRO71 H. Grotch and R.A. Hegstrom, Phys. Rev. A 4, 59 (1971).
- HIN66 J.C. Hindman, J. Chem. Phys. 44, 4582 (1966).
- KLE62 D. Kleppner, H.M. Goldenberg and N.F. Ramsey, Phys. Rev. 126, 603 (1962).
- LAM59 E.B.D. Lambe, Ph.D. Thesis, Princeton University, 1959 (unpublished)
- LAM75 E.B.D. Lambe, private communication.
- MYI66 T. Myint, Ph.D. Thesis, Harvard University, 1966 (unpublished)
- OLS76 P.T. Olsen and E.R. Williams in Atomic Masses and Fundamental Constants 5, edited by J.H. Sanders and A.H. Wapstra, Plenum Press, New York, 1976.
- PHI72 W.D. Phillips, F.G. Walther and D. Kleppner, Third International Conference on Atomic Physics, Aug. 1972, Boulder, Colorado, abstracts of papers.
- PHI75 W.D. Phillips, W.E. Cooke and D. Kleppner, Phys. Rev. Lett. 35, 1619 (1975).
- RAM56 N.F. Ramsey, Molecular Beams, Oxford, London, 1956.

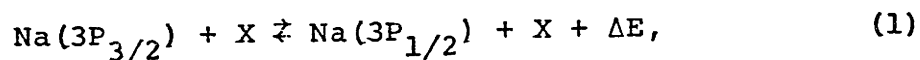
- RAM65 N.F. Ramsey, *Metrologia* 1, 7 (1965).
- RAM75 N.F. Ramsey, private communication.
- REI75 R.V. Reid, *Phys. Rev. A* 11, 403 (1975).
- RIC75 A. Rich, private communication.
- SCH58 W.G. Schneider, H.J. Bernstein and J.A. Pople, *J. Chem. Phys.* 28, 601 (1958).
- SLI63 C.P. Slichter, Principles of Magnetic Resonance, Harper and Row, New York, 1963.
- STR41 J.A. Stratton, Electromagnetic Theory, McGraw Hill, New York, 1941.
- TAY69 B.N. Taylor, W.H. Parker and D.N. Langenberg, *Rev. Mod. Phys.* 41, 375 (1969).
- VAL69 P.A. Valberg, Ph.D. Thesis, Harvard University, 1969 (unpublished).
- WAL72a F.G. Walther, W.D. Phillips and D. Kleppner, *Phys. Rev. Lett.* 28, 1159 (1972).
- WAL72b F.G. Walther, Ph.D. Thesis, Massachusetts Institute of Technology, 1972 (unpublished).
- WAU74 J.S. Waugh, private communication.
- WES71 J.C. Wesley and A. Rich, *Phys. Rev. A* 4, 1341 (1971).
- WIN70 P.F. Winkler, Ph.D. Thesis, Harvard University, 1970 (unpublished).
- WIN72 P.F. Winkler, D. Kleppner, T. Myint and F.G. Walther, *Phys. Rev. A* 5, 83 (1972).
- WRI74 F.E. Wright, M.S. Thesis, Massachusetts Institute of Technology, 1974 (unpublished).

PART TWO

INELASTIC COLLISIONS IN EXCITED
SODIUM

I. INTRODUCTION

Inelastic collisions of the type



have long been the subject of experimental investigation, and recently have generated considerable theoretical interest as well. These processes have been called "sensitized fluorescence", "excitation transfer", "intermultiplet mixing", and "fine structure transfer collisions" by various authors. We prefer the latter term for the work to be described here.

These processes are of interest for two reasons. First, they yield information about the interaction potentials between atoms, and particularly between excited atoms. Second, they provide a simple example of the case of inelastic collisions and can lead to a better understanding of the more general problem of inelastic collision dynamics.

Determination of interatomic potentials has always been of fundamental importance in molecular physics. Recent theories, especially pseudo potential theories, have allowed the calculation of interaction potentials between alkali and rare gas atoms. These calculations have met with mixed success in predicting experimental results and are in need of more detailed comparison with experiment so that the areas of validity and the nature of the limitations of the theory can be established.

An important application of the theoretical potentials has been to the calculation of the collisional cross sections for fine structure transfer (FSX). While very detailed information about the FSX process may be calculated, there is little detailed experimental data available for comparison. While FSX in the alkali metals has been observed experimentally for many years, only recently have velocity dependences of the cross sections been studied closely, and even the best of these measurements have been of insufficient range or resolution for comparison with some of the important general features of the theory, let alone the details.

If the excited state potentials are known independently to be accurate, an experimental study of FSX processes can serve to test the validity of the methods used to calculate the cross sections. Since these processes are a particularly simple example of inelastic collisions they can serve as a first step in understanding more complicated phenomena such as chemical reactions.

We will briefly review the extent of past experimental and theoretical work on fine structure transfer in the alkalis, and especially of work on collisions of sodium with rare gases, which is the subject of the present work.

The traditional method for observing fine structure transfer (FSX) collisions is to excite the alkali atom to one fine structure state and observe the fluorescence from the other state.

Previous to the work reported here, all such measurements on sodium have been in gas cells.

As early as 1914 Wood (WOO 14) observed FSX in sodium, and in 1928 the first quantitative measurements of the cross section for FSX collisions between Na and a rare gas were made by Lochte-Holtgreven (LOC 28). Although these early measurements were later found to be in error due to effects of radiation trapping (SEI 56), it was established that the thermal average cross sections were of the order of 10^{14} cm². Hanson (HAN 57) made the first measurements of the velocity dependence of the FSX cross section. His technique involved photo dissociation of NaI, using various wavelengths of ultraviolet light to produce Na atoms at a few different velocities, which then collided with Ar or H₂O. Collisional cross sections with Ar showed a decrease with velocity.

More recently, Krause and his coworkers have made extensive measurements of the thermal average FSX cross sections for all the stable alkalis (except Li) in collision with all the stable rare gases. Some collisions with molecules were observed and some excited states higher than the first resonance doublet were observed by these workers. The results for Na on rare gases are contained in (PIT 67). Jordan and Franken (JOR 66) have also obtained average cross sections for Na on rare gases. Gallagher (GAL 68) has measured the temperature dependence of

the FSX cross sections for Rb and Cs colliding with various rare gases. The measurements imply cross sections that increase as v^n with $n=4-9$ for thermal velocities.

Anderson et al. (AND 76) have measured velocity dependence for K on He using beams methods, and find a linear increase with velocity. Most recently Apt and Pritchard (APT 76) have measured velocity dependence of the FSX cross section for Na on several rare gases. The technique used was one suggested by this author and Pritchard (PHI 74) using selective laser excitation. They observe a decrease in the cross section for Na on Ar over their velocity range, and an increase for Na on Xe.

Several investigations have also studied the effects of polarization on the observed cross sections in attempts to determine the dependence of the process on the particular m_j states involved. (ELB 71, SCH 71) Krause (KRA 66) has reviewed much of the experimental work to 1966, and Lijnse (LIJ 72) has made a very complete review of the literature, both experimental and theoretical.

Early applications of perturbation theory to the general problem of energy transfer collisions (LAN 32, ZEN 32) has shown the main features to be expected in the velocity dependence of the cross sections, namely an initial increase to a maximum followed by a decrease as $1/v$ at large v . More recently, estimates of the interaction potentials between excited alkalis and rare

gases have been applied to various semiclassical approximations to the collision problem (MAN 70, DAS 70), producing velocity dependent cross sections valid for certain restricted conditions. Most recently, detailed calculation of the interatomic potentials by Baylis and Pascale and Vandeplanque (BAY 69, PAS 74) have been applied by Reid and Dalgarno and Pascale and Olson to a fully quantum mechanical formulation of the collision problem, yielding specific predictions for the magnitudes, velocity dependences, polarization and scattering angle dependence of the cross sections (REI 73, OLS 75, PAS 76).

These latter more detailed calculations have concentrated on the Na-rare gas systems. For a wide enough range of calculated collision velocities, as expected, the cross section rises as the velocity increases, peaks and then declines at higher velocity. Various secondary peaks and oscillations in the cross section are also seen for some systems. None of these features have been observed in any of the experiments on any of the alkalis. Experiments show cross sections which either rise or fall with velocity depending on the system involved, but no single experiment, or set of experiments on the same system, has had sufficient range and resolution to reveal the existence of a peak in the cross section.

The present work reports results for the velocity dependence of the $3/2 \rightarrow 1/2$ transition in Na. There are several reasons

why we have chosen to study the first sodium resonance doublet. First, excitation from the ground state is possible using a commercially available c.w. single frequency tunable dye laser. Second, the Na-rare gas systems have received the lion's share of the detailed theoretical interest. Finally, the 17 cm^{-1} fine structure interval in the 3P state of Na allows impact energies from a few times to many times this value to be obtained experimentally. With such a range, the velocity at which the cross section peaks should be accessible.

Fig. 1 compares the velocity range accessible to various experiments relative to a hypothetical cross section curve. The velocity scales are of course different for each alkali, since the curve scales with the fine structure separation.

The best results for $\sigma(v)$ from thermal averages are due to Gallagher (GAL 68) on Rb and Cs where the large fine structure separation puts thermal velocities in the rapidly increasing region of the curve. These measurements are of inherently low resolution - although because of the steeply rising $\sigma(v)$ the resolution was as good as 30-40%. The beam measurements of Anderson et al. (AND 76) access a region of the curve which is increasing linearly, we estimate their resolution at about 40% full width. The measurements of Hanson (HAN 57) are in the decreasing region for Na. Resolution is not given, but should be no better than the velocity selection by doppler shift method of Apt and Pritchard (APT 76). While Apt's measurements spanned

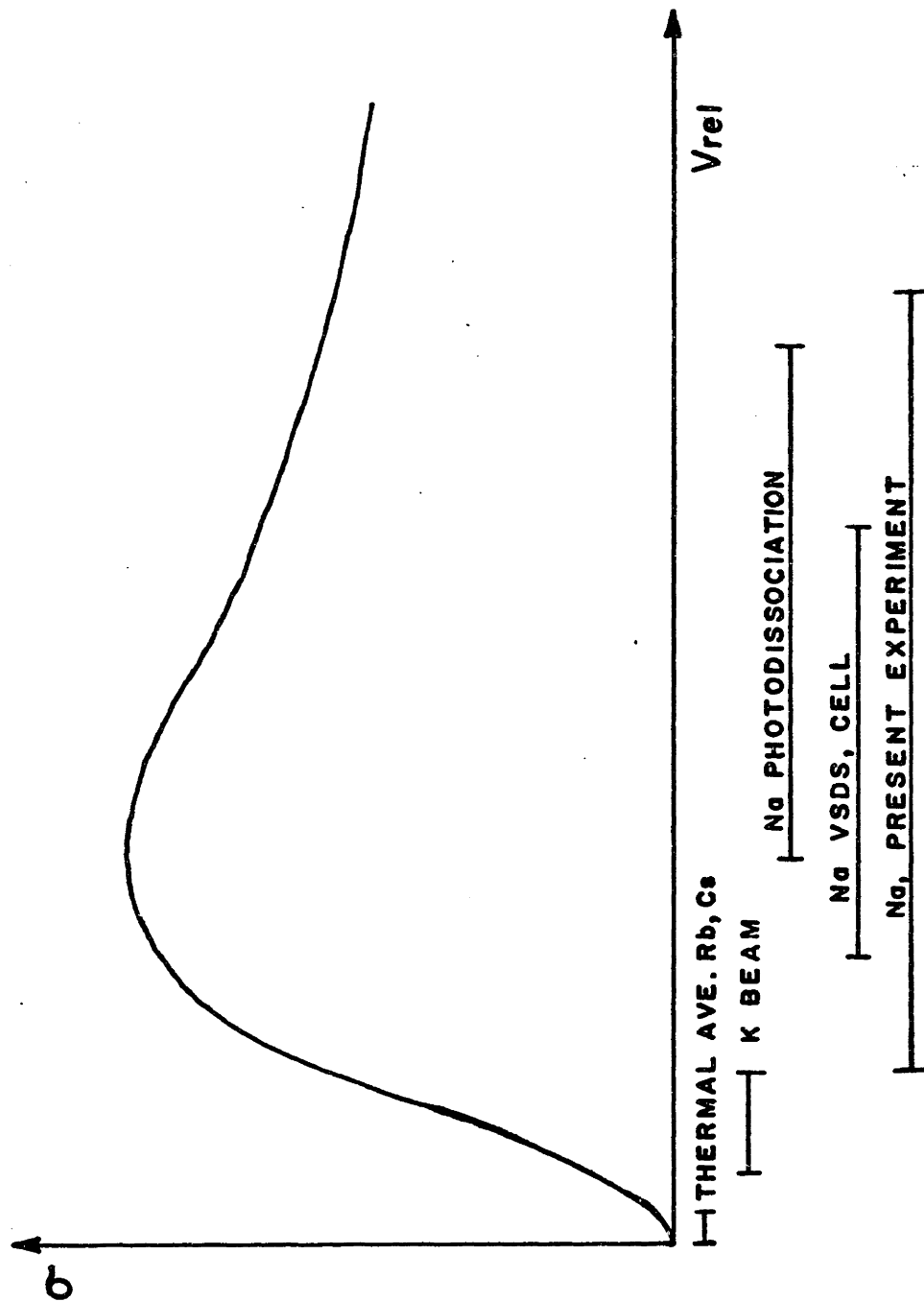


FIG.1 VELOCITY RANGE OF VARIOUS METHODS

the peak region, resolution was too low, especially at low velocity to see its effect on the data. Their resolution was 35% full width at best, but was 90% at the lowest velocities.

The range of our experiment covers the peak of the $\sigma(v)$ curve, with a resolution of no worse than 15% when our highest resolution technique is used.

We measure the FSX cross sections using intersecting atomic beams. The beams of sodium and rare gas atoms originate in supersonic nozzle sources and intersect in a region illuminated by a laser beam which excites Na atoms to the $3P_{3/2}$ state. The number of atoms which change their fine structure state due to collision is determined from the amount of light observed at the $3P_{1/2} \rightarrow 3S_{1/2}$ wavelength. The collisional energy is determined by the velocities of the atoms in each beam and the angle of intersection. The collision energy may be varied by rotating the rare gas beam to change the intersection angle.

An important extension of this technique is to use the exciting laser beam to select the velocity of the Na atoms in the beam. This was suggested in a slightly different context by Hertel et al. (HER 75); our experiment represents the first use of this technique in a colliding beams experiment. Collision energies in the range of .01 to .3 eV have been obtained, and this range is extendable in both directions without major changes in the apparatus. Our technique is not suited to the accurate

measurement of the absolute cross section, so we obtain the cross section $\sigma(v)$ within a normalization constant.

We have obtained $\sigma(v)$ for Na on Ne and Ar for both rotational and laser velocity selection. Some data for Na on He was also obtained. We have determined the energy at which the cross section peaks for Na-Ne and Na-Ar. The velocity dependence for Na-Ar is in good agreement with the best theoretical predictions, but the Na-Ne dependence is in serious disagreement.

II. THEORY.

II.1 Simple Approaches.

There are a number of simple concepts concerning inelastic scattering which can aid in the general understanding of fine structure transfer collisions. We begin with a discussion of the Massey criterion.

Consider a system such as our Na atom with two energy levels, 1 and 2, separated by ΔE (the fine structure separation). If the atom is subjected to a time varying perturbation, V , due to a collision, we would expect transitions between the levels to be induced by this perturbation provided that V has a non zero matrix element between the two states. More precisely, the fourier components of $V(t)$ at frequency $\omega_{12} = \Delta E/\hbar$ will induce the transitions. If we assume the collision to occur over a distance a , then the time τ for the collision is $\tau = a/v$ where v is the relative velocity. Thus if we satisfy the condition

$$\xi = \frac{\Delta E a}{\hbar v} \approx 1 \quad (2)$$

we expect to have the best chance of changing the state of the atom. Satisfaction of condition (2) is known as the Massey criterion. The quantity ξ is known as the Massey or adiabatic parameter. For $\xi \gg 1$ the collision is adiabatic while for $\xi \ll 1$ it is sudden.

These qualitative considerations are given a quantitative footing in Landau-Zener theory (LAN32, ZEN32). Our discussion follows that of Zener. We consider a two level atom involved in a perturbing collision. We further assume that in the absence of coupling between the two levels that they would cross at some value of the internuclear separation, R . It is a well known result that with coupling the levels actually repel with a separation given by twice the coupling. The situation is shown in Fig. 2.

We choose as a basis set the asymptotic wavefunctions at large R , ϕ_i . The Hamiltonian is not diagonal in this basis because of the interaction term. Diagonalizing the Hamiltonian at each value of R would produce wavefunctions giving the solid, adiabatic potential curves of Fig. 2.

We follow the usual perturbation theory approach of expanding the true wave function ψ as

$$\psi(t) = c_1 e^{i \int_{-\infty}^t \omega_1(t) dt} \phi_1 + c_2 e^{i \int_{-\infty}^t \omega_2(t) dt} \phi_2 \quad (3)$$

where ω_1 and ω_2 are the unperturbed Bohr frequencies of states 1 and 2. We assume that the transitions will all occur in the crossing region, that the ϕ_i are constant in this region and the matrix element

$$V_{12} = \int \phi_1 V \phi_2 \quad (4)$$

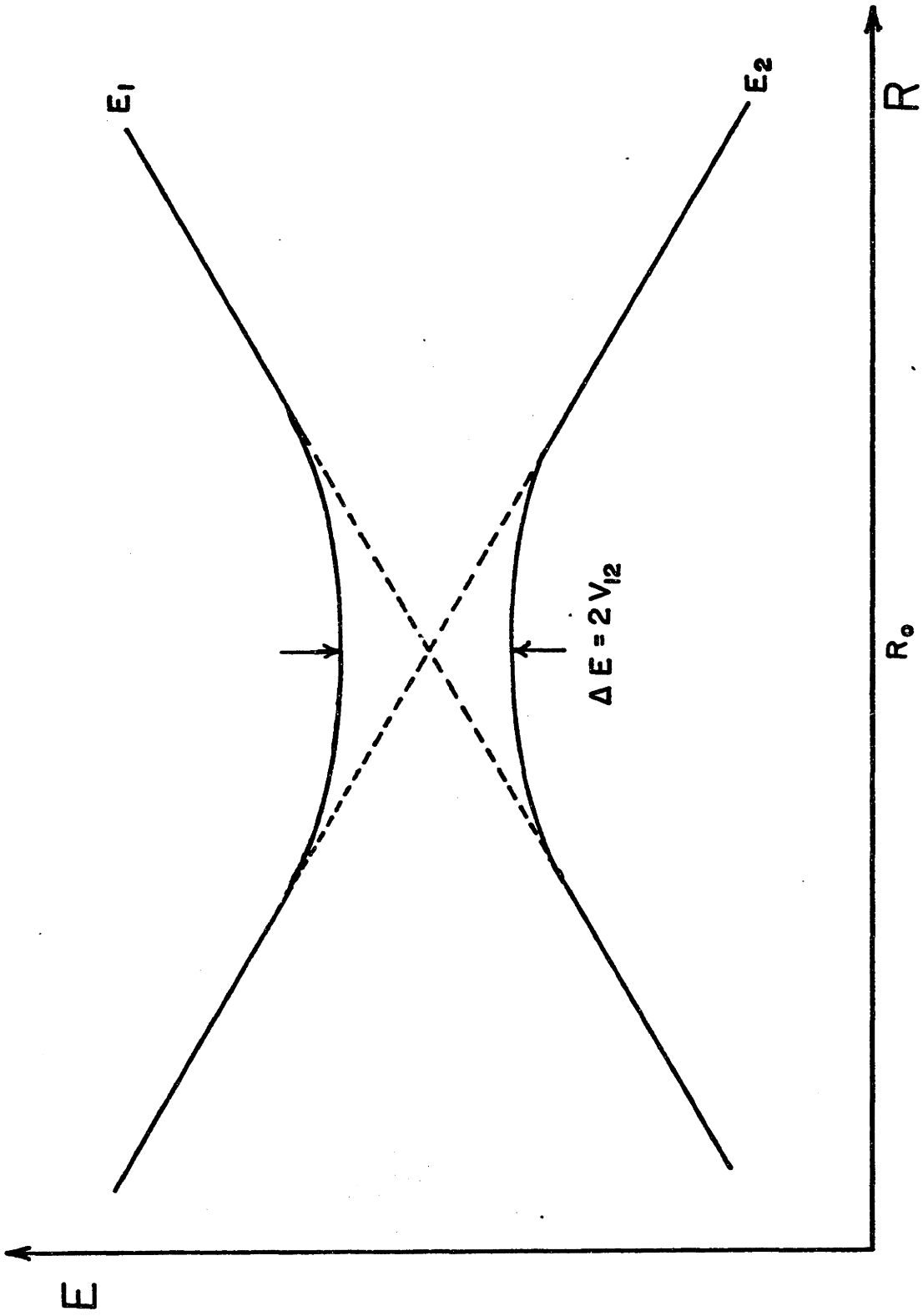


FIG. 2 AVOIDED CROSSING

is also constant. We further assume that the ω_i vary linearly with time, which is equivalent to a linear variation with R and a constant velocity during the collision.

The usual first order coupled equations are obtained:

$$i\hbar\dot{c}_1 = V_{12}e^{i\int_{-\infty}^t(\omega_1 - \omega_2)dt} c_2$$

$$i\hbar\dot{c}_2 = V_{21}e^{i\int_{-\infty}^t(\omega_2 - \omega_1)dt} c_1$$
(5)

using the boundary conditions corresponding to the atom starting in state 1:

$$c_1(-\infty) = 1$$

$$c_2(-\infty) = 0$$
(6)

and the other assumptions, an asymptotic solution may be found for $c_2(\infty)$ after passing through the crossing region:

$$|c_2(\infty)|^2 = e^{-2\pi\gamma}$$

$$\gamma = \left(\frac{V_{12}}{\hbar}\right)^2 \bigg/ \frac{d}{dt} |\omega_2 - \omega_1|$$
(7)

If we define the length of the crossing region to be

$$a = 2V_{12} \bigg/ \frac{d}{dR} |\hbar\omega_2 - \hbar\omega_1|$$
(8)

and recall that $dR/dt = v$, and $\Delta E = 2V_{12}$, we obtain

$$P = |c_2(\infty)|^2 = e^{-\frac{\pi}{2} \xi} \quad (9)$$

$$\xi = \frac{a\Delta E}{\hbar v} .$$

So we obtain the Massey parameter as the determining quantity in the transition probability.

In an actual collision the atoms will in general traverse the crossing point R_0 , continue to the turning point and pass through R_0 again as they separate. The probability of curve jumping is given by (9) each time crossing occurs. If we ignore the effects of coherence between the states the final probability that the atom which started in state 1 will be in state 2 after the atoms separate is*:

$$P_{\text{tot}} = 2P(1 - P) = 2e^{-\frac{\pi}{2} \xi} (1 - e^{-\frac{\pi}{2} \xi}) \quad (10)$$

This function is plotted against $\frac{1}{\xi} \propto v$ in Fig. 3. The transfer probability rises sharply at first, reaches a maximum when the Massey parameter is of the order of 1 ($\xi_{\text{max}} = \frac{2 \ln 2}{\pi}$) and falls off as $1/v$ at large velocities. This confirms the qualitative expectations concerning the behavior of the inelastic cross section as a function of the Massey parameter.

There are of course many limitations to Landau-Zener theory. Besides the approximations noted, it treats only

*See note at end of theory section.

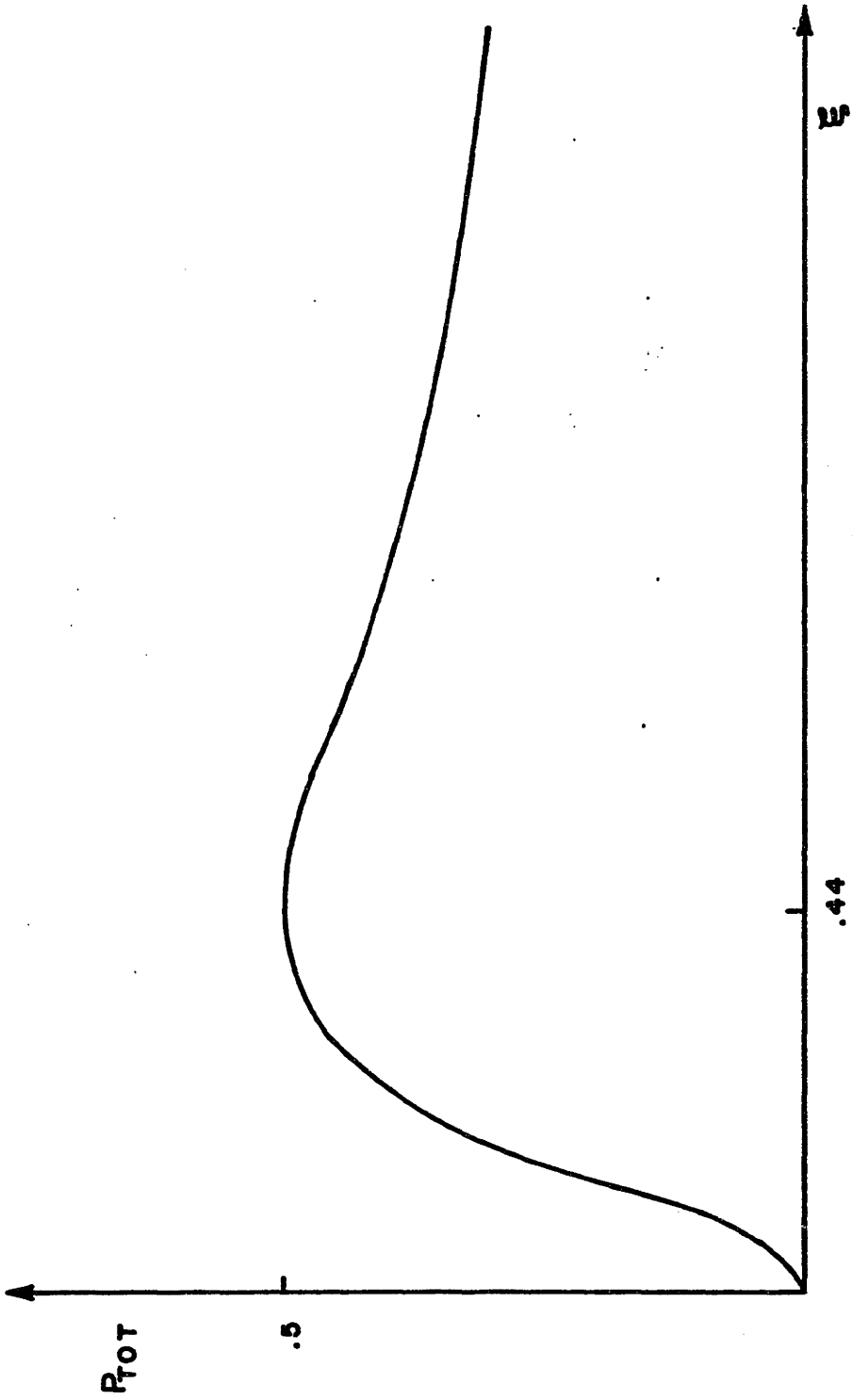


FIG. 3 LANDAU-ZENER TRANSITION PROBABILITY

radial coupling - that is transitions are induced by changes in the internuclear separation. In a real situation there may be rotational coupling due to the rotation of the internuclear axis. There may be no avoided crossing in the adiabatic potentials, or regions other than the crossing may contribute significantly to the transition probability. More sophisticated techniques are necessary for the accurate calculation of real cases.

II.2 Molecular Potentials

As a prelude to the discussion of the more realistic methods for calculating fine structure transition cross sections, we will consider in more detail the nature of the adiabatic potentials. Fig. 4 shows the potentials calculated by Pascale and Vandeplanque (PAS74) for the Na-Ar system. The levels approach the 3p levels at large separation, while at smaller separations the potentials are labeled according to molecular notation (HER50). The Na-Ar system is thought of as a quasi molecule during the collision.

The molecular coupling scheme can be understood as follows: as the atoms approach each other the spherical symmetry of the isolated atom is replaced by an axial symmetry about the internuclear axis. Whereas the orbital angular momentum \vec{L} is a conserved quantity for the isolated atom (neglecting spin-orbit coupling), only the projection of \vec{L} along the inter-

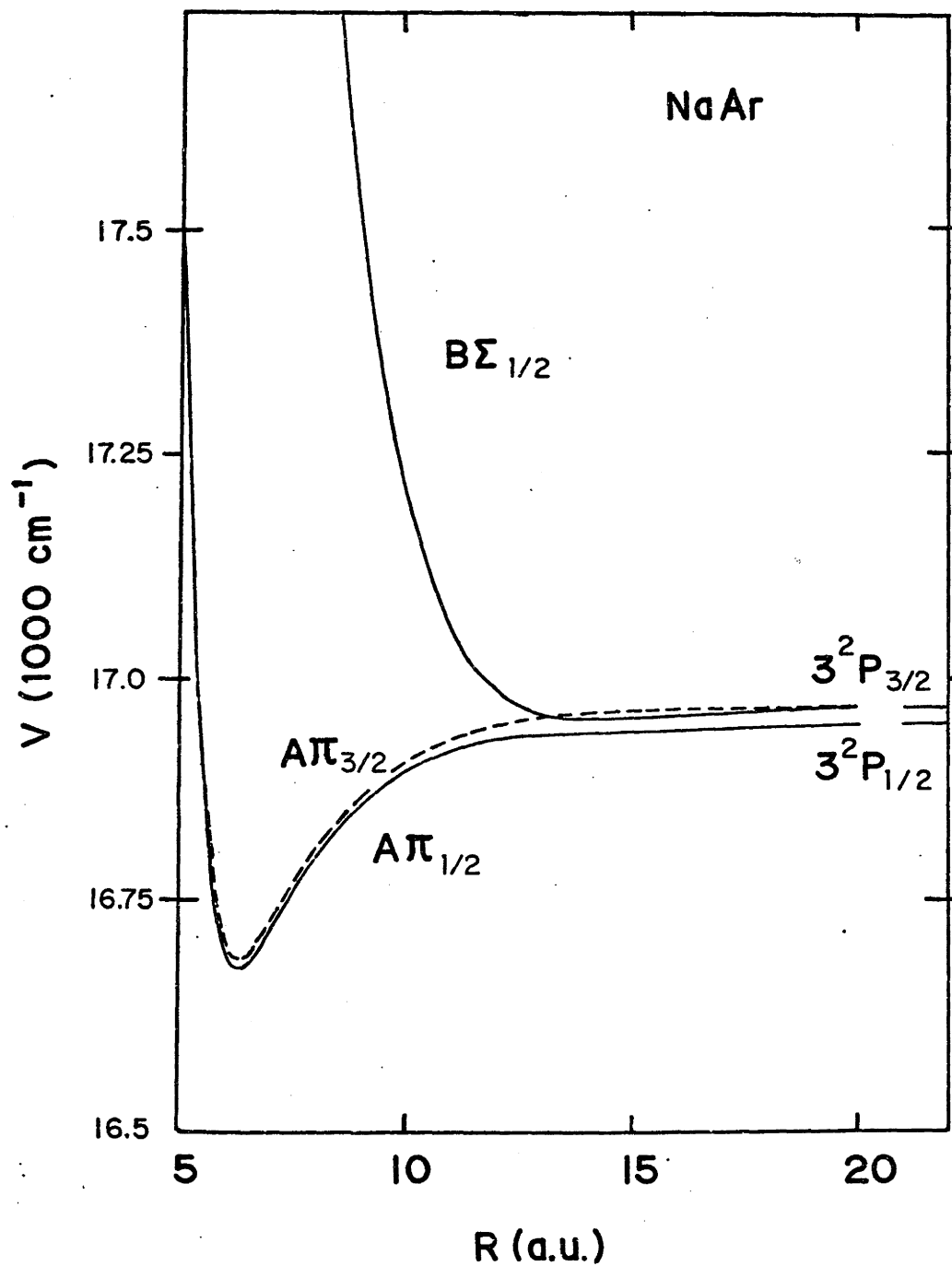


FIG. 4 Na-Ar POTENTIALS

nuclear axis is conserved for the molecule. The absolute value of this projection is the quantum number Λ which takes on the values $\Lambda = 0, 1$ for states derived from atomic P states. These values of Λ correspond to the molecular Σ and Π states respectively.

The electron spin is not directly affected by the molecular field, but for $\Lambda \neq 0$ \vec{S} is coupled to the molecular axis via the axial magnetic field produced by the orbital motion of the electrons (this is analogous to L·S coupling in a free atom). As with \vec{L} , only the projection of \vec{S} , denoted by Σ is conserved. The total angular momentum projected on the axis is $\Omega = |\Lambda + \Sigma|$. For the Π state in Fig. 4 $\Sigma = 1/2$ and can be oriented either with or against Λ , so $\Omega = 1/2, 3/2$. The splitting between the two states is analogous to the fine structure splitting of the isolated atom.

In the molecular representation \vec{L} and \vec{S} are uncoupled from each other and are separately coupled to the molecular axis, in contrast to the isolated atom where the LS coupling is dominant. The region of transition between the two coupling cases (sometimes called Hund's case a and c respectively) occurs when the magnitude of the molecular energy is comparable to the fine structure separation.

II.3 Semiclassical Theory

The semiclassical approach to calculation of fine struc-

ture transfer cross sections involves the selection of a classical trajectory for the collision partners. Given the path and the interactions, the evolution of a given state is calculated either through perturbation theory as in Landau-Zener theory or by direct integration of Schoedinger's equation. Much of the semiclassical theory has been developed by Nikitin and his co-workers (NIK65, DAS70a). We will discuss some of the physical insights which arise from the semiclassical considerations.

Fig. 5 shows a set of hypothetical potential curves similar to those of Fig. 4. We have shown how states of various m_j in the atomic representation go adiabatically into the molecular states. The $\Sigma_{1/2}$ state is formed from states with $m_j = 1/2$ as is the $\Pi_{1/2}$ (the molecular axis is the quantization axis for both the molecular and atomic basis). In the absence of rotation of the molecular axis only states composed of the same m_j are coupled by the axially symmetric molecular field. The situation is similar to the coupling of the two levels in the Landau-Zener theory. This results in mixing of the $\Sigma_{1/2}$ and $\Pi_{1/2}$ states in the vicinity of R_1 as the collision proceeds from the region of atomic to molecular coupling. As with the Landau-Zener case, in the transition region the $\Sigma_{1/2}$ and $\Pi_{1/2}$ states are each composed of both $P_{1/2}$ and $P_{3/2}$ states. The symmetry requirements of the molecular potential which produces this mixing will be discussed in the next section.

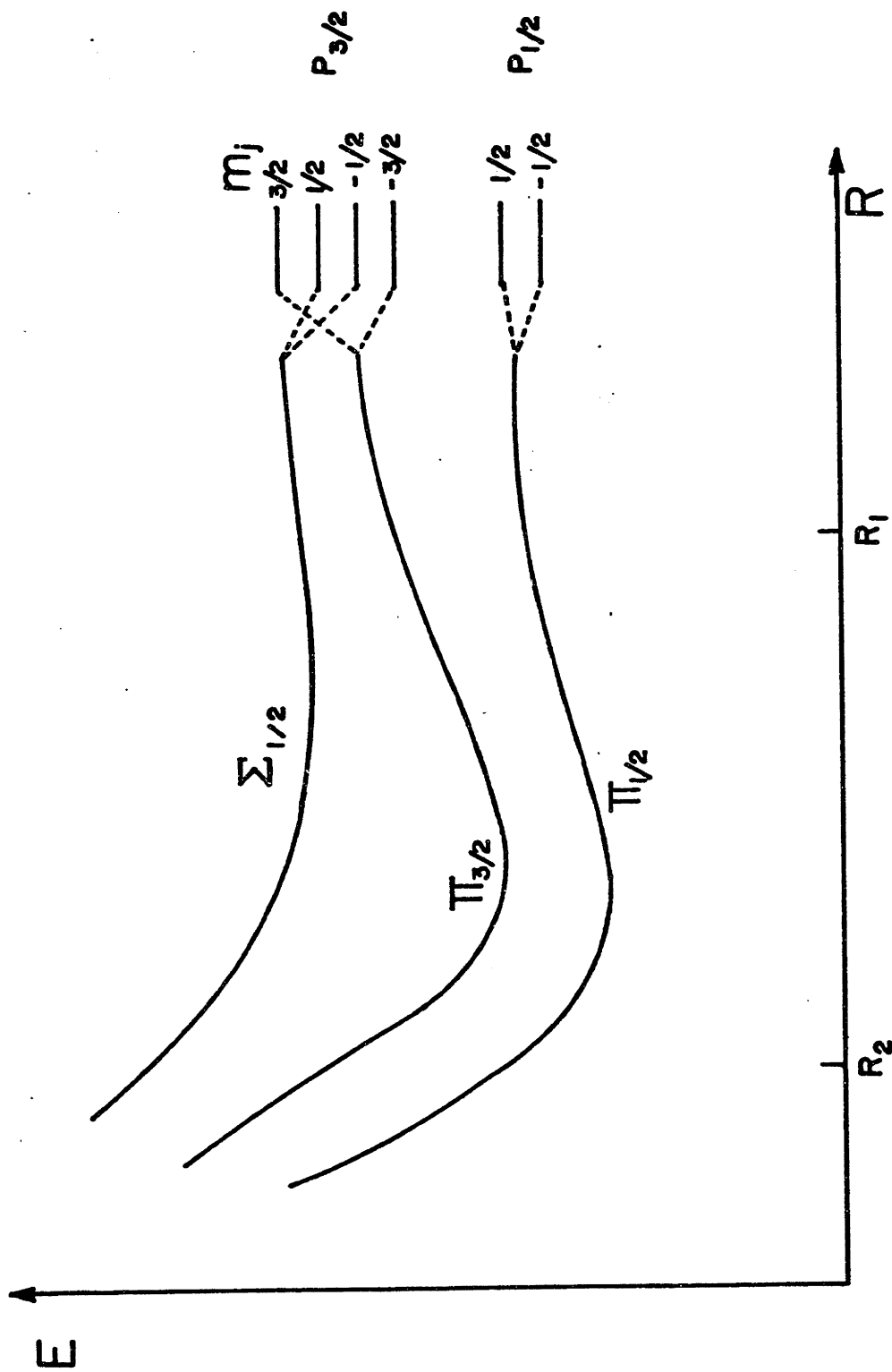


FIG.5 COUPLING REGIONS

Since there is in fact rotation of the molecular axis during the collision, the foregoing discussion must be modified. This rotation is only significant if it is faster than the electronic wave function can follow, that is if the angular frequency of rotation is comparable to the angular frequency difference between the states. At large R the rotation is slow, so only the $\Sigma_{1/2}$ and $\Pi_{3/2}$ states which become degenerate at large R are coupled rotationally. This does not produce a fine structure transition (only a depolarization). At small R in the vicinity of R_2 the situation is quite different. Here the rotational frequency may be significant compared with the $\Pi_{3/2}$ to $\Pi_{1/2}$ separation. Physically what is happening is that the electron spin which is coupled to the internuclear axis by the axial magnetic field cannot follow the rotation when it is faster than the coupling frequency. Classically we would say that the rotation of the axis becomes comparable with the precessional frequency of the spin about the axis, which decouples the spin from the axis.

The semiclassical calculations have had some success in predicting the behavior of cross sections for nearly adiabatic collisions such as those involving Cs at thermal energies (DAS70b). For a system such as Na with a much smaller fine structure separation the relevant velocities are correspondingly smaller, involving less angular momentum in the collision and invalidating the assumption of a classical path.

II.4 Quantum Theory

The first fully quantum mechanical treatment of the fine structure transition problem was given by Reid and Dalgarno (REI69). Reid has given a detailed account of the method involved (REI73) and our discussion follows his.

We consider only the 3p configuration of Na and assume that the interaction potential with the rare gas atom depends only on the internal coordinate, \vec{r} , of the Na valence electron and the relative position of the nuclei, \vec{R} . The axial symmetry allows us to expand

$$V(\vec{r}, \vec{R}) = \sum_{\mu} v_{\mu}(r, R) P_{\mu}(\hat{r} \cdot \hat{R}) \quad (11)$$

where the Legendre polynomial P_{μ} contains all of the angular dependence.

Now it can be easily seen that the only values of μ which have any matrix elements among the 3p states are those for which $\mu = 0, 2$. This is because $P_{\mu}(\hat{r} \cdot \hat{R})$ only operates on the orbital part of the Na wave function, which has $L = 1$. The two $L = 1$ eigenfunctions and the tensor operator $P_{\mu}(\hat{r} \cdot \hat{R})$ which appear in the matrix element must, according to the Wigner-Eckart theorem, satisfy the triangle rule for coupling angular momenta. Only $\mu = 0, 1, 2$ can complete the triangle with two legs of $L = 1$, and the fact that the parity is the same for all states requires μ to be even.

Eq. (11) is now reduced to 2 terms. We can integrate over the electron radial wave function which is the same for all states in the 3p configuration to obtain

$$V(\hat{r}, \hat{R}) = v_0(R)P_0(\hat{r} \cdot \hat{R}) + v_2(R)P_2(\hat{r} \cdot \hat{R}) \quad (12)$$

$$v_\mu(R) = \langle 3p | v_\mu(r, R) | 3p \rangle .$$

The interaction is entirely specified if we know $v_0(R)$ and $v_2(R)$. It is possible to derive these two potentials from adiabatic molecular potentials, such as those calculated by Baylis or Pascale and Vandepplanque, if one assumes that the strength of the spin orbit interaction is constant. For example, Reid gives the following expressions for the Σ and Π energies when the spin orbit interaction is neglected:

$$E_\Sigma(R) = v_0(R) + \frac{2}{5} v_2(R) \quad (13)$$

$$E_\Pi(R) = v_0(R) - \frac{1}{5} v_2(R) .$$

It should be noted that the expansion (11) represents an approximation. While at large R the interaction is due to Van der Waals type polarization, at small R the effects of electron exchange are important. These are not expressible as a potential. Eq. (11) assumes that the interaction is nevertheless expressible as an effective potential.

With this assumption, we know the entire interaction. The scattering states are expanded in partial waves which represent the different values of angular momentum of relative motion. An expression for the scattering amplitude is obtained which depends only on kinematic and geometric factors plus a matrix element which must be evaluated numerically.

Reid has obtained results for the differential cross sections for $j_2 \rightarrow j_1$ transitions in the Na-He system, and total cross sections for $j_2^{m_2} \rightarrow j_1^{m_1}$, for various velocities and various choices of potentials, including the Baylis potential. In obtaining the total cross section, the collision axis was assumed to be randomly oriented with respect to the quantization axis.

Olson has used the method of Reid and the potentials of Baylis to calculate the total velocity dependent cross sections for Na, K, and Rb on He, Ne, Ar and for Cs on He. He is in agreement with Reid for Na-He. Pascale and Olson have used the same method with the potentials of Pascale and Vandephanque to obtain total cross sections for Na on He, Ne, Ar, Kr and Xe. Pascale and Olson agree with Olson for Na-He and Na-Ne, but disagree for Na-Ar. This disagreement is partially due to the different potential used and partially due to the wide energy grid which Olson used.

The cross sections of Pascale and Olson for Ne and Ar are shown in Figs. 6, 7. Fig. 8 shows Reid's $(3/2, m_j) \rightarrow (1/2, m_j')$

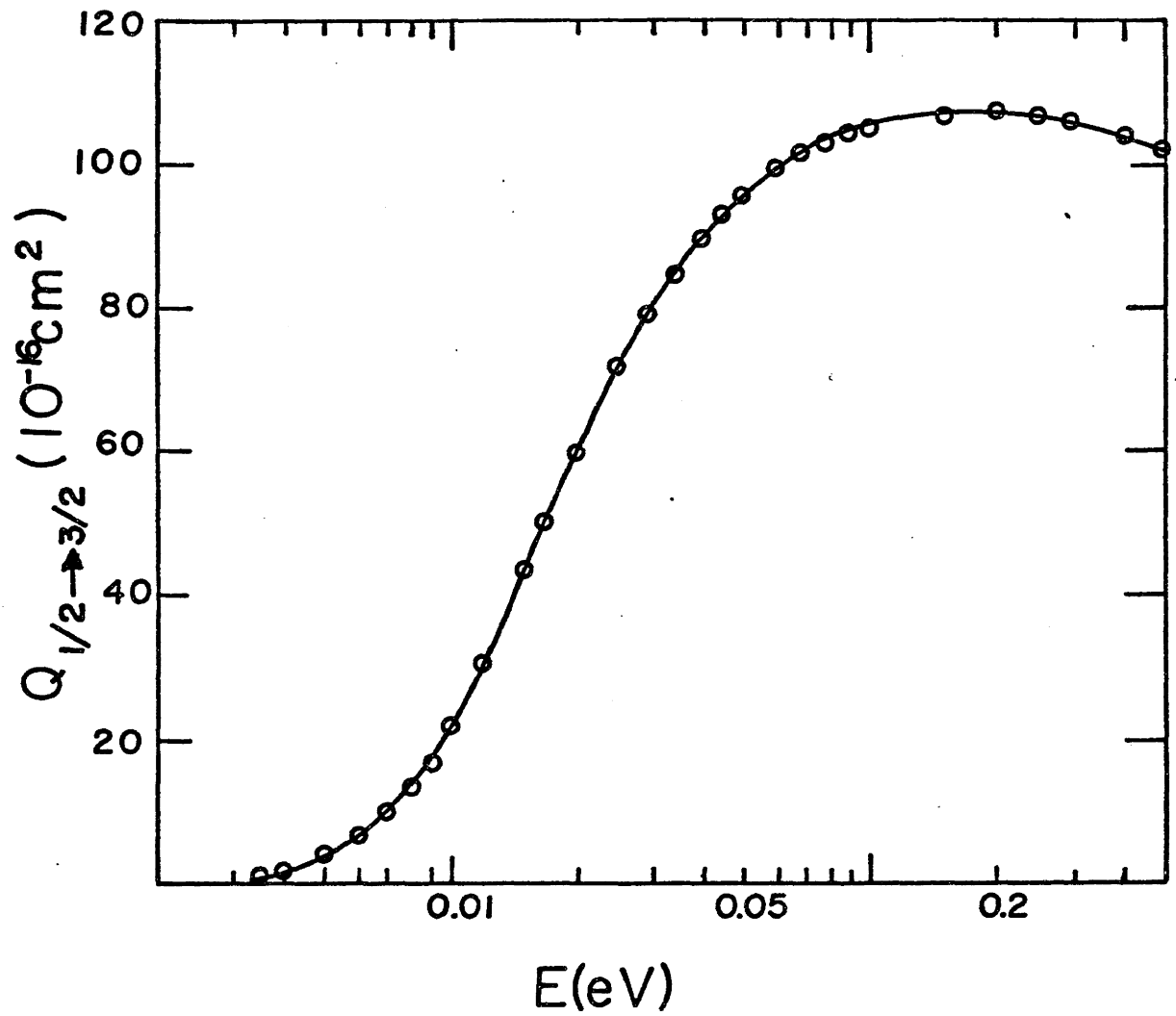


FIG. 6 Na-Ne CROSS SECTION

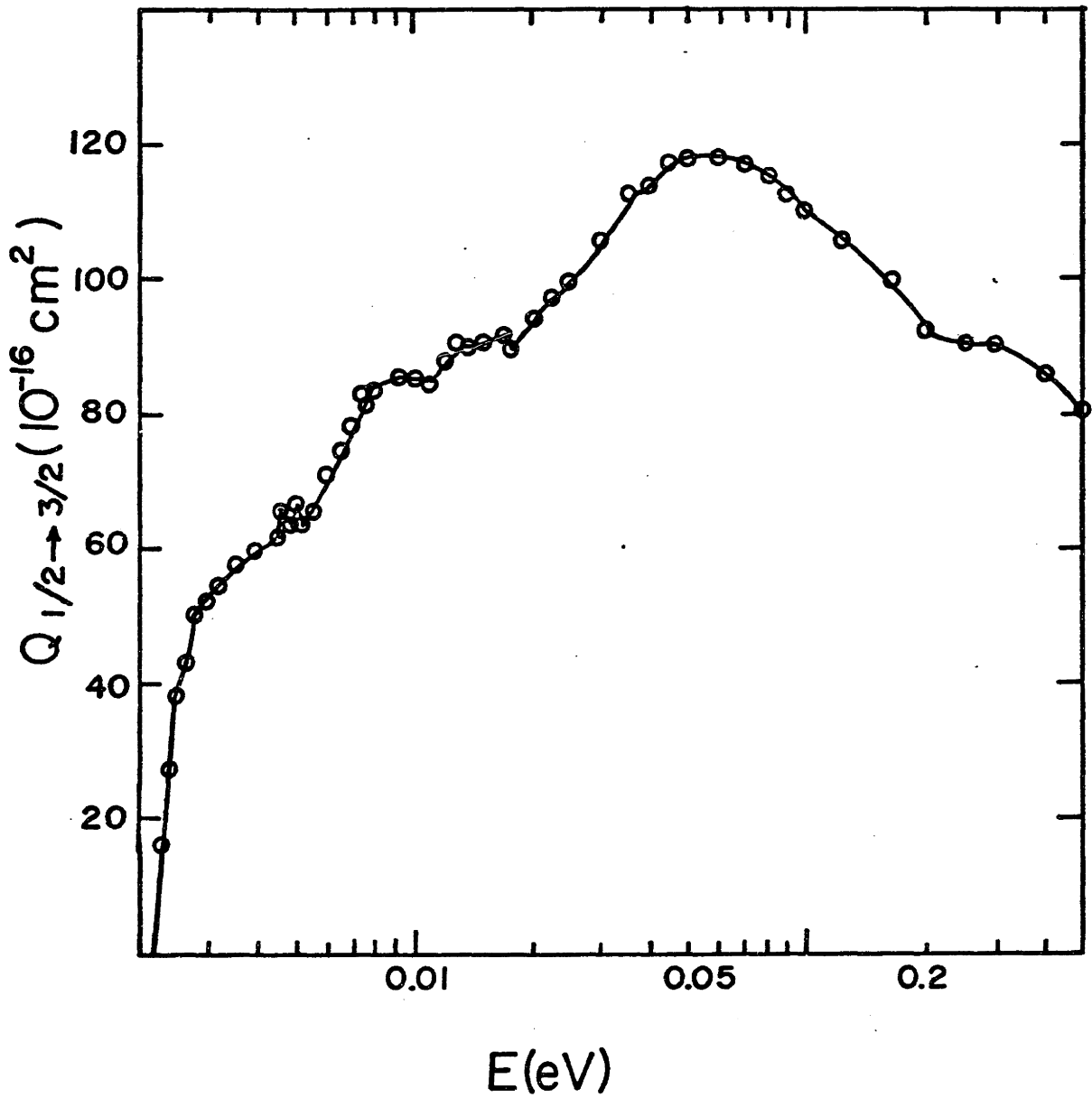
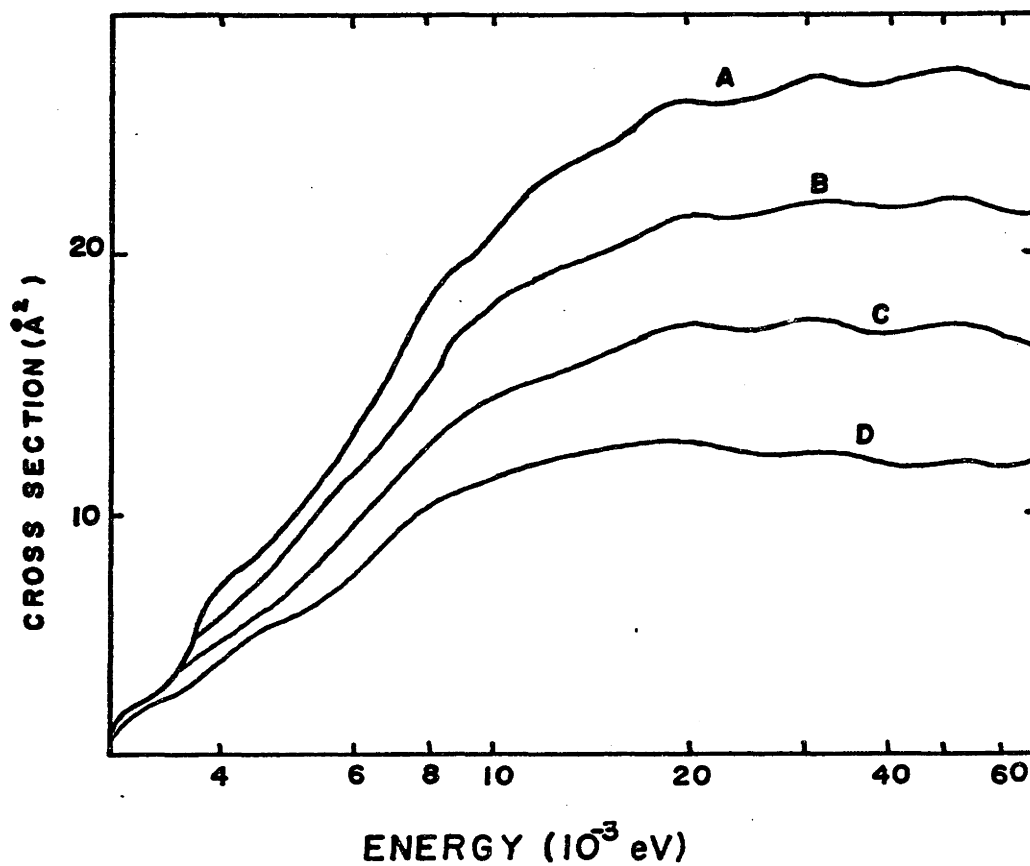


FIG. 7 Na-Ar CROSS SECTION



- A: $\sigma(3/2, 3/2 \rightleftharpoons 1/2, -1/2)$
 B: $\sigma(3/2, 1/2 \rightleftharpoons 1/2, -1/2)$
 C: $\sigma(3/2, 1/2 \rightleftharpoons 1/2, 1/2)$
 D: $\sigma(3/2, 3/2 \rightleftharpoons 1/2, 1/2)$

FIG. 8 Na-He PARTIAL CROSS SECTIONS

cross sections for Na-He. Both authors give some discussion of the relation between the cross sections and the potentials. The undulations of Fig. 8 as well as the low energy undulations of Fig. 7 are due to a region of stationary phase between the $A\Pi_{1/2}$ and $B\Sigma_{1/2}$ states at low impact parameters, according to Pascale and Olson. These authors also discuss the shapes of the cross section curves in terms of $\Delta V(R) = V(B\Sigma) - V(A\Pi)$. They find a correlation between the slope of ΔV in the region where $\Delta V \approx \Delta E$ and the rate of rise of the cross section from threshold. For Neon where the cross section rises most slowly, the slope of ΔV is smallest as ΔV approaches ΔE . This is the region where the semiclassical theories predict the major contribution from radial coupling.

Reid, who has used several different Lennard-Jones potentials as well as the Baylis potentials concludes that a rapid rise of the cross section at threshold is due to the potential being attractive down to small impact parameters, while a rise which is slower is due to a potential which becomes repulsive at larger impact parameters. All of these comments are qualitative in nature and Reid points out that one should not oversimplify the relation between the cross section and the potential.

An important feature of Fig. 8 is that the velocity dependence of the various $m_j \rightarrow m_j'$ cross sections are not radically different from each other and therefore from the averaged cross section.

II.5 Theory of the Experiment

The method for measuring the fine structure transfer cross section is to irradiate a Na beam with laser light at the $3S_{1/2} \rightarrow 3P_{3/2}$ wavelength, while the Na beam collides with a rare gas beam. The steady state fluorescence from the $3P_{3/2}$ and transferred fluorescence from the $3P_{1/2}$ state are both observed. The situation may be described as a 3 level problem, the rate equations for which are

$$N(3S_{1/2})^{\circ} = -N(3S_{1/2})R_{\text{ex}} + (N(3P_{1/2}) + N(3P_{3/2}))R_{\text{rad}} \quad (14a)$$

$$N(3P_{3/2})^{\circ} = N(3S_{1/2})R_{\text{ex}} - N(3P_{3/2})(R_{\text{rad}} + R_{\text{FSX}}) + N(3P_{1/2})R'_{\text{FSX}} \quad (14b)$$

$$N(3P_{1/2})^{\circ} = N(3P_{3/2})R_{\text{FSX}} - N(3P_{1/2})(R'_{\text{FSX}} + R_{\text{rad}}) \quad (14c)$$

where R_{ex} is the rate of excitation by the laser, R_{rad} is the radiative decay rate, assumed to be the same for both P states, R_{FSX} and R'_{FSX} are the $3/2 \rightarrow 1/2$ and $1/2 \rightarrow 3/2$ fine structure transfer rates. If we assume the R_{FSX} are small compared with the radiative rates, the steady state solutions to Eqs. (14b) and (14c) reduce to

$$N(3S_{1/2})R_{\text{ex}} = N(3P_{3/2})R_{\text{rad}} \quad (15a)$$

$$N(3P_{3/2})R_{\text{FSX}} = N(3P_{1/2})R_{\text{rad}} \quad (15b)$$

The ratio of photons emitted at the $3P_{1/2} \rightarrow 3S_{1/2}$ frequency to those emitted at the $3P_{3/2} \rightarrow 3S_{1/2}$ frequency is

$$R = \frac{N(3P_{1/2})R_{\text{rad}}}{N(3P_{3/2})R_{\text{rad}}} = \frac{N(3P_{3/2})R_{\text{FSX}}}{N(3P_{3/2})R_{\text{rad}}} = \frac{R_{\text{FSX}}}{R_{\text{rad}}} \quad (16)$$

Thus, the ratio of the transfer to fluorescence light give a quantity proportional to the rate of fine structure transitions. We know that

$$R_{\text{FSX}} = \sigma_{3/2 \rightarrow 1/2} n_{\text{r.g.}} v_{\text{rel}} \quad (17)$$

where σ is the cross section for the transition, n is the rare gas density and v_{rel} is the relative velocity. The object of the experiment is to vary v_{rel} while keeping n constant and measuring R . If we then divide R by v_{rel} we obtain a fraction proportional to $\sigma_{3/2 \rightarrow 1/2} (v_{\text{rel}})$.

The simple situation described by Eqs. (14) is complicated by the effects of hyperfine structure and magnetic sub-levels. We will show below that these complications do not seriously affect the interpretation of the results.

The energy level diagram for Na is shown in Fig. 9. One effect of hyperfine structure is to allow optical pumping which reduces the total number of atoms in the excited state at equilibrium. Suppose that the laser is tuned to the $3S_{1/2}, F = 2 \rightarrow 3P_{3/2}$ transition. In general the $3P$ level

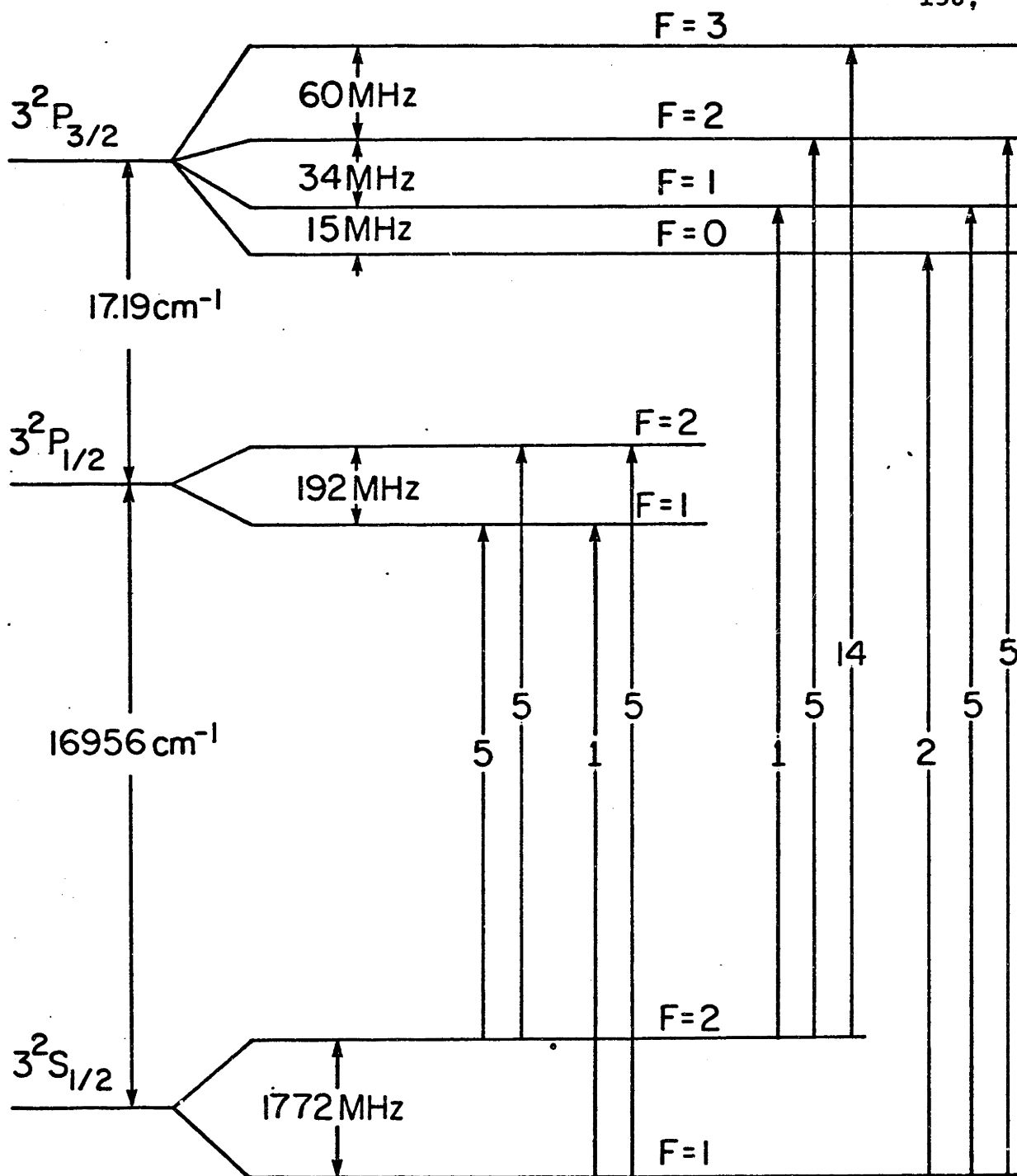


FIG. 9 SODIUM LEVEL DIAGRAM WITH
TRANSITION STRENGTHS

will decay to both ground state hyperfine levels, and atoms in the $F = 1$ state will not be excited. Eventually all the atoms will be in the $F = 1$ level and excitation will stop until fresh atoms enter the laser beam. A notable exception is the $3S_{1/2}, F = 2 \rightarrow 3P_{3/2}, F = 3$ excitation which can only decay to the $F = 2$ state due to selection rules. If this transition is excited, optical pumping to $F = 1$ can be avoided. In any case, the loss of excitation due to optical pumping is not a problem which affects the interpretation of the results.

The existence of magnetic sublevels brings up the question of the relation of the quantization axis relative to the collision axis. Recall that the calculations of the total cross section average the direction of the collision axis over all directions in space. While this is appropriate for collisions among atoms in thermal equilibrium it is not valid for a beam experiment. In particular, as the collision axis changes with respect to the quantization axis the cross section might appear to change due to purely geometric effects. We have sought to avoid this problem by establishing a quantization axis perpendicular to the collision plane. In this way the angle between the quantization axis and the collision axis remains fixed so that as the collision axis changes, any changes in the cross section which are observed are due to the velocity dependence of the cross section.

We establish this polarization axis in one of two ways:

either the laser beam is perpendicular to the collision plane and circularly polarized or nearly parallel to the plane and linearly polarized perpendicular to the plane. The former arrangement is used when velocities are to be selected by rotation of the beams and the latter when selection is by laser tuning and doppler shift. In both cases the collision axis changes as the velocity is changed. The collision axis goes almost full circle during a run when the beam is rotated while it changes by only 60° when doppler selection is used. Therefore, the axis problem is not as critical in the latter case.

Because circular polarization is used when the laser is perpendicular to the Na beam, a selective excitation of m_F states occurs. When the $F = 2 \rightarrow F = 3$ transition is being driven, most of the excited atoms will be in the $m_F = 3$ state. Since this is the "stretch" state with $m_j = m_I = 3/2$, the $m_j = 3/2$ state is selected. Referring to Fig. 8 we see that the fine structure transitions to $m_j = 1/2$ and $m_j = -1/2$ states will produce results very similar to what would be obtained if all m_j levels participated.

When linearly polarized light is used to excite the atoms, taking the quantization axis along the direction of polarization, only $\Delta m_F = 0$ transitions are induced, so a mixture of final m_F values, except $m_F = 3$, are excited. Furthermore, the hyperfine interaction mixes the m_j states to further reduce the m_j selectivity of the excitation. Therefore, we expect

that the observed cross sections will be good approximations to the total $j = 3/2 \rightarrow j = 1/2$ cross sections.

Note on eq. 10: The extreme low and high velocity limits of eq. 10 may be understood as follows: For low velocities the colliding atom will follow the solid adiabatic curve of fig. 2, both coming in and going out, so no state change occurs, as predicted by eq. 9. For high velocities, there is no time for the coupling which causes the avoidance of the crossing to be established, so coming in the atom follows the dotted, diabatic path, changing from one adiabatic curve to the other with high probability, again as predicted by eq. 9. Going out, the diabatic curve is again followed, so the atom is in the same state after the collision as when it started.

III. APPARATUS AND EXPERIMENTAL PROCEDURES

III. 1 Vacuum System

The vacuum system is shown schematically in fig. 10. It is a rectangular aluminum box, welded together from 1" thick Al plate. The approximate inside dimensions are 23" x 23" x 16" high. An $11\frac{1}{2}$ " hole in the bottom of the box leads to a Varian HS10 10 in. oil diffusion pump with a rated pumping speed of 4200 l/sec. One side of the box is completely removable. This side, the source flange, mates to a 6" diameter stainless steel elbow which in turn mates to a Varian M4 diffusion pump, pumping speed = 800 l/sec. The source flange supports the Na oven assembly. The inside of the box is divided into two regions by a differential vacuum wall of plexiglass and rubber sheet. The smaller source region is bounded by the source flange and is pumped by a 4" pump, while the larger scattering region is pumped by the 10" pump.

A $15\frac{3}{4}$ " hole in the top of the box is closed by an Al flange which supports the rare gas beam assembly. The remaining three sides of the box have 6" holes which are closed by flanges containing collection optics, observation windows, a vacuum gauge tube or a surface ionization detector.

The background pressure achievable in either region of the

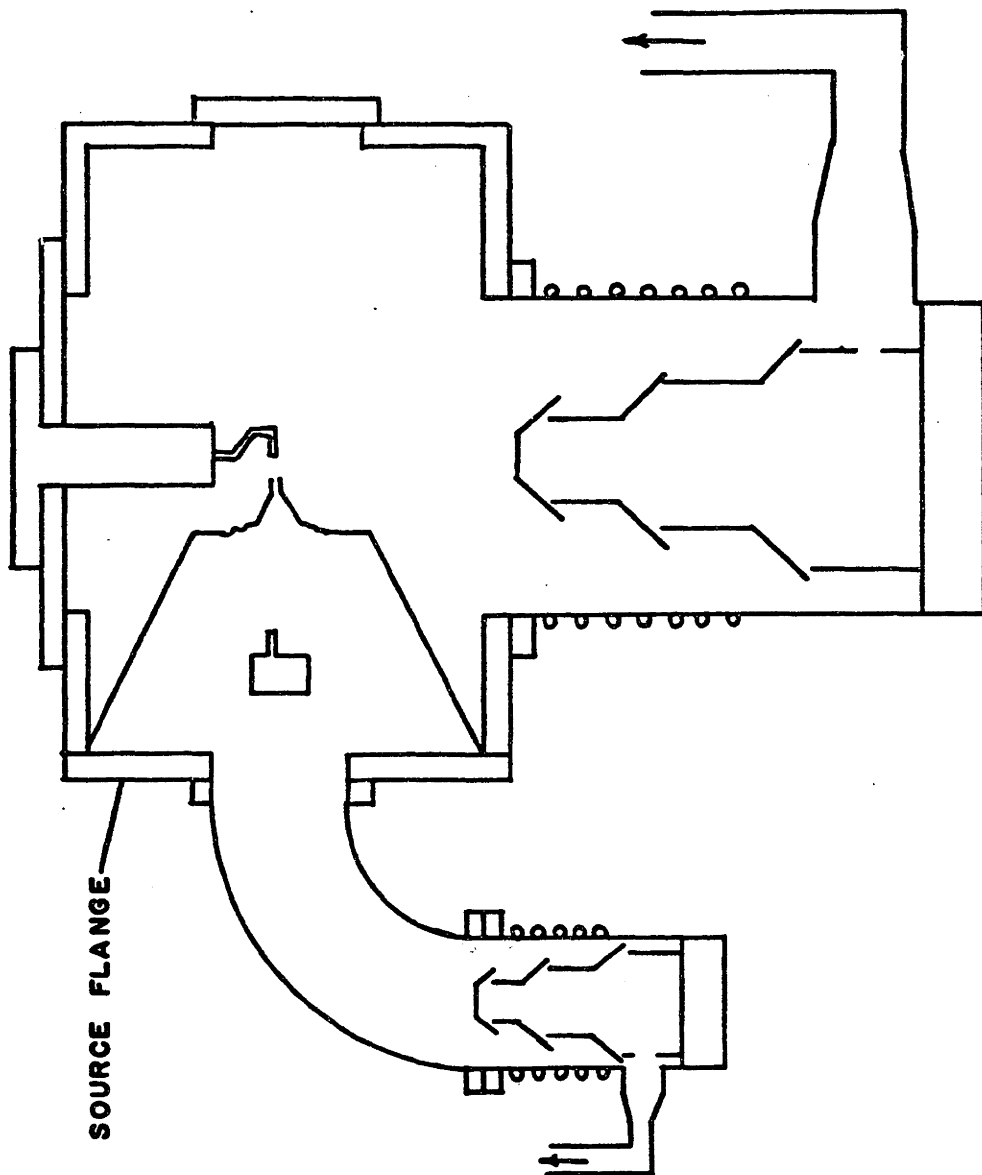


FIG. 10 VACUUM SYSTEM

box with no load is typically of the order of 10^{-6} torr. Ion gauges are provided for both regions. A thermocouple gauge monitors the pressure of the common foreline, which is pumped by a Welsh 1402 4 cfm two stage pump.

III. 2 Source Flange

The source flange supports all of the components of the sodium beam source. Most of these are shown in fig. 11. The uncollimated beam from the nozzle of the oven passes through a hole in the cold plate into the cone and through the needle to the interaction region. The nozzle may be aligned with the cold plate hole and needle which define the beam. The entire beam assembly may be aligned with the interaction region.

The oven is shown in detail in fig. 12. The oven body, top and nozzle are of stainless steel. The nozzle tube, with a .005" hole drilled in the end is welded to the body, and the top seals a copper gasket to the knife edge at the top of the body.

A molybdenum nozzle heater surrounds the end of the nozzle and is held in place with a steel set screw. The six holes which run the length of the heater house the heating elements which are close wound coils of .015" Tantalum wire. The coils do not short to each other because of the oxide layer which forms on the tantalum. The coils are enclosed in ceramic tubes which

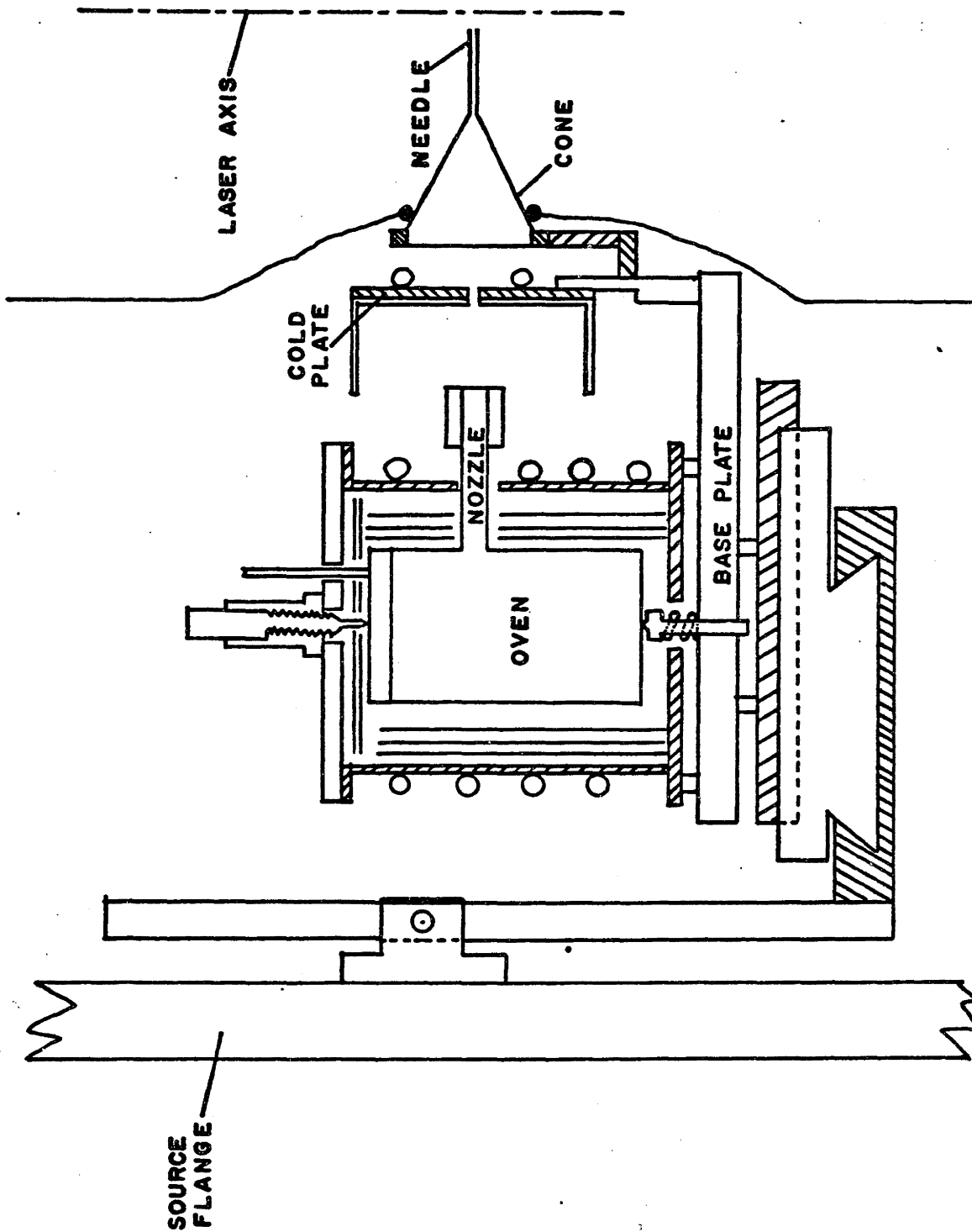


FIG. II Na SOURCE ASSY.

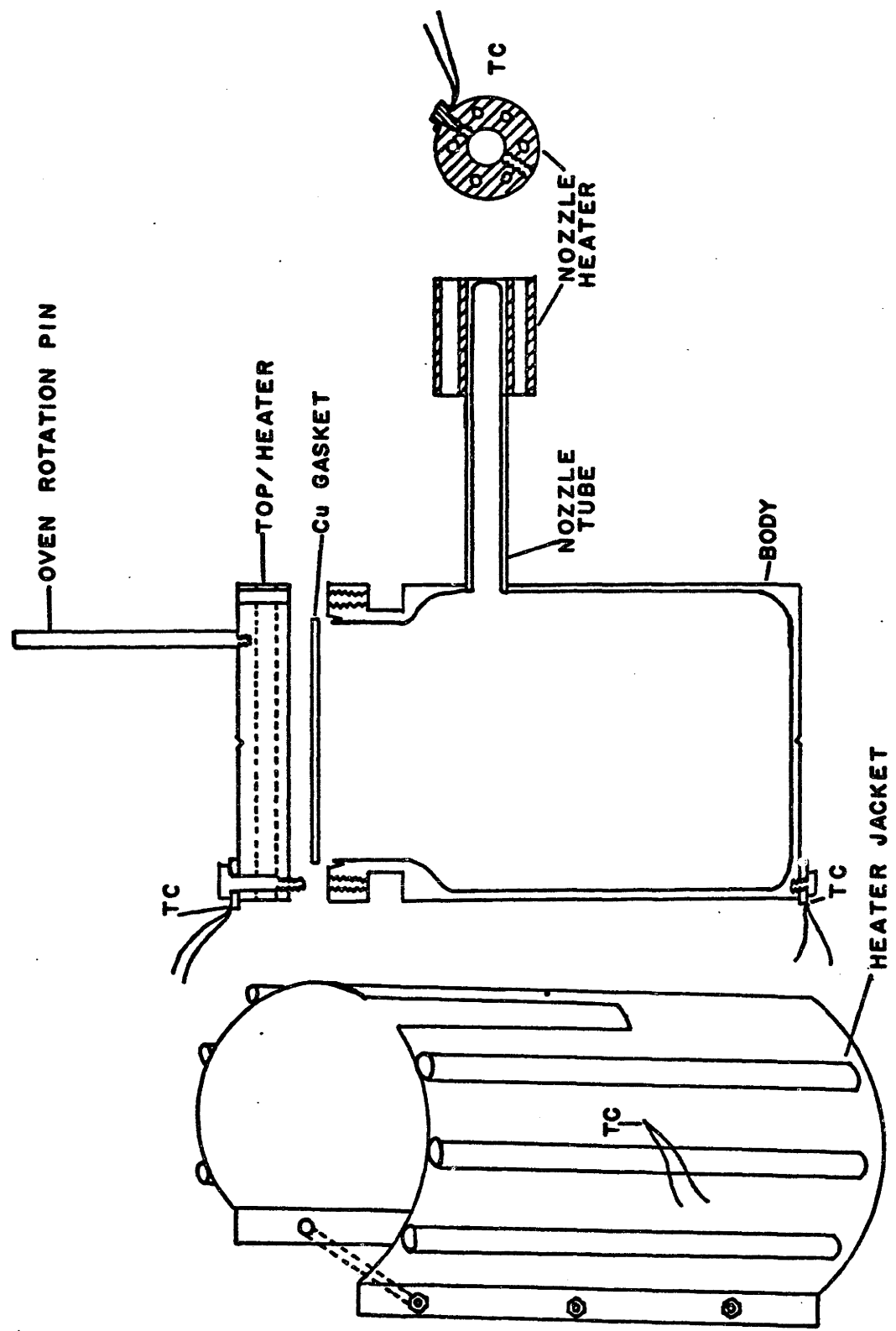


FIG. 12 OVEN ASSY.

insulate them from the molybdenum. All the heating elements are connected in series and are either welded to nickel leads or connected by crimping a copper-nickel tube around the junction. Similar heating elements are placed in the holes running through the top.

A stainless steel jacket holds the heaters for the oven body. Stainless tubes are oven brazed to a sheet of stainless which is formed into a cylinder that is fastened around the oven body. The tubes contain heating elements like those in the nozzle and top. Where necessary, wires are insulated or potted in place with Saureisen #1 cement, a high temperature ceramic.

Chromel-Alumel thermocouples are attached to the oven assembly at various points. One is welded directly to the heater jacket between heater tubes about half way up the jacket. The others are first welded to a stainless washer which is then bolted to the desired component. A thermocouple is attached to the top by one of the screws holding the top to the body. One is bolted to the bottom of the body and one is bolted to the nozzle heater. The washer of this last thermocouple is formed to make good contact with the curved surface of the heater.

Radiation shields made of .002" stainless foil are placed around the oven body, over the top and around the nozzle heater. The oven assembly is supported inside a copper can which is water

cooled. This prevents the heat from the oven from heating up the rest of the apparatus in the vacuum system.

The oven is held between two stainless pins so that it is free to rotate about the body axis (see fig. 11). The bottom pin is spring loaded so that turning the threaded top pin adjusts the height of the oven. The bearing surfaces on the oven are lubricated with Moly-Kote (molybdenum disulphide), a high temperature dry lubricant, to prevent seizing of the bearings when the oven is heated.

The mechanism for controlling the oven rotation is shown in fig. 13. The stainless steel pin shown in fig. 12 mounted on the oven top extends through the aluminum top flange of the cooled copper can. A spring holds the pin against the face of a threaded rod. Turning the rod moves the pin, rotating the oven about its pivot points.

The vertical motion and the oven rotation allow the nozzle hole to be lined up with the axis of the needle. A rough alignment is performed before the system is evacuated and fine adjustments are made with the beam on to maximize the sodium flux through the needle.

The $\frac{1}{8}$ " hole in the cold plate (see fig. 11) provides the first defining aperture for the Na beam. The plate is cooled by liquid nitrogen and is thermally insulated from the base plate with a stainless steel standoff. A 5 sided copper box is bolted

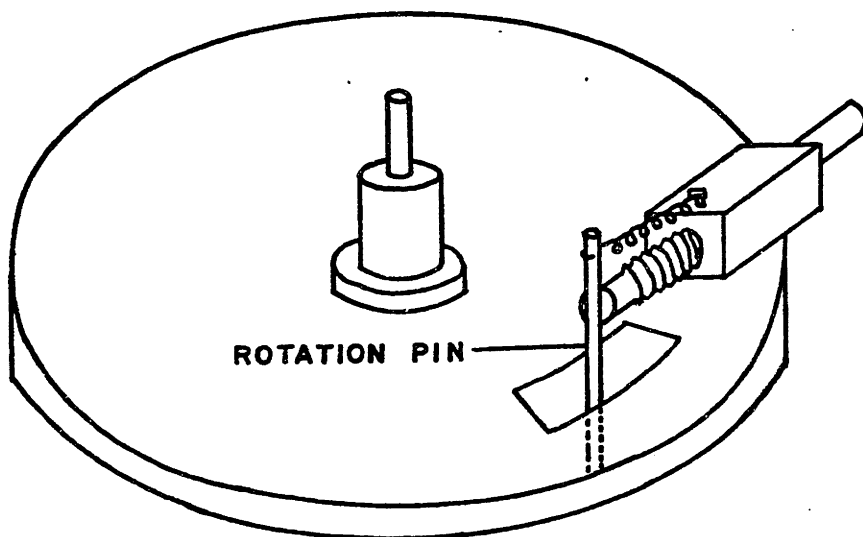


FIG. 13 OVEN ROTATION MECHANISM

to the plate, so that any line of sight from the nozzle that does not go along the beam axis is to a cold surface. The Na atoms have a high probability of sticking to the cold copper, so the box acts as an effective pump for the Na. When the beam is running the pressure in the source region can be reduced by about 2 orders of magnitude by cooling the cold plate with liquid nitrogen.

The purpose of the cone and needle (fig. 11) is to protect the Na beam from colliding with the atoms of the dense rare gas beam until they are in the interaction region. The cone is attached to the cold plate standoff so that the hole in the cold plate is on the axis of the needle. The cone is seated against an O-ring which is cemented to the rubber section of the differential vacuum wall, isolating the source region from the rest of the vacuum system except for the path through the needle. The cone is designed so that additional beam defining apertures can be placed in it, but this has not been done for any of the work reported here. The needle itself is the final defining aperture, and has an inside diameter of .060".

The entire source assembly consisting of oven, cold plate and cone is mounted on the base plate. This is bolted to a dovetail way which translates the source assembly along the beam axis. The way in turn is mounted on another way which translates horizontally, perpendicular to the beam axis. The

entire assembly is held in a carriage which pivots at a point near the source flange approximately on the beam axis.

A tilt of the carriage has the effect of translating the end of the needle vertically with little change in the beam angle.

All five of the source motions which have been described - oven height and rotation plus three orthogonal source assembly motions - are driven from outside the vacuum box, being coupled with O-ring sealed feedthrus into the source region. Flexible shafts or universal joints are used in all cases except the source carriage tilt control. These controls allow the source to be aligned internally and for the beam to be directed to the interaction region.

III. 3 Rotating Beam Source

The rare gas source is fixed to a rotating mount so that the angle between the gas beam and the sodium beam may be changed. It is of paramount importance that as the rare gas beam rotates, the gas beam density at the interaction region does not change. This will be the case only if the interaction region is centered on and symmetric about the axis of rotation. We accomplish this by using the laser beam to define the interaction region. If the Na beam is larger than the laser beam and uniform across the laser beam diameter the distribution of excited Na atoms will be symmetric about the laser beam. Using a laser beam diameter

of about .040" accomplishes this since the Na beam diameter is about .060".

The problem remains of insuring that the laser beam is on the axis of rotation and that the axis is stable. The rotation must be free of wobble or translation of the axis. We have designed a mechanism to accomplish this to a precision which will limit errors in cross section measurement to 1%. This has meant tolerances of .001" and .1 milliradian. The rotating beam assembly is shown in fig. 14 . Except for those pieces noted below, the entire assembly is of stress relieved stainless steel.

The bearing plate is bolted to the top flange of the vacuum box (fig. 10). This plate contains a bronze bearing which bears against the tube and determines the center of rotation. It also contains a ball bearing race which supports the top plate. The bearing surfaces here define the axis of rotation, since the short bronze bearing does not define the angle of the axis or prevent wobble. The tube is brazed into the top plate and is machined to fit the bronze bearing. The tube makes a vacuum seal to the box top flange with an O-ring compressed by a conical groove in the bearing plate. A 6 inch diameter protractor with $\frac{1}{2}^{\circ}$ divisions is fixed to the top plate so the rotation angle may be measured.

The top plate insert is sealed to the top plate with an O-ring and contains various electrical and O-ring feedthrus.

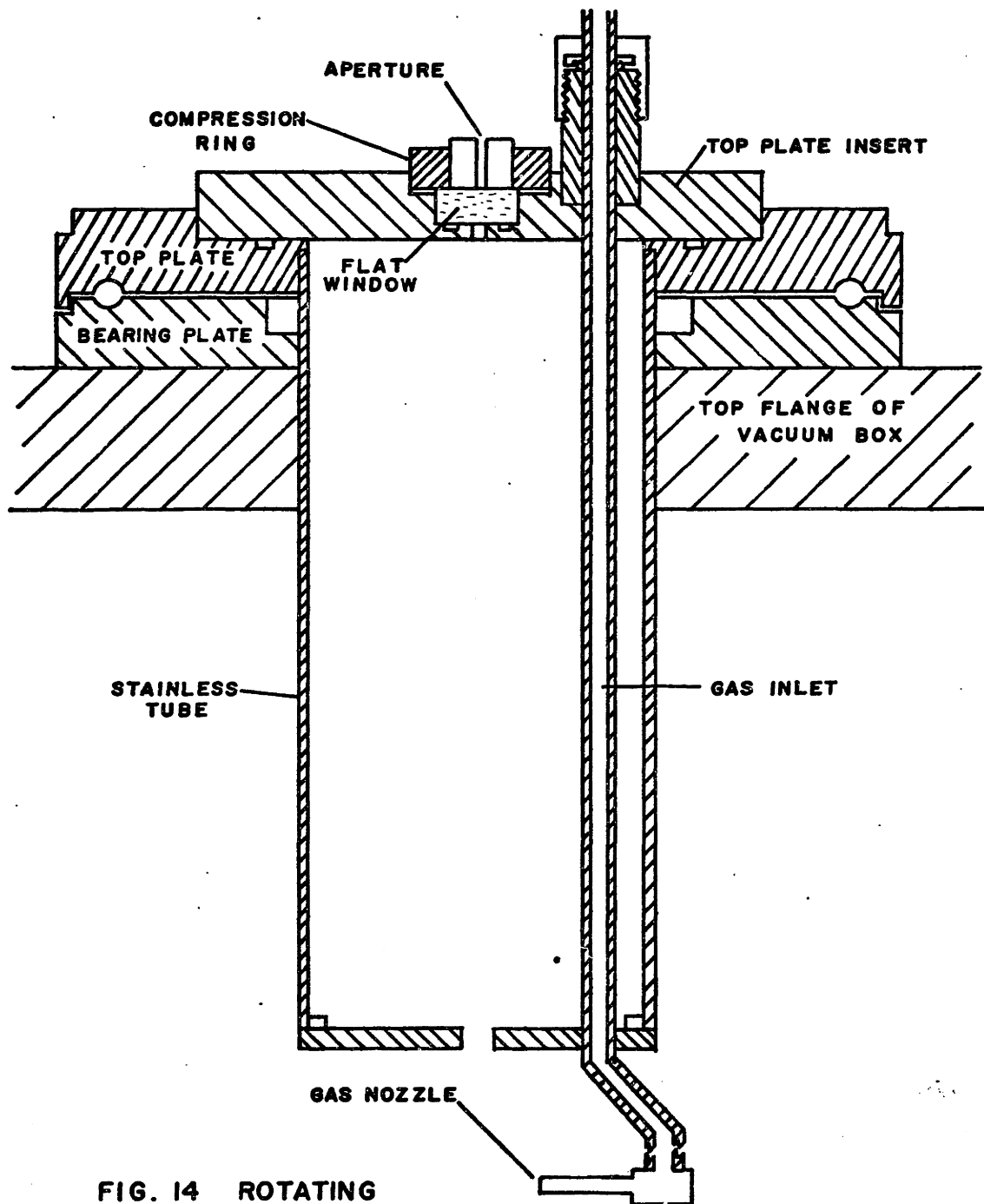


FIG. 14 ROTATING
BEAM

An optically flat window (cut from a piece flat to one wavelength in one inch) makes an O-ring seal to the insert plate, with compression provided by an aluminum compression ring. A teflon washer separates the window from the aluminum ring to prevent excessive strain. A blackend brass aperture with .040" opening fits into the center of the compression ring and rests on the window. A ring brazed to the bottom of the tube allows a brass plate to be mounted so as to provide support at the bottom for the gas beam inlet tube.

Machining specifications were for all assembled pieces to be centered to .001" of the bronze bearing center, with ball bearing surfaces flat and parallel to the top plate surfaces to .0005" over a 5" diameter. Our measurements showed that these tolerances were not significantly exceeded. The entire assembly is turned by hand and moves smoothly as long as the system is under vacuum, providing enough force to keep the ball bearing surfaces pressed to the balls.

The rare gas is brought into the vacuum box by a copper tube which is sealed to the insert plate by an O-ring feedthru. This tube is secured at the bottom of the stainless tube with a nylon set screw. A Swagelock union couples it to the gas beam nozzle assembly which is shown in detail in fig. 15.

The molybdenum nozzle holder and the copper tube are oven brazed to the copper block which serves as a compact elbow. A

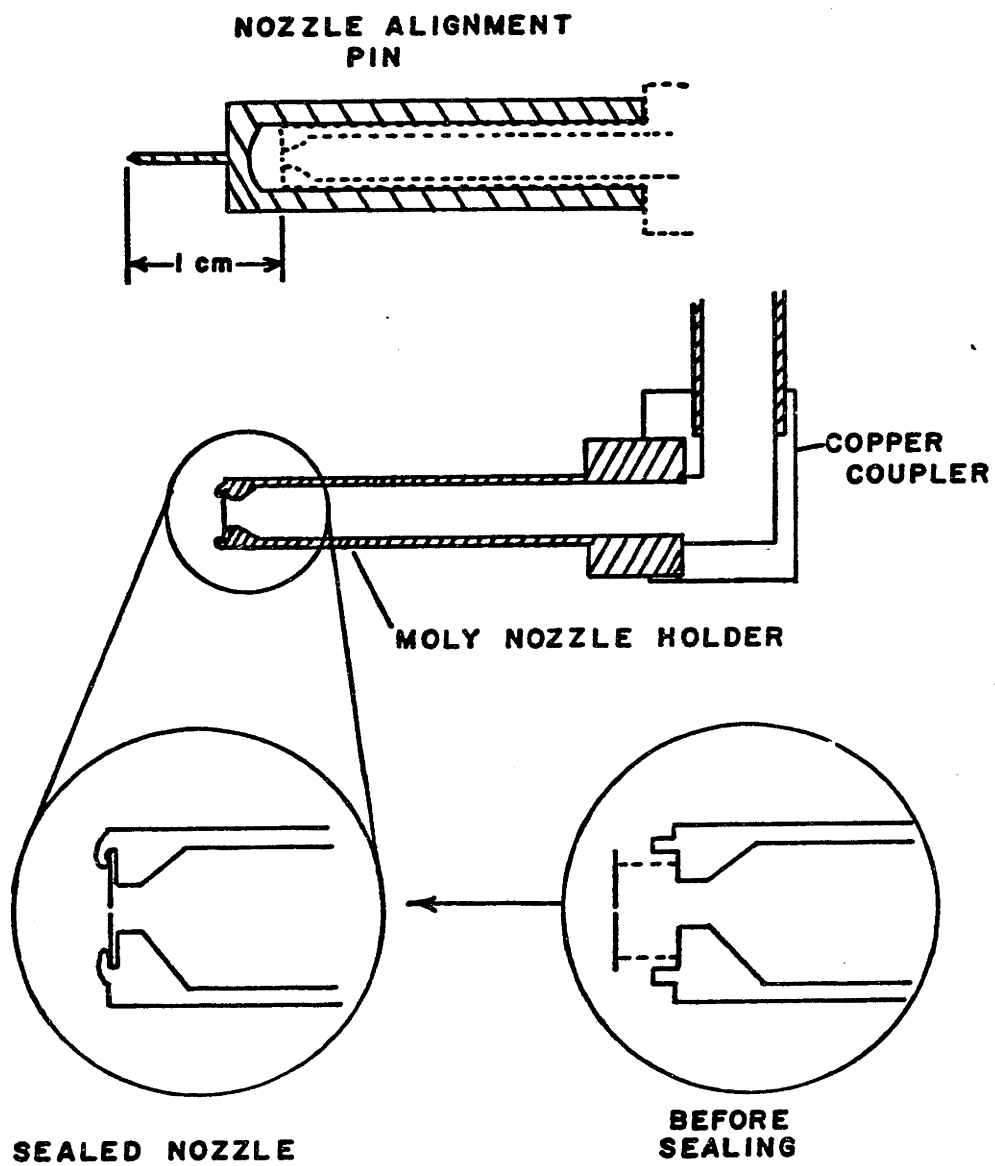


FIG. 15 GAS NOZZLE ASSY.

molybdenum microscope aperture, a .001" hole in a .001" thick foil, is sealed to the holder by rolling the protruding edge of the holder onto the foil.

The gas beam is positioned so that the nozzle is 1 cm. from the center of rotation, with the axis of the nozzle holder pointing at the center. The height is adjusted to be about level with the Na beam axis, with the final alignment being done using the Na beam controls.

III. 4 Laser and Input Optics

The laser used to excite the Na atoms to the $3P_{3/2}$ state is a Spectra Physics 580A single frequency tunable dye laser. The dye is a solution of Rhodamine 6 G in ethylene glycol obtained from Spectra Physics. The dye laser is pumped by a Spectra Physics Model 164-3 Argon ion laser. Typically 3-4 watts of Ar^+ power (all lines) are used to obtain a maximum of 100 MW single frequency dye laser output at the sodium resonance wavelength of $5890\overset{\circ}{\text{A}}$.

Fig. 16 shows a schematic diagram of the dye laser cavity. For the purposes of this work we will be interested in the operation of the electrically tunable elements. The tuning wedge and fine tuning etalon provide the coarse tuning. The intracavity etalon, with a free spectral range of 75 GHz is narrow enough to restrict lasing to a single longitudinal cavity mode. The cavity modes are spaced at 390 MHz. If the

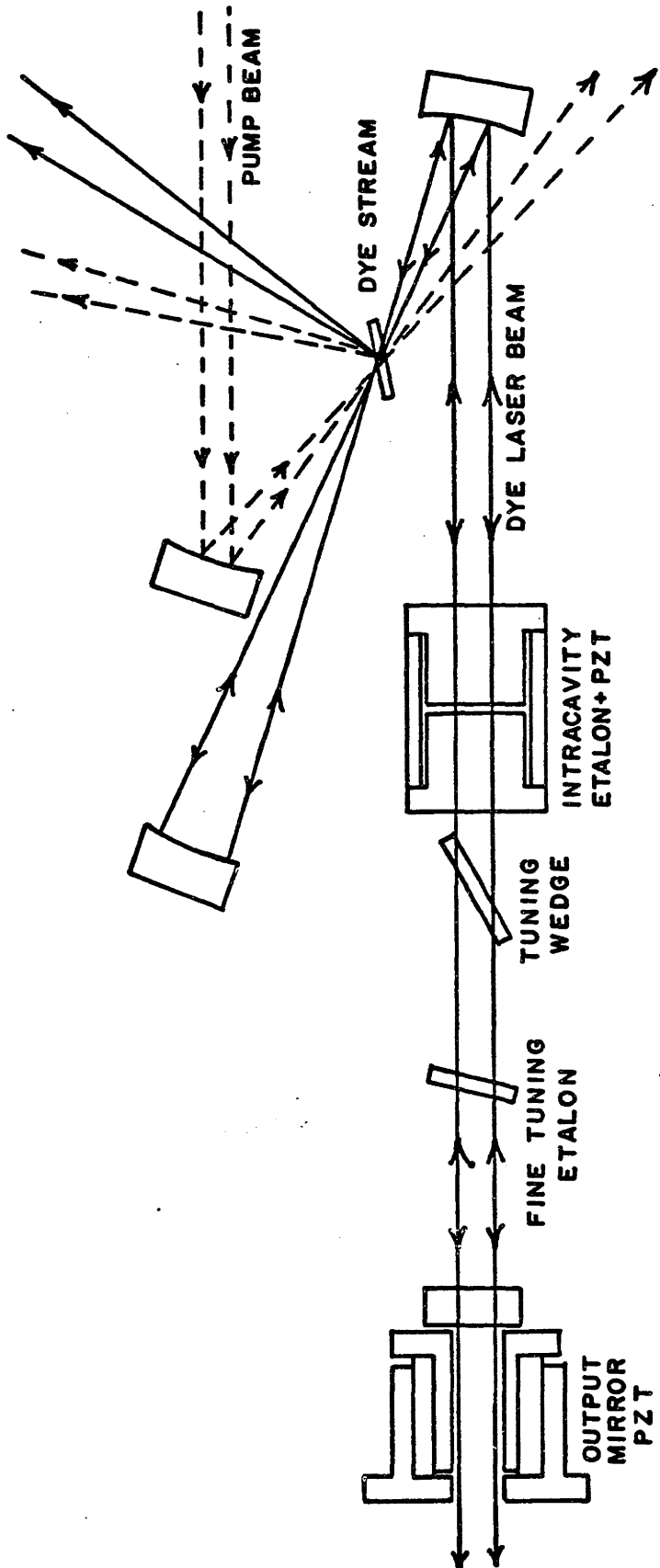


FIG. 16 DYE LASER INTERNAL OPTICS

spacing of the intracavity etalon is varied by changing the voltage on its piezoelectric transducer (PZT) the frequency of the laser initially remains constant, being determined by the cavity length, although the laser output power may change. As the etalon is tuned further, the laser will suddenly begin lasing at an adjacent cavity mode, closer to the new center frequency of the etalon. This procedure is called cavity mode hopping and provides a method for tuning the laser discretely in steps of 390 MHz. If the output mirror PZT is tuned while the intracavity etalon remains fixed, the laser frequency will change continuously until it goes outside the etalon range, when it will jump back discontinuously by 390 MHz. The laser's etalon controller provides means of achieving longer sweeps by changing the output mirror and etalon PZT's simultaneously.

Since the laser frequency is determined by the cavity length, any changes in the cavity result in frequency shifts. Enclosing the laser in a cardboard box minimizes frequency instabilities due to air currents. Also, the laser can be locked to an external etalon. The auxiliary optics used to do this as well as some optics which aid in tuning the laser are shown in fig. 17.

A portion of the laser beam is sent to a spectrum analyzer (Spectra Physics 470) enclosed in a temperature controlled box. The spectrum analyzer has a free spectral range (FSR) of 2 GHz.

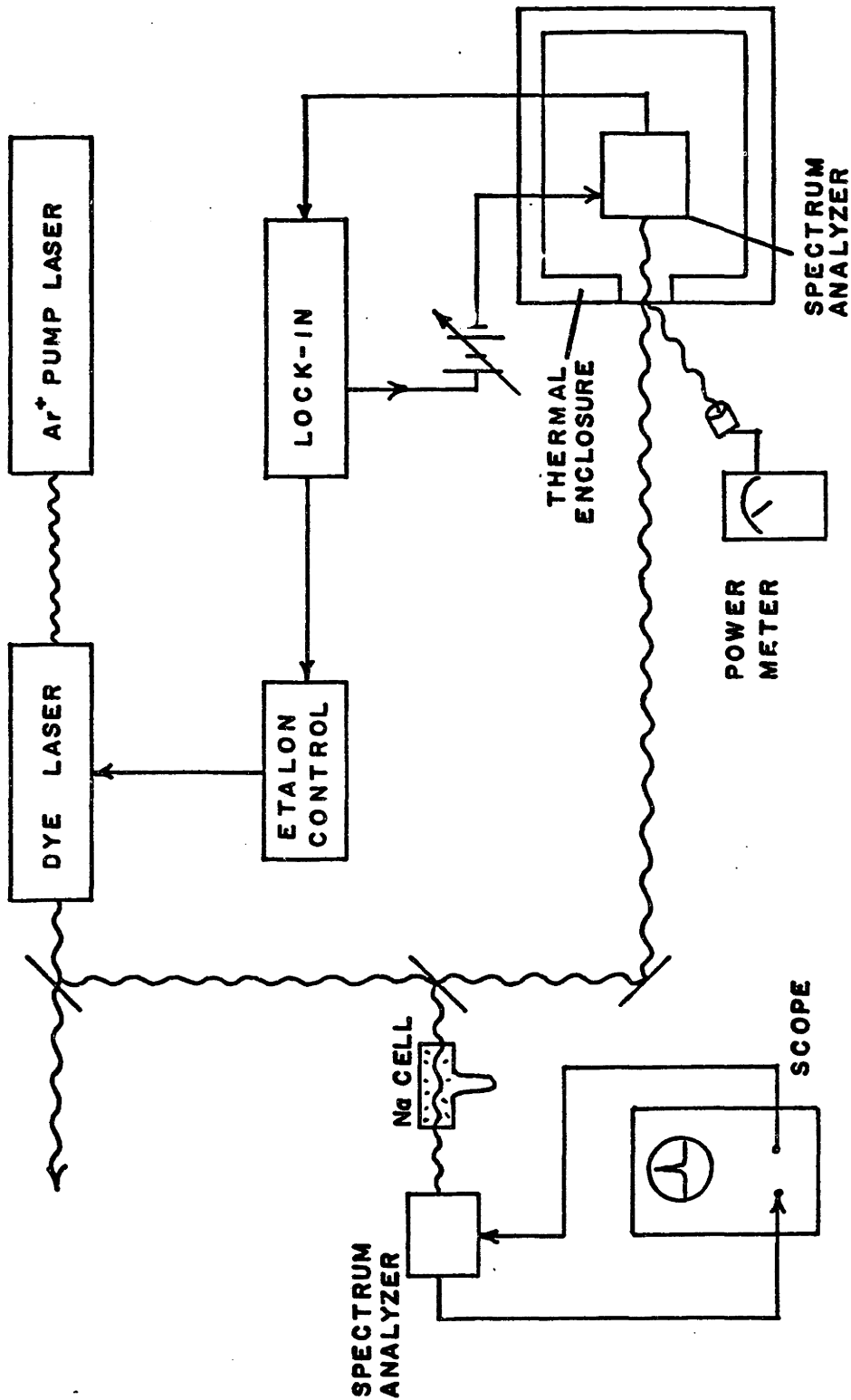


FIG. 17 AUXILIARY LASER OPTICS

A sine wave modulation at about 700 Hz is applied to the sweep input of the analyzer with a d.c. offset of 0-100V provided by a battery. When the laser frequency is in the pass band of the analyzer a modulated signal appears at the output which is sent to a lock-in amplifier (PAR JB-5). The d.c. output of the lock-in goes to the "cavity auxiliary input" of the etalon controller which applies a proportional voltage to the cavity PZT. This completes the servo loop and the laser frequency is locked to the spectrum analyzer, which can be tuned by changing the d.c. offset at the sweep input. Typical settings of the lock in amplifier are: mod level=0.5-1.0, sig. level=0.5-1.0 time constant=1sec, 6db/octave.

Another portion of the laser beam is sent through a sodium vapor cell to another spectrum analyzer (Spectra model 450, 2GHz or 470,8 GHz). This spectrum analyzer is swept by the horizontal scope drive and displays the mode structure of the laser. This is necessary to be sure the laser is operating at a single frequency and is also convenient for observing sweeps or mod hops. The Na cell is used to tune the laser to within the doppler width of the Na resonance frequency. Fluorescence in the cell, which is heated to about 60°C is clearly visible when the laser is at the correct frequency.

The light reflected from the window of the thermal enclosure is allowed to fall on a power meter (Spectra Model 404). This may be used for monitoring the power during data taking or for

maximizing the power when aligning the laser optics.

The optical system which directs the laser beam into and out of the scattering region is shown in fig. 18 . After passing through one of the beam splitters shown in fig. 17 (a glass microscope slide) the main part of the laser beam goes to a X10, focusable, beam expanding telescope. The telescope focuses the beam to its smallest diameter about at the interaction region. A mirror on the laser table directs the expanded beam to a mirror on the ceiling. The ceiling mirror sends the beam to the beamsplitter, a piece of optical glass flat to one wave in one inch. The reflected beam goes to the positioning mirror mounted on the top of the vacuum box at one corner. From there it is reflected to a mirror directly above the input window of the rotating beam mechanism (see fig. 14). This mirror, the perpendicular input mirror, directs the beam into the box along the beam rotation axis to where it intersects the Na beam at right angles. A mirror placed below the intersection point reflects the beam out of the box through a window in the flange opposite the source flange. The window is heated to keep it free of oil back streaming from the diffusion pump.

The portion of the laser beam transmitted by the beam splitter is reflected through this same window approximately parallel to the Na beam. It intersects the Na beam at about 7° , and strikes the blackened surface of the cone. This

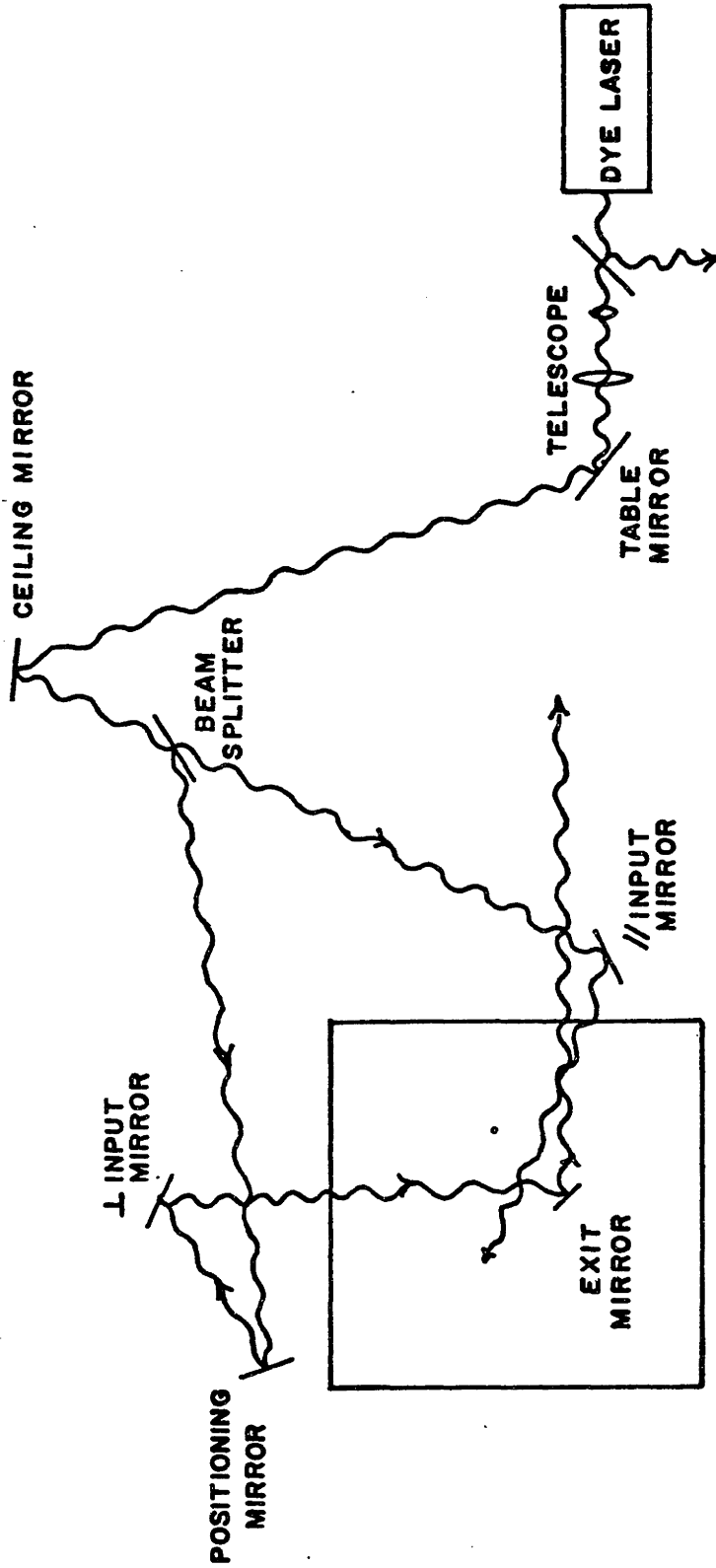


FIG. 18 LASER BEAM ALIGNMENT OPTICS

parallel beam is made to intersect the Na beam at the same point as the perpendicular beam. The perpendicular beam is used when the collision velocity is to be varied by rotation of the gas beam and the parallel beam is used for laser velocity selection.

As we have discussed above, the perpendicular beam must be along the axis of the rare gas beam rotation. If the beam enters the aperture (fig. 14), it intersects the axis since the aperture is centered. By observing the beam reflected from the window, the beam angle can be adjusted to be parallel to the rotation axis. The distances of the positioning mirror and the input mirror from the aperture and such that adjustment of the positioning mirror center the beam without affecting the angle seriously, while adjustments of the input mirror affect mainly the angle.

For most applications a circular polarizer is placed between the perpendicular input mirror and the aperture. The circular polarizer consists of a linear polarizer and a quarter wave plate in a mount which allows the two to be rotated with respect to each other and then to be locked and rotated together. The relative orientation is determined using the setup of fig. 19). The $\frac{\lambda}{4}$ plate is adjusted until there is no change at the detector when the analyzer is rotated. In practice, the adjustment can be made so that the peak to peak

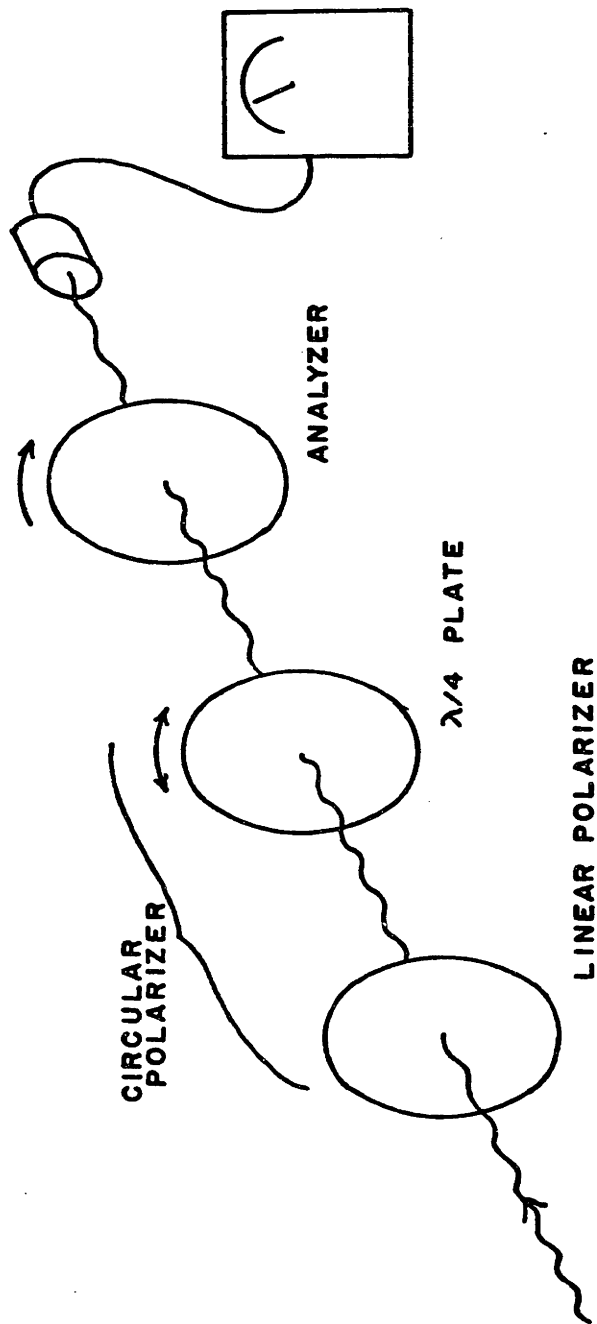


FIG.19 CIRCULAR POLARIZER ALIGNMENT

variation as the analyzer is rotated is less than 7%. This means the light is elliptically polarized with the squares of the major and minor axis of the \vec{E} vector ellipse differing by 7%.

The $\frac{\lambda}{4}$ plate of the circular polarizer is a piece of Polaroid retarder, with a nominal 140 nm retardation, sealed between two pieces of flat glass with clear epoxy. The linear polarizer is a piece of a glass sandwich polarizing filter used for photography.

Neutral density filters are sometimes used to attenuate the laser before sending it to the interaction region. These are made by cementing Kodak gelatin neutral density filters between flat glass with optical cement.

III. 5 Fluorescence Collection Optics

A schematic diagram of the optical system used for observing the resonance and transfer fluorescence is shown in fig. 20 . The collection lens, a 142 mm. focal length f/2.5 achromat is mounted in a steerable tube shown in detail in fig. 21 . The lens is vacuum sealed to its threaded cell with Torr-Seal. The cell screws into the stainless steel lens tube and the threads are sealed with Apiezon vacuum sealing wax. A sheet metal hood around the lens tube protects the lens from becoming fogged with oil backstreaming from the pump. The lens tube is

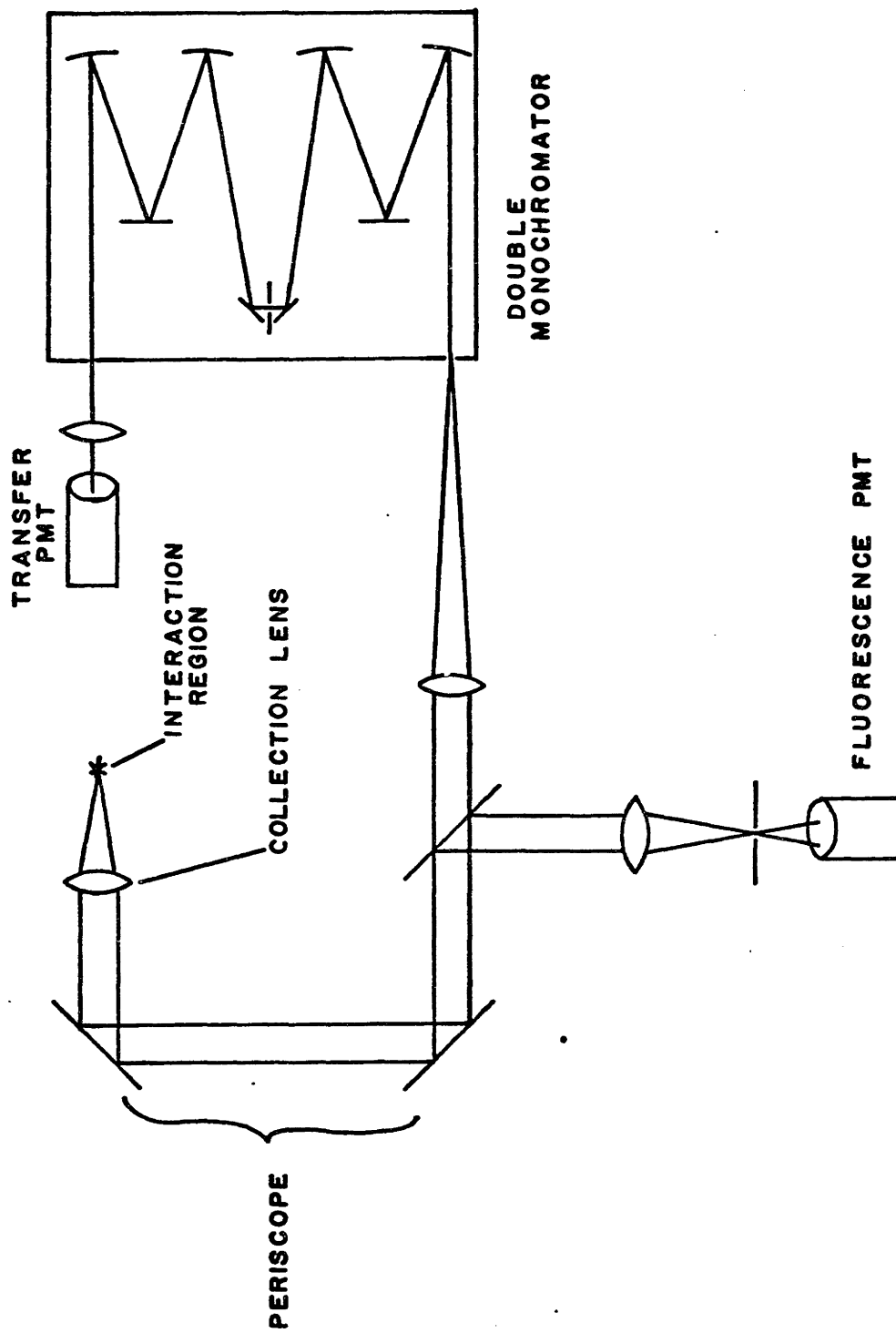


FIG. 20 COLLECTION OPTICS

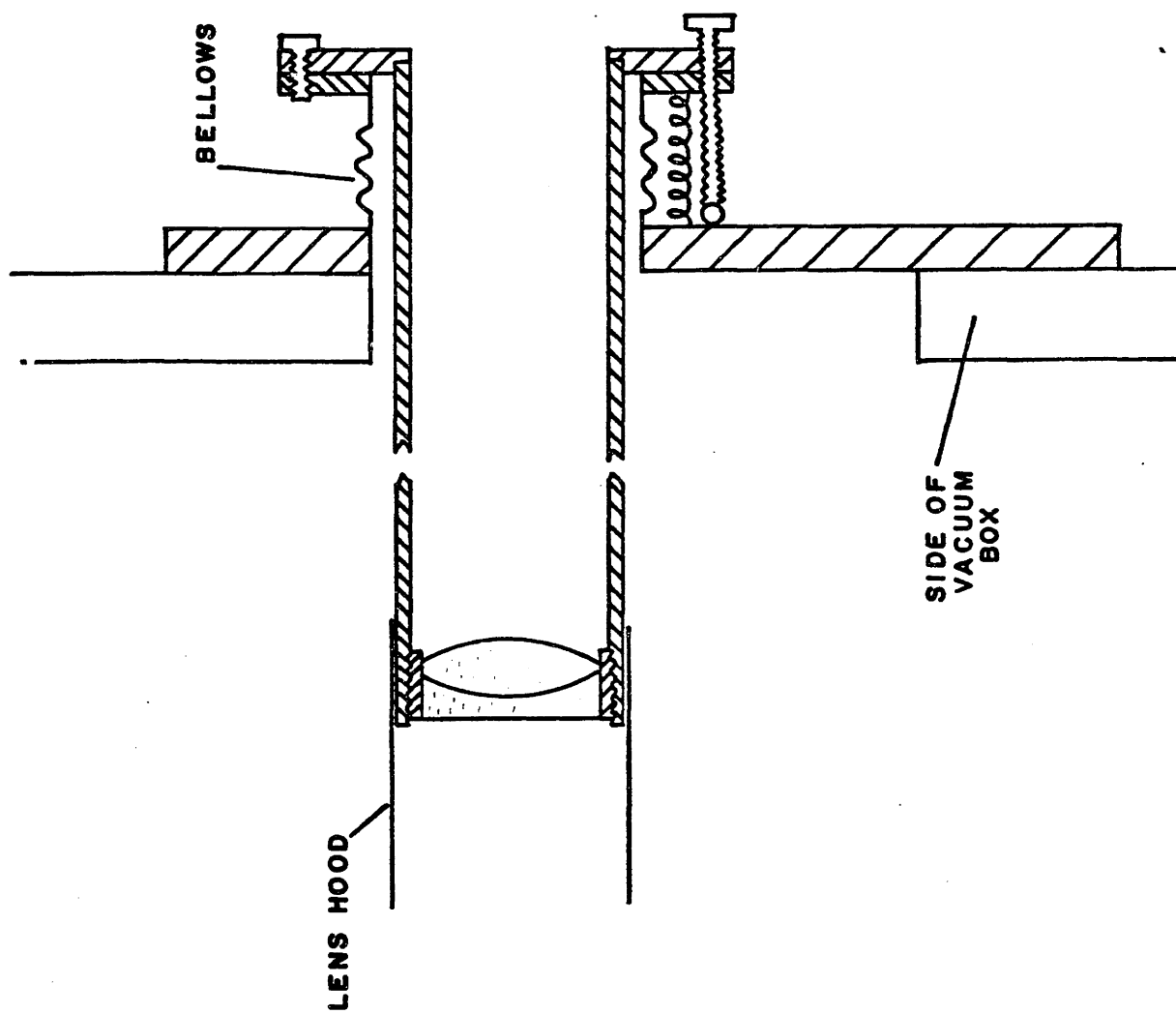


FIG. 21 COLLECTION LENS ASSY.

brazed to a flange which is bolted to a flanged bellows. The other flange of the bellows completes the vacuum seal to one of the box side ports. Three adjusting screws loaded by strong springs allow the tube to be tilted or moved in and out. Coarse focusing of the lens on the interaction region is performed by screwing the lens cell the proper distance into the tube before sealing with wax. Fine focusing is done with the adjusting screws. The lens is focused by observing an object placed at the interaction region through the lens with a telescope focussed on infinity.

The periscope of fig. 20 , shown in detail in fig. 22, was necessary to bring the collected light to the level of the monochromator slit. Two orthogonal adjustments are provided for each of the mirrors are worked from outside the periscope. The two sections are telescoping so the vertical distance between the mirrors is adjustable. The two sections can be rotated with respect to each other about a vertical axis. The flange of the top section mates with the collection lens tube flange.

The beam splitter, a flat piece of optical glass, is housed in a box (fig. 23) which mates to the lower periscope flange and to the fluorescence photo tube. The beam splitter itself is mounted atop a mirror mount so that the image of the interaction region formed by the focusing lens may be centered on the aperture. The adjusting screws are coupled to knobs out-

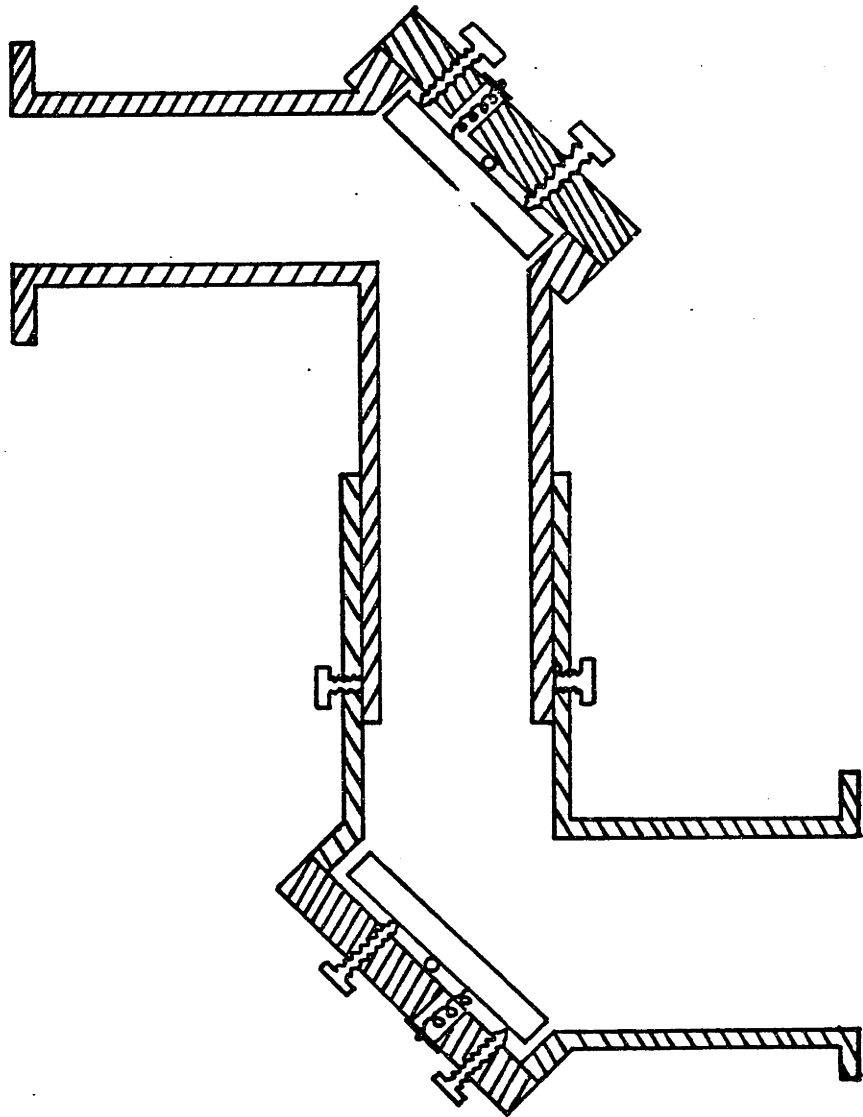


FIG. 22 PERISCOPE

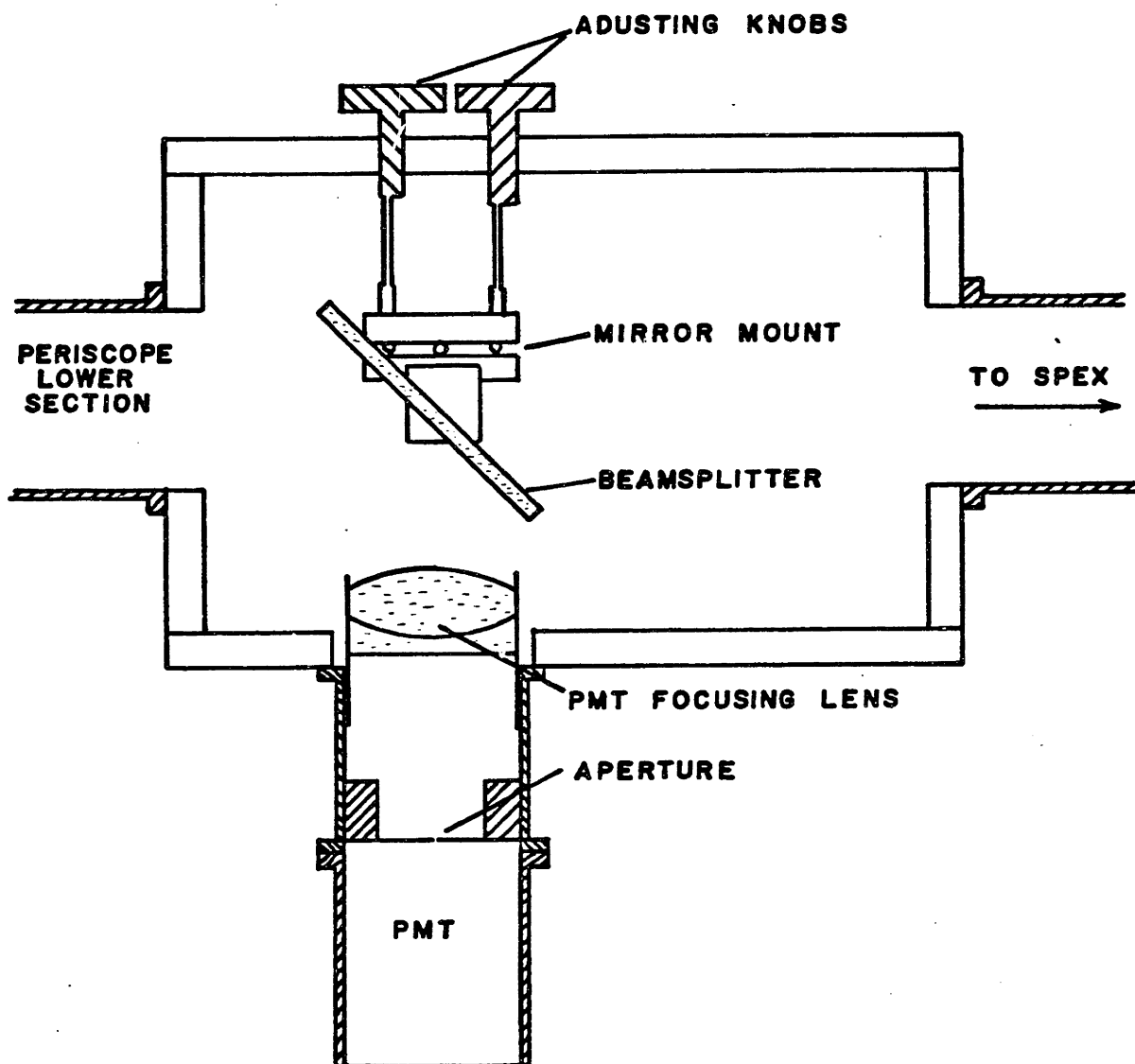


FIG. 23 BEAMSPLITTER

side the box. The photo tube, an RCA 6199 acts as the resonance fluorescence detector, since the majority of the light striking it is at the resonance fluorescence wavelength. The focusing lens is a 94 mm focal length achromat.

The monochromator, a Spex, Model 14018 with holographic gratings, 1800 lines/mm has an acceptance angle of $f/7.8$. For this reason, a 365 mm focal length lens is used to focus the interaction region onto the input slit, roughly matching the convergence of the light to the acceptance angle. With a 142 mm collection lens, the image of the interaction region at the slit will be about 2.6 times larger than actual size. Since the interaction region is about 1 mm. in diameter, some of the light is lost in passing through the monochromator slits all of which are set at .8 mm wide. The .8 mm wide slits provide attenuation of the fluorescence light by better than a factor of 10^5 when the monochromator is tuned 17 cm^{-1} away to the transfer fluorescence wavelength. Since the slits can be as high as desired without significantly affecting this attenuation, image is lost only in one direction due to the mismatch of collection lens and monochromator f /number. It should be noted that because of the periscope the image of the interaction region on the monochromator slit has the Na beam axis vertical, along the long axis of the slit. The short axis of the slit is along the rotation axis of the rare gas beam. This orientation

is important since the symmetry of the interaction region about the rotation axis must be determined by the accurately axial laser beam, not by the spectrometer slits, for accurate rotation data.

The photo tube on the output of the monochromator is an RCA C31034 in a Products for Research TE-104-RF refrigerated and r.f. shielded housing. No aperture other than the monochromator output slit is used.

The procedure for alignment of the collection optics is as follows: A small mirror is inserted near the monochromator input slit in the tube which holds the 365 mm focusing lens is removed and two cross hair mounts are installed near each end of the tube, defining the input axis of the monochromator. The mirror allows one to look back along this axis to the interaction region, which appears to be at infinity due to the collection lens. The monochromator position and the periscope height and angle are adjusted so that the axis is in the center of the lower periscope mirror. That mirror is adjusted to bring the center of the top mirror onto the axis. Finally, the top mirror is set to bring the interaction region on axis. After this is done, a ground glass is placed in the plane of the fluorescence PMT aperture, and the interaction region focused onto it by adjusting the focusing lens. Adjustment of the mount on which the beam splitter sits brings the image to the

aperture position. The cross-hairs and mirror are removed from the monochromator lens tube and the lens is reinstalled so that the slit is at its focus. Finer adjustments are made while observing actual fluorescence from the interaction region with the Na beam in operation.

III.6 Detection Electronics

In order to minimize the effects of instabilities in both resonance and transfer fluorescence signals it is important to observe the two simultaneously, so that the ratio will be unaffected. A block diagram of the detection circuitry designed to do this is shown in fig. 24 . The fluorescence PMT is an RCA 6199 run at a cathode to anode voltage of -1000V. The anode current is measured with a Keithly electrometer (model 600B or 601). The 0-1V recorder output goes to a voltage-to-frequency converter (Datel Systems VFV-10K) which has a 1KHz/volt conversion ratio. The output pulses of the V/F converter are counted by a gated scaler. The transfer PMT, an RCA C31034 run at -1500V cathode to anode feeds its anode pulses to a Mechtronics model 511 photon discriminator. The discriminator level is set so that the current measured by an electrometer for a given light level is consistent with the count rate for that light level, assuming the current gain given by the manufacturer as typical for the operating

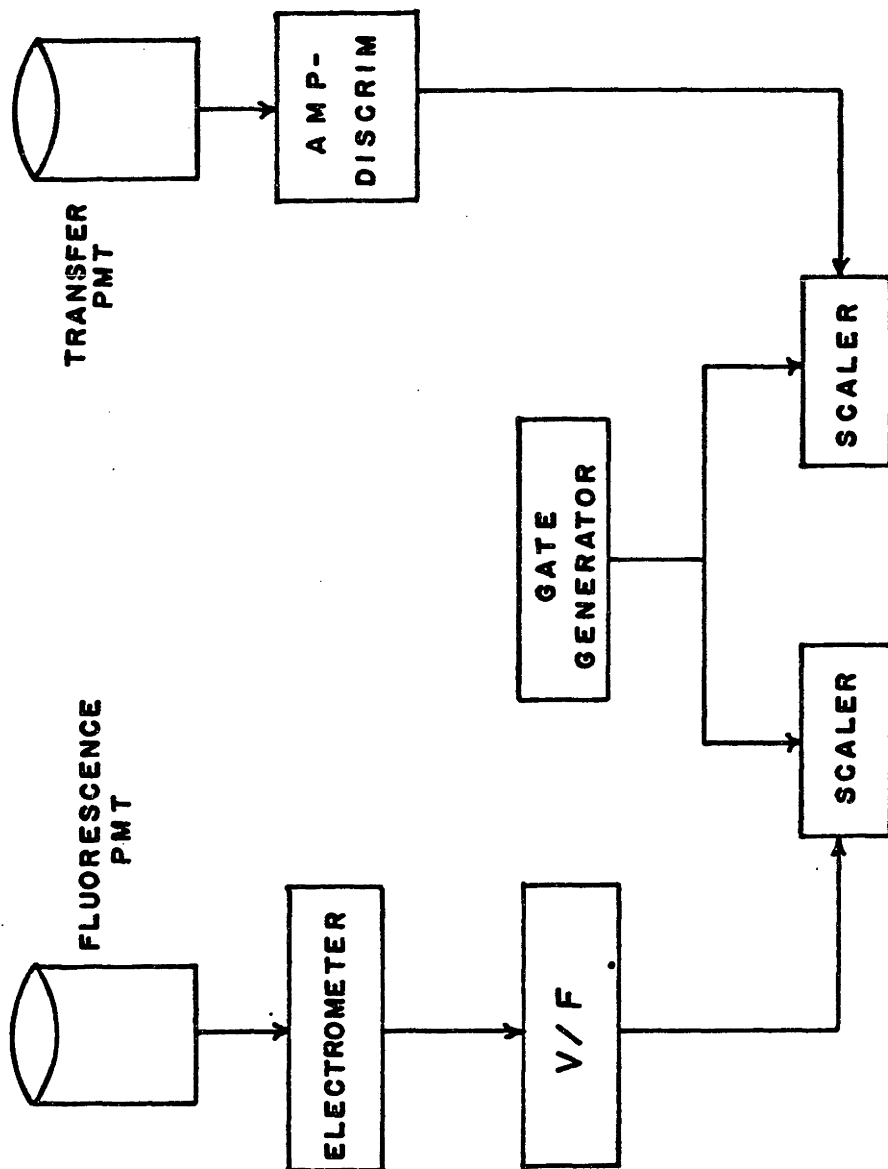


FIG. 24 DETECTION ELECTRONICS

voltage. The output pulses from the discriminator are counted by a gated scaler. The two scalers are gated together by an external gate generator. Gate times of 1, 10 and 100 sec. are available. Details of the homemade portions of the electronics are given in the appendix.

Earlier versions of the detection system used a digital voltmeter to read the electrometer output voltage. A time constant of 1 sec. was used on the output of the electrometer, and the DVM was triggered at the end of 1 sec of counting discriminator pulses. For 10 sec. counts, three DVM readings were taken. The V/F converter with simultaneous gating of counters has proved much more satisfactory, both in accuracy and convenience.

III.7 Procedures - Rotation Mode

The first step in a run where the collision velocity is to be varied by rotation of the rare gas beam is to align the laser along the rotation axis. In many cases when the rotation mode of measurement has been used the beam splitter of fig. 18 was not present and the ceiling mirror is adjusted so as to direct the laser to the positioning mirror. Under these circumstances it is easy to see the reflection of the laser beam from the window at the top of the rotating beam (fig. 14). Ideally, if the window was perfectly flat with its surface perpendicular to the axis of rotation, proper alignment would

consist of adjusting the mirrors until the laser was reflected back on itself. In practice the window is about a milliradian off, which could produce errors as large as 5% in the apparent cross section as the beam was rotated. Under these circumstances of misalignment of the window, the reflection of a properly aligned laser beam from the window will describe a circle about the incident laser beam. In order to observe this condition, a screen is set up on the laser table between the telescope and the table mirror (see fig. 18). A 1/2" hole in the screen allows the expanded laser beam to pass through, while the reflection of the laser beam from the window is visible on the screen when the alignment is close to being correct. The position of this reflection is recorded for each of four positions of the rotating beam, 90° apart. From these four positions, the center of the circle swept out by the reflection is determined and the input and positioning mirrors on the vacuum box are adjusted to bring the center into the laser beam axis. A few repetitions of this procedure generally produce a pattern that is centered within 1-2 mm. The optical distance between the screen and the window is about 8 m., so that taking into consideration the doubling of the angle on reflection, the error is about 0.1 milliradian. Once the proper alignment is established, the position of the spot reflected by the exit mirror is marked on a wall about 7 m. from the entrance window.

Deviations from the marked position of less than 1 mm. can be seen so .1 milliradian checking of the alignment is possible. Alignment checked in this way will be consistent with a rotation alignment for a period of at least several hours, but will generally not be good after a day so that a new rotation alignment is necessary each day.

Insertion of the circular polarizer between the input mirror and the input window generally alters the alignment. Since the circular polarizer blocks the reflection from the window quite effectively, it is difficult to repeat the rotation alignment. Instead, the spot reflected by the exit mirror is brought into coincidence with the position marked on the wall, and the alignment is almost as good as the original alignment.

An alternative procedure is to use an auxilliary laser such as a He-Ne laser to perform the rotation alignment and establish the position on the wall of the exit beam. The actual dye laser beam is then made to hit the same position. This procedure is especially useful when the beam splitter is in position since the reflection of the dye laser from the window in that case is more difficult to see and less distinct because of multiple reflections from the beam splitter. The multiple reflections from the input window have not proved to be a problem.

Proper alignment of the laser beam is a prerequisite for aligning the atomic beam. This procedure is performed when

the system is up to air.

With a proper laser axis established, the nozzle alignment pin (fig. 15) is slipped over the rare gas nozzle assembly. The pin is made so that the point of the alignment pin will be at the center of the laser beam when the rare gas beam is properly aligned. A telescope is set up to project the image of the pin reflected from the exit mirror onto a wall. The pin appears as a shadow in the laser beam. The rare gas nozzle is moved until the shadow of the pin point is at the center of the laser beam image. This alignment is not especially critical, but it assures maximum uniformity of the rare gas beam over the interaction region.

The rare gas beam and Na beam are set 180° from each other by lining up the needle of the Na beam with the rare gas alignment pin. Using a telescope with an eyepiece reticle to observe the pin and needle from below via the exit mirror, this can be done to better than $1/2^{\circ}$. The Na beam is moved laterally to intersect the interaction region. Vertical adjustment is made while looking through the collection lens. While final adjustments can be made later with the beam on, they are not generally needed after this procedure.

With the beams aligned, the system pumped down and the laser aligned along the rotation axis, we are ready for a Na beam. The oven body is typically heated to a temperature of

500°C, the top is kept about 50° hotter with the nozzle hotter still at 600-750°C. All of these temperatures are as read by the thermocouples, and so may be subject to some error. The body thermocouple in particular is not protected by a radiation shield and so may read lower than the actual temperature. A thermocouple on the heater jacket typically reads 70° hotter than the body, which is certainly an upper limit to the error in the body thermocouple.

With the Na beam on and the laser going into the box the laser is tuned to the Na $3S_{1/2}$, $F=2 \rightarrow 3P_{3/2}$, $F=3$ resonance. The easiest method is to first tune within the doppler width using the auxilliary Na cell, then observe the beam by eye through the collection lens (the upper periscope mirror is removed for this) while tuning the laser to maximize the fluorescence. Fluorescence due to excitation of $F=1$ ground state atoms is easily distinguished by its much smaller amplitude. The longitudinal position of the needle is set so that the end of the needle is about 3 mm. from the edge of the interaction region. The upper periscope mirror is replaced and the monochromator slit is opened slightly (about 20 μ wide and 1.2 mm. high) for observation of the resonance fluorescence through the monochromator. Final tuning of the laser is done while observing the fluorescence with the monochromator set to pass the fluorescent wavelength. The laser is then locked to the external etalon and the upper mirror of the

periscope adjusted to maximize the fluorescence signal on the PMT at the monochromator output. The image of the interaction region is then centered on the slit. The signal on the other (fluorescence) PMT is then maximized by adjusting the beam splitter. Adjustments of the oven and source alignment are made to maximize the signal. If any large changes are needed at any stage, the process is repeated.

The monochromator is then set 17 cm^{-1} away from the resonance fluorescence at the $3P_{1/2} \rightarrow 3S_{1/2}$ wavelength. The slit is opened to .8 mm. wide and .2 cm or 1 cm high. The monochromator phototube is connected to the amp/discriminator.

The rare gas beam is turned on to the desired pressure. He is run at about 6 psig., Ne at 15 psig. and Ar at 20 psig. The ratio of fluorescence to transfer observed through the monochromator is about 10^3 . When tuned to the transfer wavelength, the monochromator rejects the fluorescence by a factor of several times 10^5 . Thus the ratio of transfer signal to fluorescence background should be several hundred. We observe a "gas on" to "gas off" ratio of 300 in the signal from the transfer PMT, in agreement with this estimate.

The fluorescence and transfer signals are recorded for various angle settings of the rare gas beam. A typical run might start at the minimum angle of 35° , go to 60° and step through to 300° in 30° steps, then back from 315° to 45°

in 30° steps so a full sweep in 15° steps is taken. Data at 270° is not taken since the rare gas beam blocks the collection lens. Several readings are taken at each angle. Measurements of scattered light and background are taken at each angle by mistuning the laser from the Na resonance by a large amount (4 GHz). The effect of collisions with background rare gas rather than beam rare gas is determined later by shutting the beam off and leaking in rare gas through a variable leak so as to produce the same background pressure as when the beam was running.

The power of the laser is monitored throughout the run and the laser frequency is kept at the peak of the Na resonance by continually maximizing the fluorescence signal.

III.8 Procedures - Laser Velocity Selection Mode

The initial alignment procedures for runs where the collision velocity is to be selected by laser tuning is identical to that for rotation measurements. After all the optics and beams have been aligned relative to the perpendicular laser beam (the beam along the rotation axis) the parallel beam is introduced, almost along the Na axis. With this laser tuned so that this beam is exciting the maximum number of atoms as determined by the fluorescence signal, the position of the parallel laser beam is adjusted to give a maximum fluorescence signal. This maximizes overlap of the parallel beam with the

region that has been focused onto both photo tubes.

Since the fluorescence from the parallel beam is not confined to a small region as was that from the perpendicular beam, due to the small intersection angle between the laser and Na beams, the monochromator slit, rather than the laser beam is used to define the interaction region. A slit height of 1.2 mm. with .8 mm width is used with a corresponding opening in the aperture of the fluorescence PMT (smaller by the ratio of the focal lengths of the lenses used to image the interaction region). Since the rare gas beam is not to be rotated, it is no longer essential to have the interaction region centered about the rotation axis. The only requirement is spatial stability of the parallel laser beam and collection optics. Instabilities would result in changes of the gas density in the interaction region and variation in the relative collection efficiency of the fluorescence and transfer light.

An absolute frequency reference for the laser is established by tuning it so that the perpendicular beam is in resonance with the $3S_{1/2}, F=1 \rightarrow 3P_{3/2}$ transitions. By mode hopping from this frequency, the laser may be tuned to various frequencies whose difference from the $F=1$ resonance is known. Data is taken by hopping the desired number of modes to a laser frequency lower than the perpendicular $F=1$ frequency, blocking the perpendicular beam and recording fluorescence and transfer. Mode hops are

counted back to the $F=1$ resonance to verify that the proper frequency was reached, and the perpendicular beam is unblocked to check that the laser cavity did not drift. Counting of mode hops is facilitated by the use of the external 2 GHz FSR etalon, which is resonant with the laser about every 5 mode hops. The laser is of course not locked during this procedure.

Scattered light is checked by mode hopping in the opposite direction from the $F=1$ resonance. Some of the signal which is due to background Na is also checked in this way. Scattered light is more of a problem than in the rotation measurement, since the laser beam strikes the surface of the cone and scatters everywhere. This is one of the reasons for using small apertures. In order to avoid hitting the needle with the laser the needle is pulled back about 7 mm. from the interaction region. This increases the scattering from the rare gas before the Na gets to the interaction region, increasing the amount of background Na.

The useful range of laser tuning is about 2 to 15 mode hops to the low frequency side of the $F=1$ resonance. Several readings are taken at each frequency before rechecking the $F=1$ resonance. Stability of the position of the parallel laser is a major problem. Unfortunately we do not have a simple check on the laser alignment as in the case of the perpendicular beam. We deal with this problem by taking data at a particular frequency, then at a

reference frequency - usually the frequency where fluorescence is maximum. By normalizing all the data to the results at the reference frequency, slow drifts can be corrected.

The fluorescence signal as a function of laser frequency taken by itself gives the velocity distribution of the atoms in the Na beam. This information is useful for the interpretation of the data obtained in rotation runs.

IV. RESULTS AND ANALYSIS

IV.1 Methods of Analysis

The procedure for extracting a cross section curve from the data is basically the same whether the data comes from a rotation mode run or a laser selection run. The data consist of several pairs of fluorescence and transfer measurements for each angle or laser frequency corresponding to a given collision velocity. For each velocity there are also measurements of the background light signals due chiefly to laser scattered light and phototube dark counts. Finally, the contribution of the background rare gas to the transfer process is measured. In cases where background light signals are small or due only to phototube noise they are monitored less frequently. Similarly the contribution of background gas is not measured each time since it is usually only a few percent and the background pressure is quite constant from run to run for a given rare gas beam nozzle pressure.

Each fluorescence and transfer reading is corrected for background light before the transfer/fluorescence ratio is calculated for each pair. The ratios of all pairs taken at a given velocity are averaged. This average ratio is corrected

for background gas effects by subtracting the ratio, corrected for background light, obtained when only the background gas was present. If the background gas data comes from a different run, where a slightly different alignment of the collection optics might change the observed ratios by a constant factor, the background ratio is first normalized by dividing by that factor. The procedure is justified by the observation that in fact the factor is relatively constant - ratios from different runs which have very different magnitudes have the same velocity dependence. This procedure would not be valid if the difference in ratio were caused by the rare gas nozzle being at a different distance from the interaction region. This distance, however, is carefully set by procedures described earlier. In any case, the background gas contribution is only a few percent, so the errors introduced are not very important.

The corrected ratios represent the rate of fine structure transitions as a fraction of velocity. Dividing the rate by the velocity yields a number proportional to the cross section. The velocity is given by

$$v_{rel} = \sqrt{v_{Na}^2 + v_{rg}^2 - 2v_{Na}v_{rg}\cos\theta} \quad . \quad (18)$$

For rotation data v_{Na} and v_{rg} are constant while θ , the beam intersection angle, varies. v_{rg} is given by (AND65)

$$v_{rg} = \sqrt{\frac{5kT}{m}} \quad (19)$$

where T is the nozzle temperature, in this case room temperature. The use of Eq. (19) is justified because the gas beam is a jet with a high Mach number. We estimate an inverse Knudsen number for our beam in excess of 2000 (Knudsen number is the ratio of the kinetic mean free path in the nozzle to the nozzle diameter). Using the results given by Anderson and Fenn (AND65) this implies a Mach number of 25 and a velocity full width at half max (FWHM) of about 7%. This is in agreement with measured velocity widths by Lee and coworkers (SIS71, PAR72) of 6-8% FWHM with similar conditions.

The Na velocity is taken to be the most probably velocity as determined experimentally by the procedure described below. The velocity is between that predicted for a jet source (Eq. (19)) and that for an effusive source:

$$v_{eff} = \sqrt{\frac{3kT}{m}} \quad (20)$$

For laser velocity selection data, v is again given by (18) but θ is now a constant; v_{rg} is still given by (19), but v_{Na} is determined by the laser frequency. In order to understand this frequency selection let us refer to Fig. 25. The solid curve is the experimentally observed fluorescence excited by the parallel beam. As explained in Sec. III the laser fre-

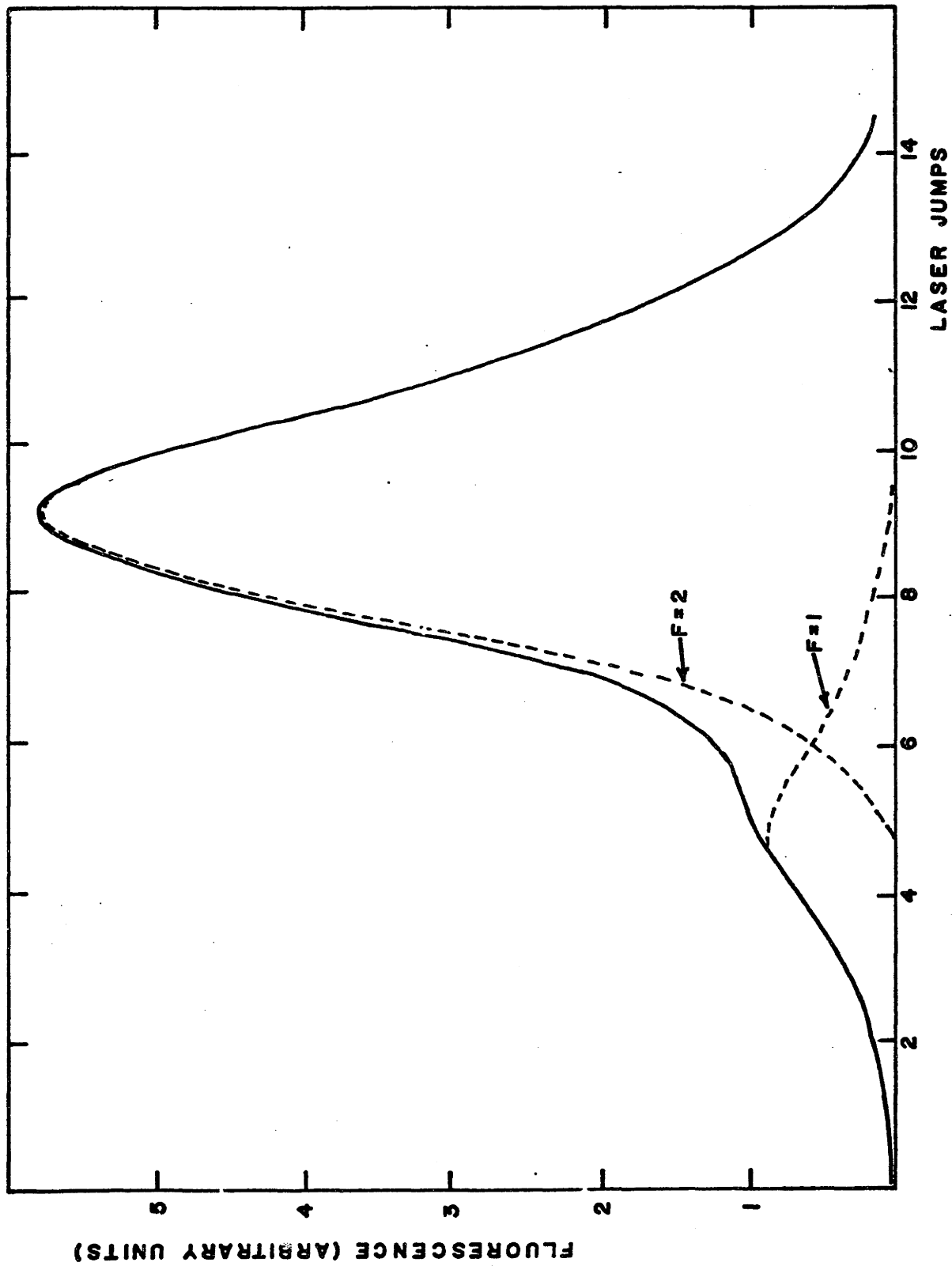


FIG. 25 Na VELOCITY DISTRIBUTION

quency is changed in jumps of 390 MHz with zero jumps being the frequency where the perpendicular laser beam is in resonance with the $3S_{1/2}$, $F = 1 \rightarrow 3P_{3/2}$ transition.

The solid curve of Fig. 25 is the sum of the dotted curves which arise from excitation from $3S_{1/2}$, $F = 1$ and $F = 2$. These curves reflect the velocity distribution of atoms in the beam projected on the laser axis. The shapes of the curves are identical and they are displaced from each other by the ground state hyperfine separation, 1772 MHz. These facts have been used to construct the dotted curves from the data.

The velocities of the atoms excited by a given laser frequency are given by first order doppler shift:

$$v_{F=1} = .230 \times 10^5 \text{ cm/sec} \times J \quad (21a)$$

$$v_{F=2} = .230 \times 10^5 \text{ cm/sec} \times J - 1.045 \times 10^5 \text{ cm/sec} \quad (21b)$$

where J is the number of laser mode jumps from the reference frequency.

It can be seen from Eqs. (21) or from Fig. 25 that after 4 jumps both $F = 1$ and $F = 2$ atoms can be excited simultaneously and that the velocities for the two types will be different by about 10^5 cm/sec. As a result, data taken in the overlap region of the curves must be corrected for the effects of atoms at one velocity if the cross section at the other velocity is to be determined. For example, with the laser tuned

to a given frequency the observed ratio of transfer to fluorescence will be

$$R \propto \frac{\sigma(v_{F=1}) v_{F=1} N(v_{F=1}) + \sigma(v_{F=2}) v_{F=2} N(v_{F=2})}{N(v_{F=1}) + N(v_{F=2})} \quad (22)$$

where $N(v_F)$ is the relative number of atoms with velocity v_F excited from the given F state. To evaluate this expression requires knowing the ratio of $\sigma(v_{F=1})$ to $\sigma(v_{F=2})$. A first approximation is to assume them to be equal, then to use the resulting $\sigma(v)$ curve to refine the correction. It is assumed that cross sections are the same for atoms excited from either $F = 1$ or 2 when the collision velocities are the same.

IV.2 Na-Ne Collisions

As we pointed out in Sec. II.4 the predicted behavior of $\sigma(v)$ for Na on Ne is anomalous compared to the other rare gases in that it rises much more slowly as the velocity increases, and has its maximum shifted to a much higher velocity. It is therefore of special interest to obtain an experimental $\sigma(v)$ curve to compare with theory.

We have made measurements in both laser selection and rotation modes of operation. The results of two laser selected runs, corrected as described in the previous section, are shown in Fig. 26, and compared with the theory of Pascale and Olson (PAS76). The uncertainties represent the standard deviation of points taken at a given velocity.

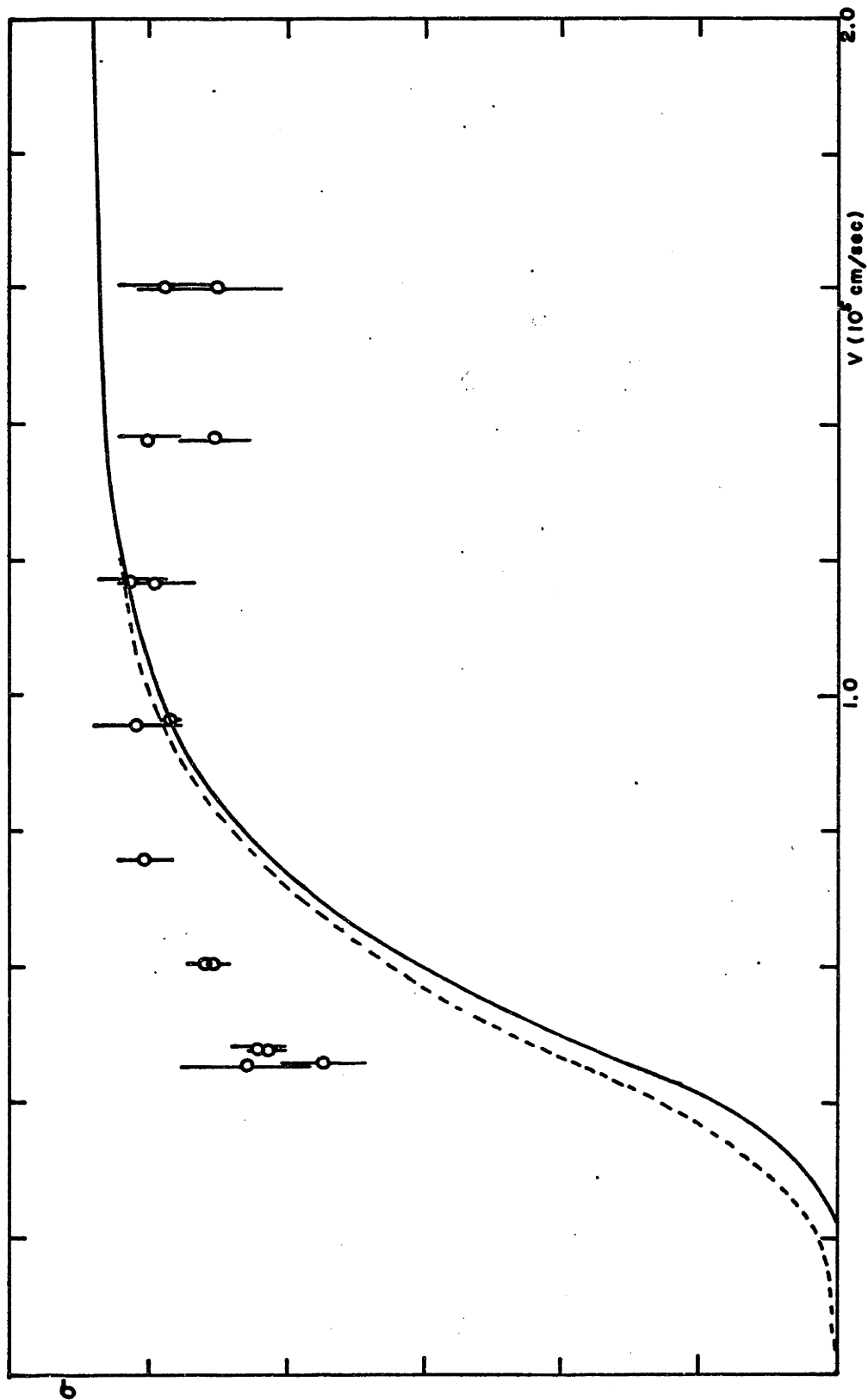


FIG. 26 Na-Ne CROSS SECTION, LASER SELECTED

The data result from laser frequencies 7 to 14 mode jumps from the reference frequency, and therefore represents atoms excited mainly from $F = 2$. At 14 jumps where the signal is smallest, background light (most dark current) corrections to the fluorescence were about equal to the signal, while at 9 jumps the correction was about 4%. In the transfer signal, the corrections were 30% and 4%. Corrections due to background gas were about 10% in overall magnitude, but only changed the shape of the curve by 5%, and do not change any important features. The corrections for the presence of $F = 1$ atoms are 32% at 7 jumps, 9% at 8 jumps and negligible for the rest. The corrections lower the cross sections since the $F = 1$ atoms are faster than the $F = 2$ atoms.

The observed cross section curve is normalized to agree with the theoretical curve at about 10^5 cm/sec. It is quite clear that the curves do not agree at all. The experimental curve has the cross section peaking in the vicinity of 1×10^5 cm/sec while the theoretical curve doesn't peak until 2×10^5 cm/sec. It is also clear that the experimental curve indicates a much more rapid rise at low velocity than the theoretical curve. Care must be taken in comparing the curves at very low velocities since the theoretical cross sections are for the $3P_{1/2} \rightarrow 3P_{3/2}$ transition, while the experiment is $3P_{3/2} \rightarrow 3P_{1/2}$. The relation between the two is given by detailed balance, with the result that the theoretical curve should be shifted down in

energy an amount equal to the fine structure separation which is equivalent to about $.2 \times 10^{-5}$ cm/sec.* The dotted curve shows the correction and it can be seen that it is not of much importance at our velocities.

The data of Fig. 26 were taken with the laser polarized perpendicular to the collision plane. Data taken with the laser polarized parallel to the collision plane do not exhibit any significant difference from these data, which is probably due to the fact that the collision axis does not change rapidly with respect to the polarization axis in this experiment, as discussed in Sec. II.5.

These data were taken with laser powers about equal to the saturation power - 30 mW/cm^2 . Some data were also taken with power 100 times as great. These show quite different behaviour as shown in Fig. 27. This data has not been corrected for the presence of $F = 1$ atoms, but this correction did not change the general character of the data taken at low power except for the lowest velocity point. The higher laser power makes the correction which is necessary much larger due to power broadening. In addition, the corrections cannot be made reliably since the assumptions which allowed the determination of the velocity distributions in Fig. 25 are no longer valid. For example, it is no longer true that at 4 jumps there are no $F = 2$ atoms excited. In addition there are considerably more

*See note at end of this section.

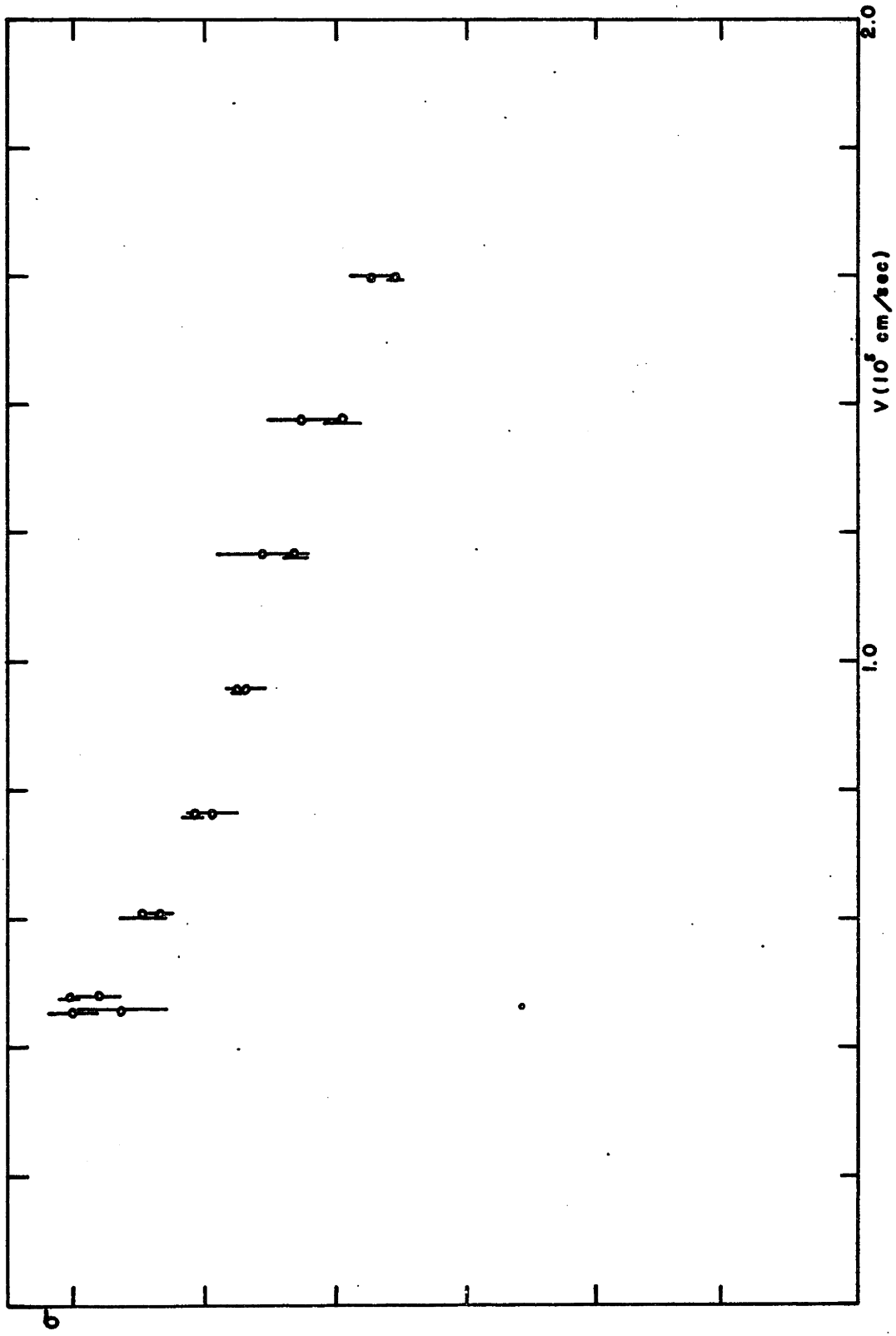


FIG. 27 Na-Ne CROSS SECTION, HIGH POWER

problems with background signals at high laser powers due both to increased scattered light and increased excitation of background Na atoms with random velocities. For these reasons we only consider data taken at low laser power to be reliable.

Fig. 28 shows the averaged results of 6 runs of rotation mode data separately normalized to their average value. The corrections for background light were less than 1%, with background gas corrections similar to those in the laser-selected data. The solid line is the theoretical prediction folded with the velocity resolution implied by a distribution like that of Fig. 25. This folding is necessary because of the relatively large spread of velocities involved in the collision in contrast to the situation when the laser is used to select velocities. With the theoretical curve normalized to agree with experiment at one point, we again see a clear disagreement.

It is also of interest to see how the data compare with laser-selected data. To make this comparison we drew a smooth curve through the laser selected data and folded it with the rotation mode velocity resolution. The comparison is shown in Fig. 29 with an uncertainty due to the uncertainty in the laser-selected data.

There is an apparent dip in the cross section derived from rotation mode data at about 1.4×10^5 cm/sec. It is our judgment that this is not real, but is due only to scatter.

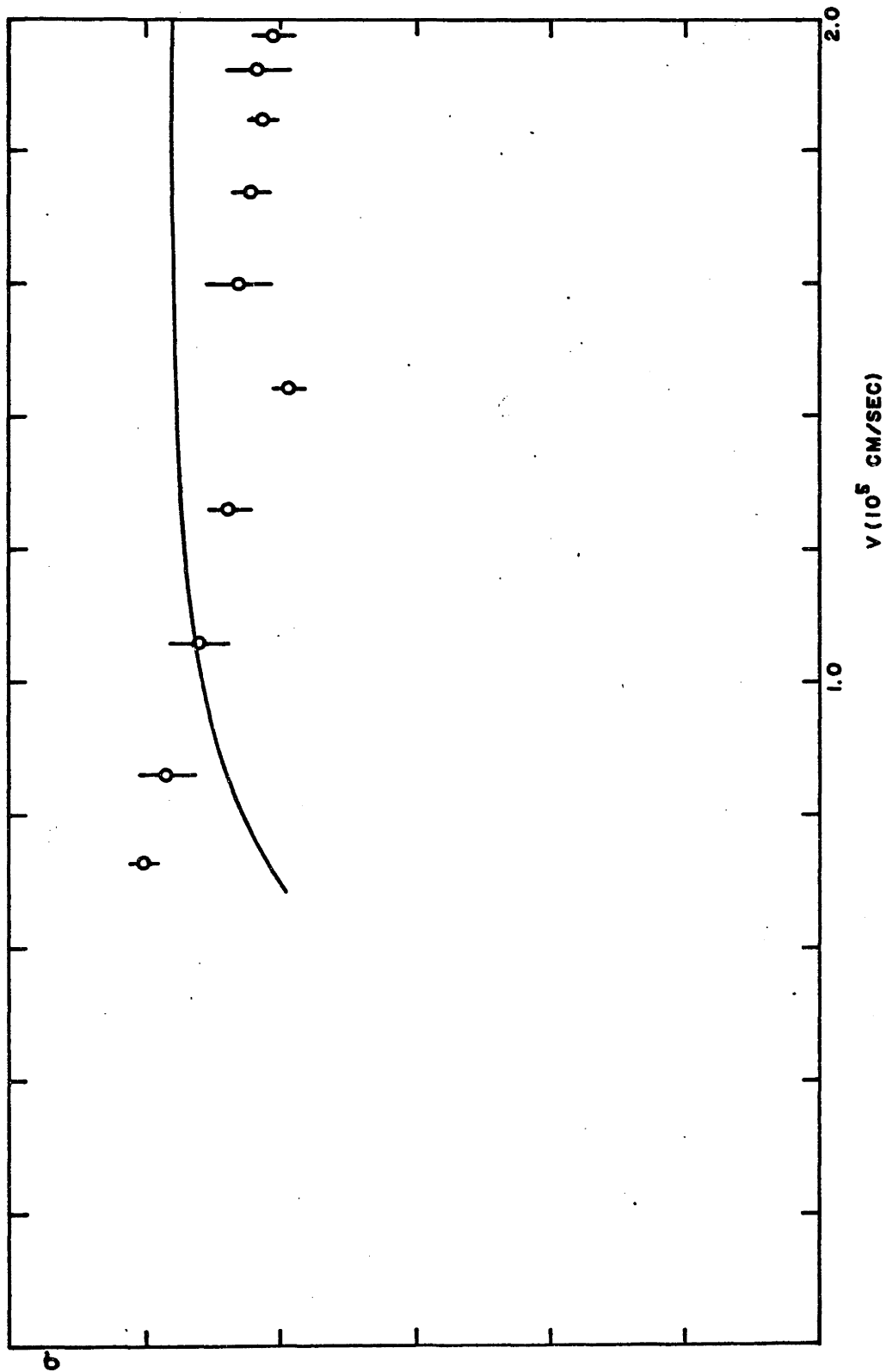


FIG. 28 Na-Ne CROSS SECTION, ROTATION SELECTED

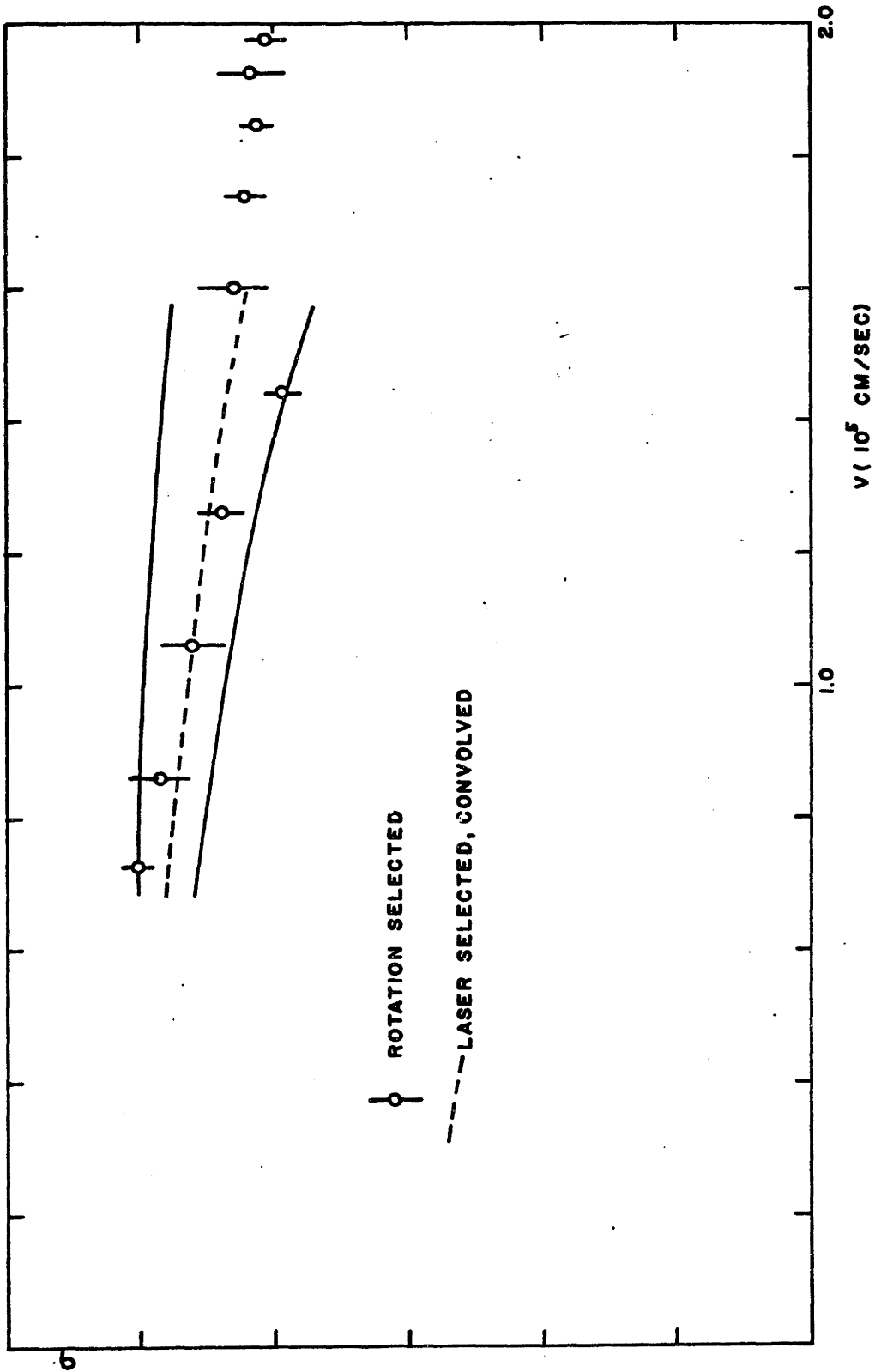


FIG. 29 Na-Ne CROSS SECTIONS

Given the velocity resolution of the rotation mode, the dip in the actual cross section would be much deeper and this is not supported by the laser-selected data. Unfortunately the laser-selected data is most uncertain just at this point, since the signal is very small for that velocity. It should be noted that the 1.4×10^5 cm/sec in rotation mode corresponds to an angle of 90° , so there is no corroborating data at 270° (since the gas beam nozzle blocks the lens), as for example there is between 60° and 300° . This point certainly deserves some more investigation.

Note: The correction to the theoretical curve shown in fig. 26 is in the energy, not the velocity, so it is $.2 \times 10^{-5}$ cm/sec only at zero velocity. There is an additional correction to the magnitude of the cross section equal to the ratio of the initial energies for the $3/2 \rightarrow 1/2$ process as compared to the $1/2 \rightarrow 3/2$ process. See for example, eq. 19 of REI73.

IV.3 Na-Ar Collisions

Fig. 30 shows three runs of laser velocity selected data for Na-Ar collisions. As for the Ne data, the laser was tuned from 7 to 14 jumps away from the reference frequency. Corrections applied are of the same general nature as with Ne, the only important correction to the shape of the curve being due to the $F = 1$ fast atoms. The correction is 59% at 7 jumps and 10% at 8 jumps. The magnitude of the correction at 7 jumps makes this point more uncertain, and the error bars have been adjusted accordingly. We assume the correction to be accurate to 15% of its magnitude.

The solid curve is the theoretical prediction of Pascale and Olson (PAS76). The experimental points are in substantial agreement with the theoretical curve, indicating a maximum at about $.8$ or $.9 \times 10^5$ cm/sec. The experimental cross section appears to fall off more rapidly to the low velocity side and less rapidly to the high velocity side; the predicted inflection of the cross section at $.4 \times 10^5$ cm/sec appears in the data as well. Such detailed comparison of theory and experiment, however, is probably not warranted at this time due to the uncertainties in the data.

Fig. 31 shows two runs of rotation mode data plus the theoretical prediction folded with the experimental velocity distribution. The agreement is excellent, and the statistics are good as well, which supports the agreement between theory

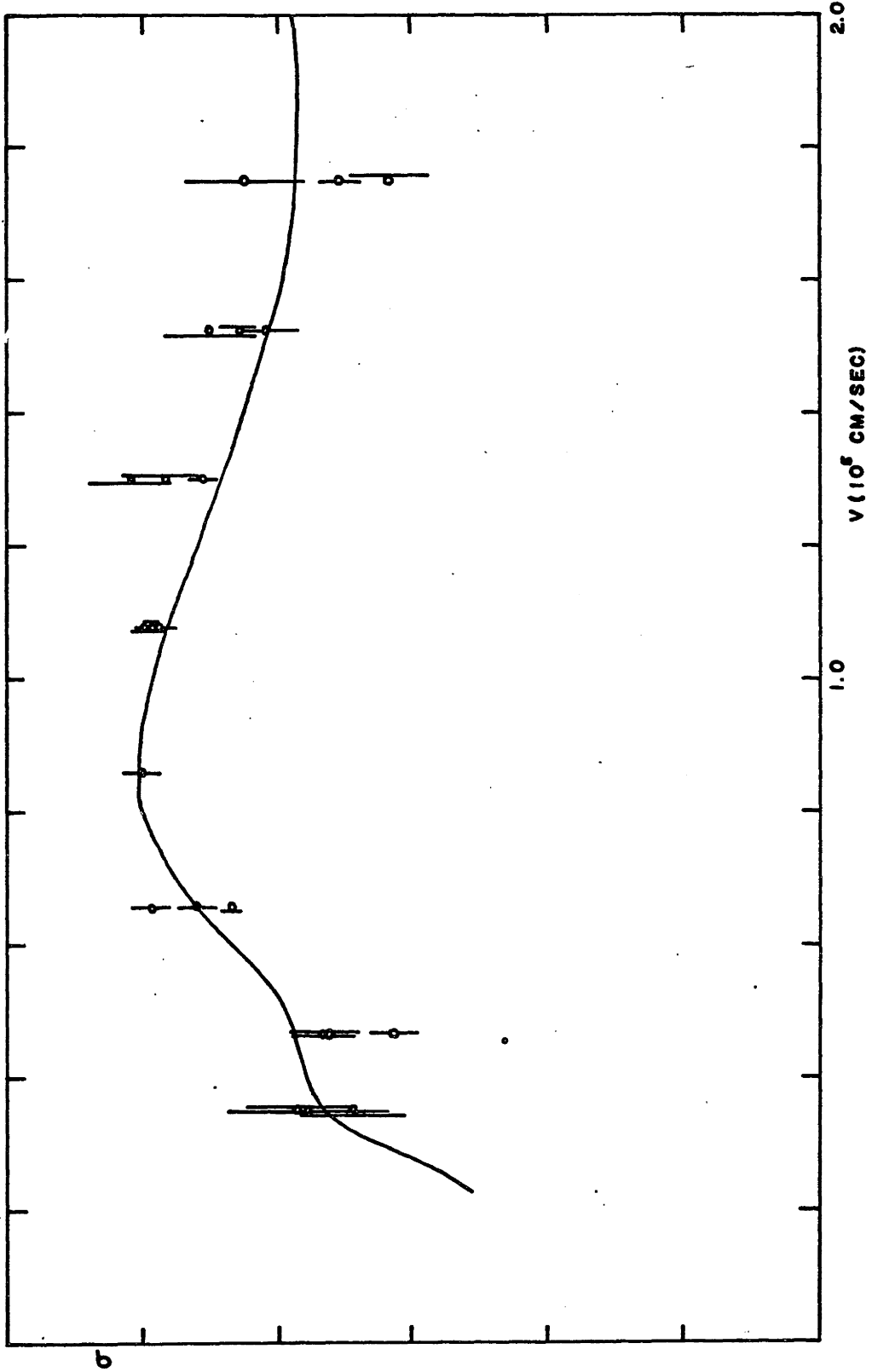


FIG. 30 Nd-Ar CROSS SECTION, LASER SELECTED

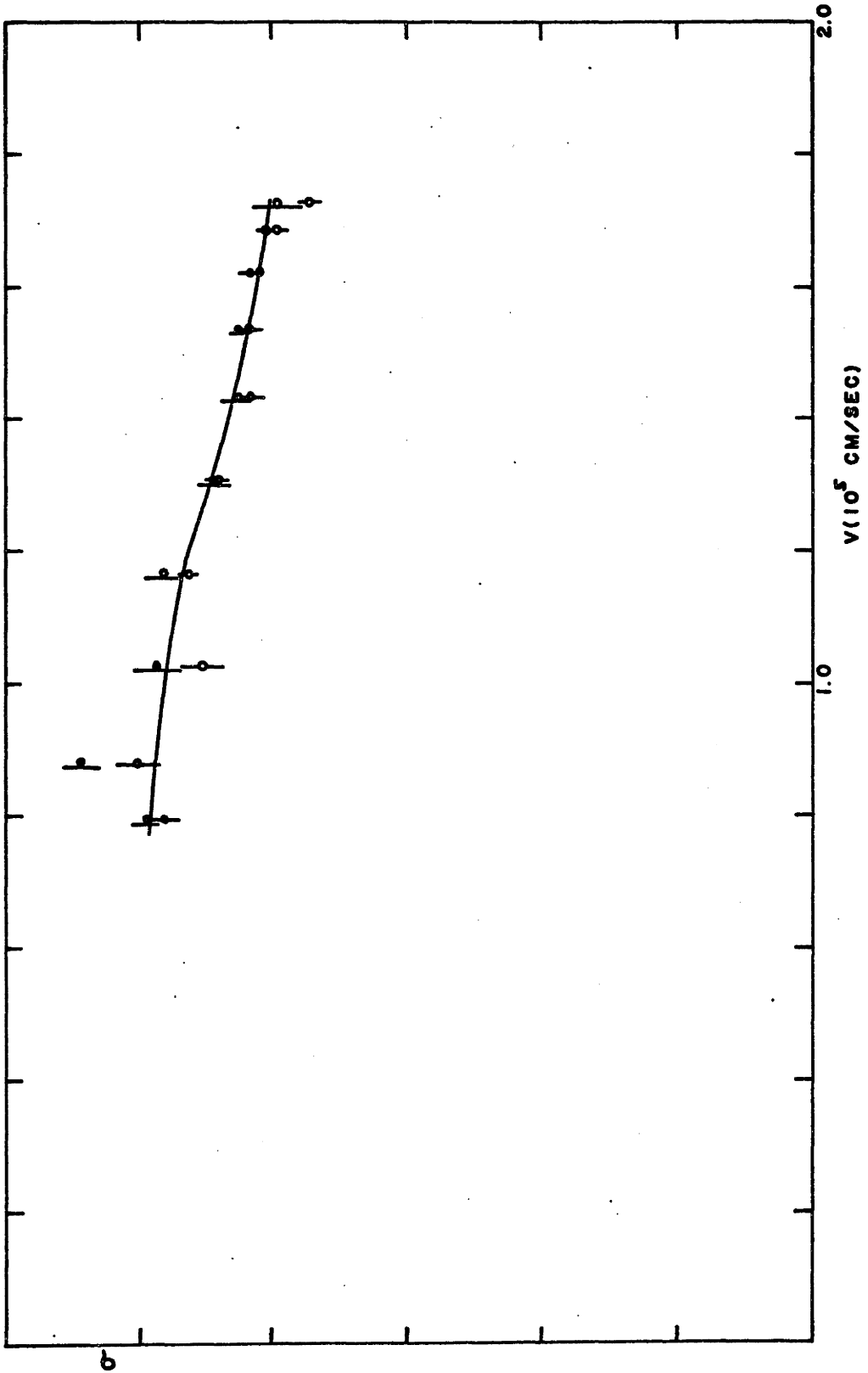


FIG. 31 Na-Ar CROSS SECTION, ROTATION SELECTION

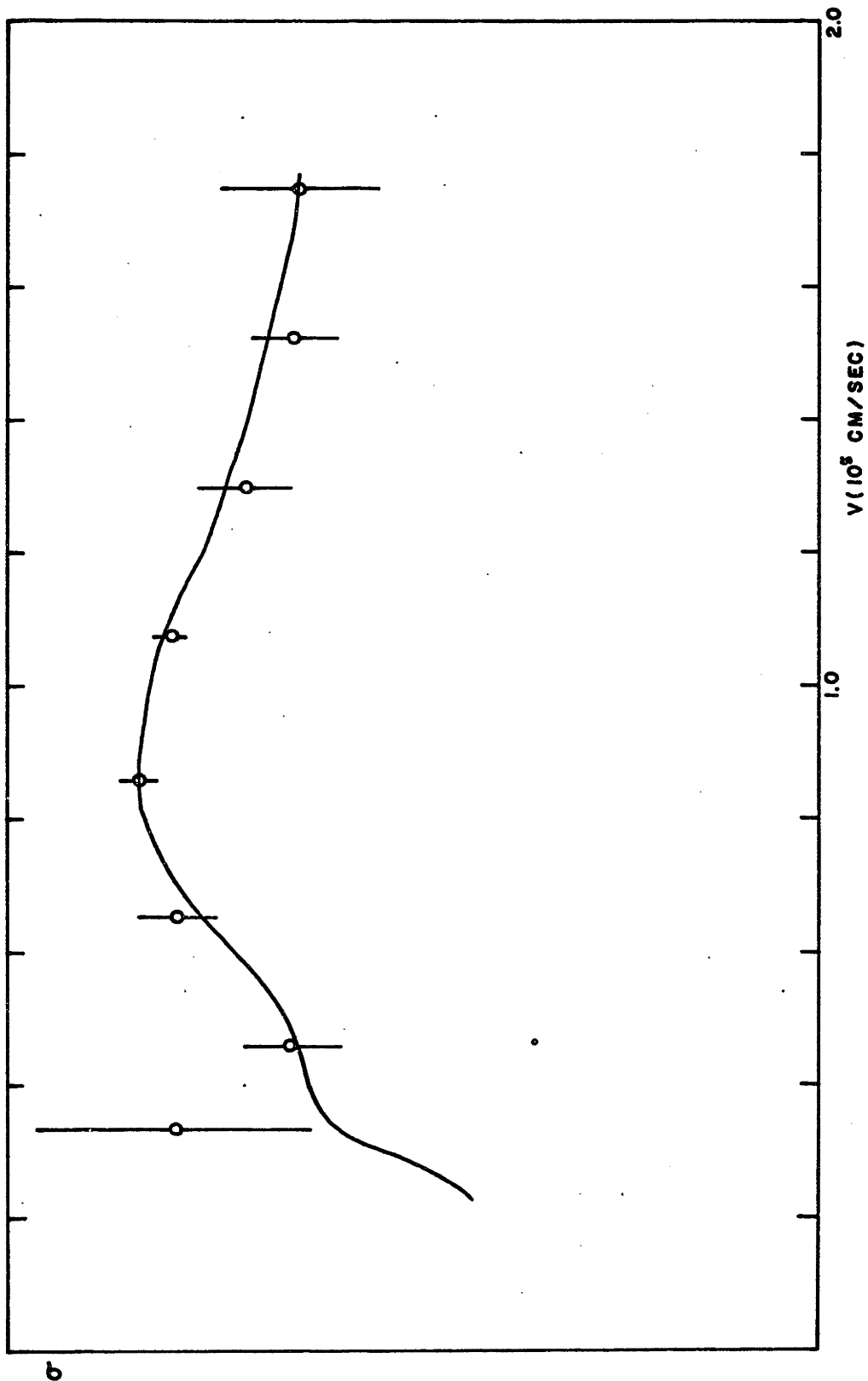


FIG. 32 Na-Ar CROSS SECTION, PARALLEL POLARIZATION

and experiment in Fig. 29,

Fig. 32 shows laser selected data like that of Fig. 30, but with the laser polarization axis in the collision plane. There are slight differences, but they cannot be considered significant at the level of the statistical fluctuations. The general features of the data are the same as for Fig. 30 where the polarization was perpendicular to the collision plane, and are in good agreement with theory.

IV.4 Na-He Collisions

We have used Na-He collisions to do a brief investigation into the magnitude of the effect on the cross section of changing the collision axis with respect to the quantization axis. The laser was aligned perpendicular to the collision plane, and was linearly polarized. The geometry is shown in Fig. 33. With the He beam fixed we measure the cross section when the laser is polarized both along and perpendicular to the He beam. The polarization axis is always at 45° to the observation axis, so the only effect should have to do with the angle between the collision axis and the polarization axis.

The cross section is larger when the polarization is perpendicular to the He beam by 15% (5%). The difference is certainly statistically significant, and represents the sort of effect discussed in Sec. II.5. We have not pursued this line of investigation any further other than to take the steps outlined in Sec. II.5 to avoid the effect. This is to our know-

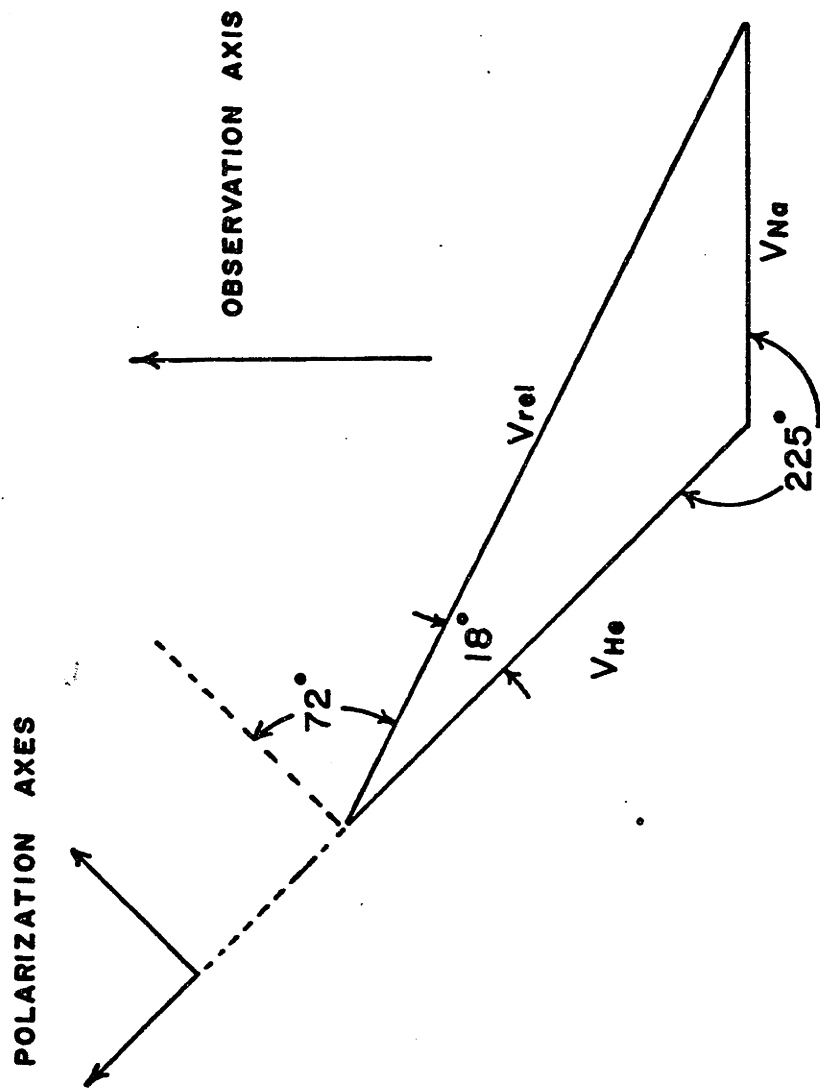


FIG. 33 GEOMETRY FOR POLARIZATION AXIS TESTS

ledge the first observation of such an effect for fine structure transfer collisions. (Apt and Pritchard have observed significant differences when linear as opposed to circular polarization was used, but this represents a change in the excited state distribution of sublevels as well as a reorientation of the quantization axis with respect to the collision axis. See APT76.)

V. DISCUSSION

V.1 Relation to Other Work

We have noted that the Na-Ne data is in substantial disagreement with the theoretical predictions. This result has been confirmed by recent measurements of Apt and Pritchard (APT77). While they do not obtain a cross section curve, they find that our measured cross section can be used to fit their data for the rate of fine structure transfer; the theory of Pascale and Olson (PAS76) does not fit their data. The experimental evidence of fine structure transfer cross section strongly indicates that the Na-Ne theory is in error. The elastic scattering results of Carter and Pritchard (CAR75) show considerable disagreement with the Na-Ne potentials of Pascale and Vandeplanque (PAS74). Specifically, the AII well depth was found to be about 20 times deeper than predicted. The experiment is not as sensitive to the B Σ state potential,

but there is an indication that the BE state is more attractive than predicted by theory and becomes repulsive at a smaller radius. According to the qualitative relations between the potentials and cross sections discussed by Reid (REI73) and Pascale and Olson (PAS76) these features would displace the maximum of the cross section to lower energy and increase the slope at low energy. This is exactly what we observe to be the case with our data as compared to theory.

The Na-Ar data is in substantial agreement with theory. Results of Apt and Pritchard (APT76) also show agreement with theory. Measurements of the potential parameters for the Na-Ar system by York, Scheps and Gallagher (YOR75) indicate disagreement with theory but only by a factor of 2 in the well depth, which indicates, along with the cross section data that Na-Ar theory is in relatively good shape.

V.2 Comparison of Methods

We have used two methods to achieve a range of collision velocities for determining the cross section curves - changing the beam intersection angle by rotation of the gas beam, and selectively exciting a velocity component of the Na beam. Each method has its advantages. The rotation method has produced better statistics partially because the signals are so much stronger. This is because essentially all of the Na atoms in the beam are excited, rather than just a fraction

with a given velocity. Also, the input optics have been more carefully designed for the rotation method, so that the spatial stability of the laser beam is better than for the laser selection method. This is not of course a fundamental limitation of the latter method, but it probably accounts for some of the increased scatter compared to the rotation data. The relative velocity accessible by the two methods is dependent on the particular system involved. For Na-Ne the rotation method achieves higher velocities than the laser selection, but cannot go as low. With Na-Ar the laser selection velocity range extends both higher and lower than the rotation range.

The major difference is in velocity resolution where the laser selection method is far superior. In general the experimental results from the rotation method cannot be directly compared with theory, but must be compared with a folding of the theoretical curve with the experimental resolution. This can be a distinct disadvantage in making detailed comparisons of theory and experiment. The Na oven could be run much hotter, producing a beam with a higher Mach number, but the velocity would be higher and the Na density would be increased, raising the possibility of radiation trapping as well as all the practical difficulties of high Na fluxes. A mechanical velocity selector would be the best solution, providing resolution as good or better than laser selection, especially at low velocities. The laser selected velocity resolution is

limited by the upper state hyperfine structure at least and in some cases by the lower state hyperfine structure. The latter problem could be eliminated by magnetic state selection of the Na beam (for example, with a hexapole magnet), but the problem of upper state hyperfine structure remains as an important limitation. (Use of optical pumping to overcome this as suggested by Hertel et al (HER75) will not produce satisfactory results because the laser intensity needed will produce too much power broadening.) For the present state of the data, however, the laser selection resolution is sufficient that direct comparison of the experimental and theoretical cross sections are possible.

We can also compare our method to that employed by Apt and Pritchard to measure the same processes. The method has been described by this author and Pritchard (PHI74). It involves selectively exciting those Na atoms in a gas cell which have a particular velocity along the laser beam. The Na atom, with one velocity component selected, collides with rare gas atoms also present in the cell. Good velocity resolution depends on high Na velocities and heavy rare gas atoms, so that the unselected velocities are relatively unimportant. Under the best conditions Apt and Pritchard obtain velocity resolution somewhat better than that of our rotation method, but only at the highest velocities. Our laser selected velocity resolution exceeds theirs at all velocities and we are

not limited to heavy rare gases. Our range of velocities extends both higher and lower than theirs. The range and resolution of their measurements has been insufficient to identify the velocity at which the cross section peaks for any system.

An advantage of the Apt-Pritchard measurements is that larger gas densities are obtainable so signals are larger; the experiment is also simpler from a practical point of view. The gas density can be measured directly, so absolute cross section measurements can be made, which yields an additional piece of information.

V.3 Suggestions for Future Work

As we have mentioned there are a number of possible improvements to the techniques we have developed, such as better spatial stability of the laser beam, mechanical velocity selection, magnetic state selection, and better alkali jetting. Also of value would be automated laser frequency control, allowing more rapid data acquisition which would improve stability. Accessing frequencies between the discrete steps we have used would be useful. The improved statistics resolution, and velocity range resulting from these changes should allow a more detailed comparison with the theoretical predictions.

Studies of the relation of the cross section and its velocity dependence to the sublevel excited are of interest. The most information would be obtained by decoupling \vec{J} and \vec{I} with

a magnetic field and selectively exciting particular m_j states, observing the transfer fluorescence with appropriate polarizers. This would eliminate the ambiguity caused by the mixing of m_j levels by the hyperfine interaction. Further studies of the changes in cross section as a function of the angle between the collision axis and quantization axis are in order. The theoretical problem must be given attention as well, since in the absence of beams experiments it has been neglected.

Extension of the present studies to other rare gases is an obvious imperative, given the existence of theoretical predictions. Studies of other alkalis are also of interest since they can be calculated by the same methods as applied to Na. These are experimentally more difficult because of smaller cross sections and difficulty of obtaining lasers at the proper wavelength for excitation. Nevertheless, the measurements are important because of the different structure intervals which enable more detailed study of a particular range of Massey parameters.

An especially exciting possibility for further study is determination of the differential scattering cross section for fine structure transitions. The information obtained from such measurements can be related to the potential much more directly than information about the total cross section. It should be possible to infer the difference between the Σ and Π

potentials from differential scattering data.

The central difficulty in differential scattering of this nature is that the atoms will decay to the ground state before they can be detected by conventional means such as surface ionization. We propose to circumvent the problem by using a second laser to excite the scattered atoms to a higher level, observing light from transitions connected directly or indirectly to this higher level. The second excitation is both state selective and velocity selective, so we can choose to observe only atoms in a particular state with a particular velocity component. Sufficient numbers of measurements with different frequencies and orientations of the second laser beam will yield the complete distribution of scattered atomic velocities, which is the differential cross section.

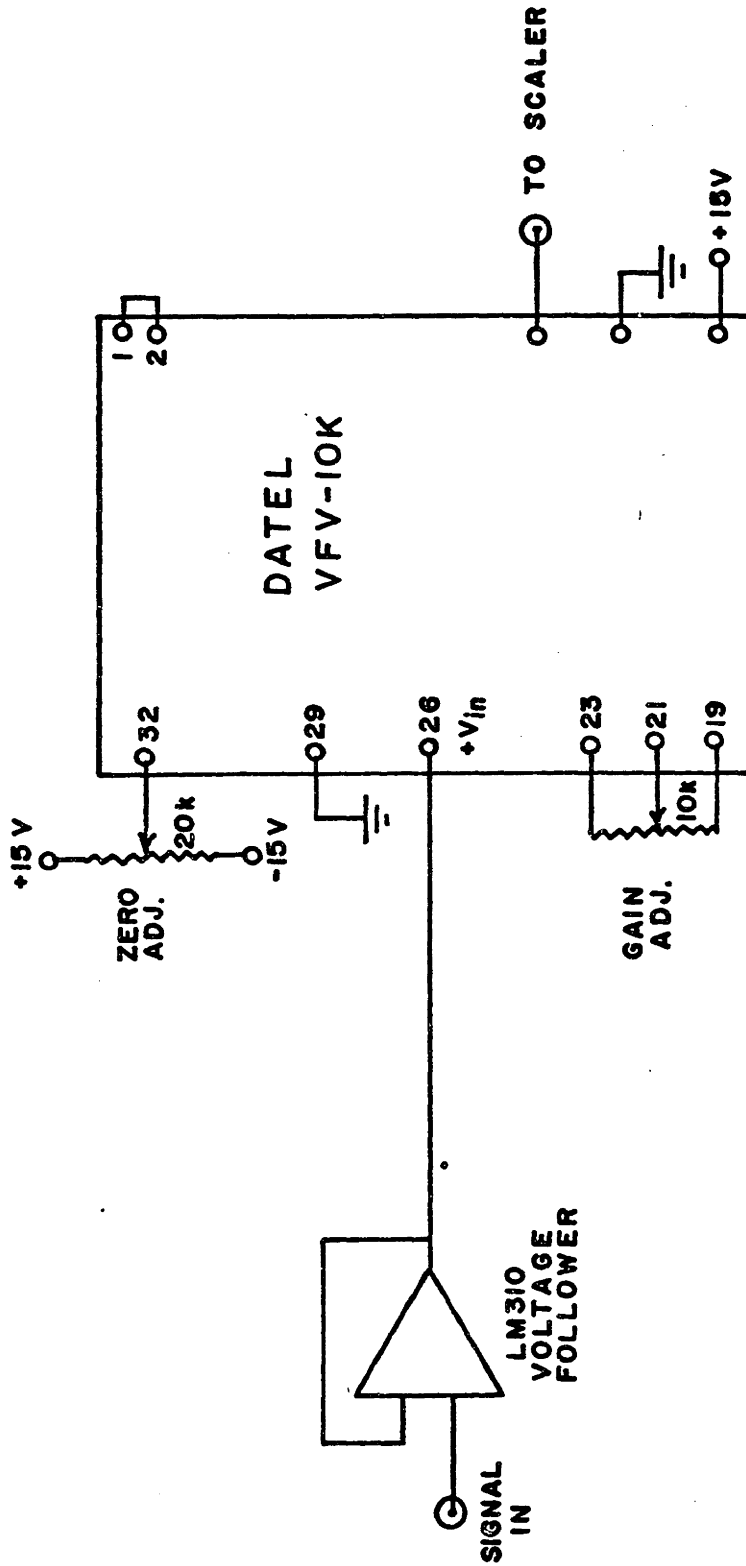


FIG. A1 V/F CIRCUITRY

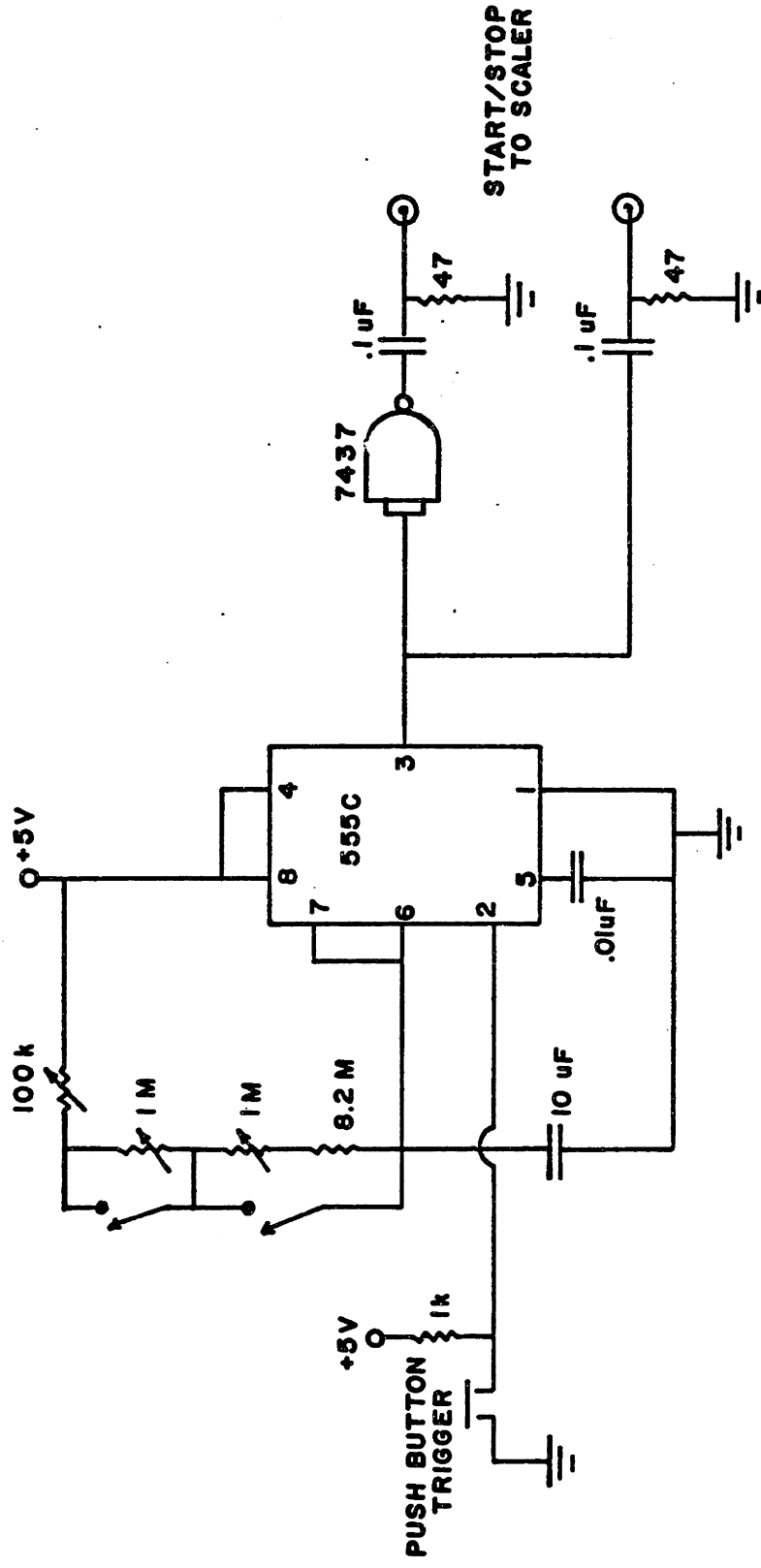


FIG. A2 SCALER GATE

REFERENCES

Part Two

- AND65 J.B. Anderson and J.B. Fenn, *Phys. Fluids* 8, 780 (1965).
- AND76 R.W. Anderson, T.P. Goddard, C. Porravand and J. Warner, *J. Chem. Phys.* 64, 4037 (1976).
- APT76a J. Apt and D.E. Pritchard, *Phys. Rev. Lett.* 37, 91 (1976).
- APT76b J. Apt, Ph.D. Thesis, Massachusetts Institute of Technology, 1976 (unpublished).
- APT77 J. Apt and D.E. Pritchard, to be published.
- BAY69 W.E. Baylis, *J. Chem Phys.* 51, 2665 (1969).
- CAR75 G.M. Carter, D.E. Pritchard, M. Kaplan and T.W. Ducas, *Phys. Rev. Lett.* 35, 1144 (1975).
- DAS70a E.I. Dashevskaya, E.E. Nikitin and A.I. Reanikov, *J. Chem. Phys.* 53, 1175 (1970).
- DAS70b E.I. Dashevskaya, E.E. Nikitin and A.I. Reanikov, *Opt. Spectrosc.* 29, 540 (1970).
- ELB71 M. Elbel and W. Schneider, *A. Physik* 241, 244 (1971).
- GAL68 A. Gallagher, *Phys. Rev.* 172, 88 (1968).
- HAN57 H.G. Hanson, *J. Chem. Phys.* 27, 491 (1957).
- HER75 I.V. Hertel, H. Hofmann, K.A. Rost and S. Azarkadeh, *J. Phys. E.* 8, 1023 (1975).
- HER50 G. Herzberg, *Spectra of Diatomic Molecules*, 2nd edition, Van Nostrand Reinhold, New York, 1950.
- JOR66 J.A. Jordan and P.A. Franken, *Phys. Rev.* 142, 20 (1966).
- KRA66 L. Krause, *Appl. Opt.* 5, 1375 (1966).
- LAN32 L. Landau, *Phys. Z. Sowjetunion*, 1, 46 (1932).
- LIJ72 P.L. Lijnse, Report #i398, Fysisch Laboratorium, Rijks Universiteit Utrecht, Netherlands (1972).
- LOC28 W. Lochte-Holtgreven, *Z. Physik* 47, 632 (1928).
- MAS70 F. Masnou-Seeuws, *J. Phys. B* 3, 1437 (1970).

REFERENCES

Part Two

- NIK65 E.E. Nikitin, *Opt. Spectrosc.* 19, 91 (1965).
- OLS75 R.E. Olson, *Chem Phys. Lett.* 32, 250 (1975).
- PAR72 J.M. Parson, P.E. Siska and Y.T. Lee, *J. Chem Phys.* 56, 1511 (1972).
- PAS74 J. Pascale and J. Vandeplanque, *J. Chem. Phys.* 60, 2278 (1974).
- PAS76 J. Pascale and R.E. Olson, *J. Chem. Phys.* 64, 3538 (1976).
- PHI74 W.D. Phillips and D. Pritchard, *Phys. Rev. Lett.* 33, 1254 (1974).
- PIT67 J. Pitre and L. Krause, *Can. J. Phys.* 45, 2671 (1967).
- REI69 R.H.G. Reid and A. Dalgarno, *Phys. Rev. Lett.* 22, 1029 (1969).
- REI73 R.H.G. Reid, *J. Phys. B* 6, 2018 (1973).
- SCH71 W. Schneider, *Z. Physik* 248, 387 (1971).
- SEI56 R. Seiwert, *Ann. Phys.* 18, 54 (1956).
- SIS71 P.E. Siska, J.M. Parson, T.P. Schafer and Y.T. Lee, *J. Chem. Phys.* 55, 5762 (1971).
- WOO14 R.W. Wood, *Phil. Mag.* 27, 1018 (1914).
- YOR75 G. York, R. Scheps and A. Gallagher, *J. Chem. Phys.* 63, 1052 (1975).
- ZEN32 C. Zener, *Proc. Roy. Soc. (London)* A137, 696 (1932).

ACKNOWLEDGEMENT

I would like to thank Prof. Daniel Kleppner for the support and guidance which he has provided during my career as a graduate student. I will always be grateful for the congenial atmosphere for work and fellowship of the research group under his direction. The interest and encouragement of Prof. David Pritchard since I joined the group has been greatly appreciated, and I am grateful for the experience of working with him.

Special thanks go to Bill Cooke who collaborated on the maser experiment, suffering with me through many long nights of data taking. The important contributions of Francine Wright, who developed the data analysis procedure and Dave McKenzie who designed and built much of the apparatus for both experiments are greatly appreciated. I am especially thankful for the help of Charles Glaser who has collaborated on the design and execution of the collisions experiment.

I am grateful to Frank Payne of the Material Science Center for his patient instructions in the art of machining and to all the people in the RLE machine, electronics, glass, tube and brazing shops who have been so ready to give advice and assistance. I am thankful to all those past and present members of the research group whose shared friendship and knowledge has helped me along the way. I would like to specially thank Fred Walther under whom I served my appren-

ticeship as a graduate student and who introduced me to the mysteries of the maser.

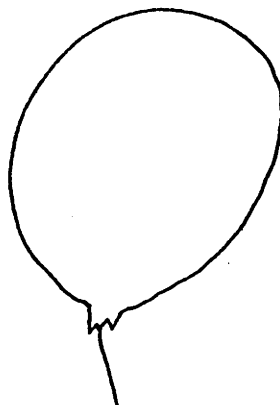
I am thankful to the NSF for its fellowship support during my first three years of graduate school and for its support of the research described in this thesis. I am thankful to RLE for providing the support and facilities which made this research possible.

I am deeply thankful to Rose Bella and especially Jo Ann Kruger who performed the arduous task of typing the manuscript with consummate efficiency.

Finally and most importantly I thank my wife Jane who has shared the pain and joy of those years of building, data taking, analyzing and writing which are now coming to an end. Her love and encouragement have made the pains milder and the joys sweeter.

BIOGRAPHICAL NOTE

William D. Phillips was born in Wilkes-Barre, Pa. on November 5, 1948. He attended public schools in Pennsylvania and was graduated from Camp Hill High School in June 1966. He received a B.S. in Physics from Juniata College in May, 1970.



Reflections on Finishing a Thesis

Here is Edward Bear, coming downstairs now, bump, bump, bump, on the back of his head, behind Christopher Robin. It is, as far as he knows, the only way of coming downstairs, but sometimes he feels that there really is another way, if only he could stop bumping for a moment and think of it. And then he feels that perhaps there isn't. Anyhow, here he is at the bottom, and ready to be introduced to you. Winnie-the-Pooh.

from Winnie-the-Pooh

by A. A. Milne

